Strong-field physics in tailored light

Sambit Mitra

SIGILL. UNIVERSITAT. LUDOVIC. MAXIM.

München 2023

Strong-field physics in tailored light

Sambit Mitra

Dissertation
der Fakultät für Physik
der Ludwig-Maximilians-Universität
München

vorgelegt von
Sambit Mitra
aus Kalkutta

München, den 28.04.2023

Erstgutachter: Prof. Dr. Matthias F. Kling
Zweitgutachter: Prof. Dr. Mikhail Ivanov
Tag der mündlichen Prüfung: 22.06.2023

Contents

List of Figures

List of Tables

Zusammenfassung

Diese Arbeit befasst sich mit drei verschiedenen Arten, wie intensive maßgeschneiderte Lichtfelder mit Materie in ihrer Gas- und zweidimensionalen Festkörperphase interagieren. Maßgeschneiderte Lichtfelder im Nah- und Mittelinfrarotbereich (NIR, MIR) ermöglichen eine präzise Kontrolle über die elektronische Bewegung auf atomarer Ebene auf Atto- und Femtosekundenzeitskalen.

Die erste Anwendung befasst sich mit der hohen Harmonischen Erzeugung (HHG), einer Quelle kohärenter und ultrakurzer Lichtpulse im extremen Ultraviolet (XUV). Die erhaltenen XUV-Spektren erfordern oft Modifikationen für verschiedene Anwendungen, die in der Regel durch hochabsorbierende Filter oder durch maßgeschneiderte dielektrische Spiegel erreicht werden, die den Fluss des XUV-Lichts drastisch reduzieren. Diese Arbeit berichtet über ein neuartiges Verfahren zur Unterdrückung einzelner Harmonischer eines solchen XUV-Kamms, das gleichzeitig spezifische gerade und ungerade Ordnungen in den HHG Spektren beeinflusst, die durch intensitv maßgeschneiderte zweifarbige sowie mehrzyklische Laserpulse in Neon erzeugt werden. Realistische makroskopische Rechnungen gemäß der Starkfeldnäherung bestätigen die experimentelle Beobachtung und korrelieren den Effekt mit dem Einsatz von symmetriebrechenden Laserfeldern ($\omega - 2\omega$). Semiklassische Berechnungen bestätigen den Effekt weiter und enthüllen seinen zugrunde liegenden Mechanismus. Hierbei wird eine nichttriviale spektrale Interferenz zwischen nachfolgenden asymmetrischen Halbzyklen gefunden, die für die Unterdrückung verantwortlich ist. Dieses Verfahren kommt insbesondere zukünftigen zeitlich aufgelösten spektroskopischen Untersuchungen von Molekülen zugute. Diese sind auf schmallbandige XUV-Lichtanregung bei verschieden Photonenenergien, sowie einen hohen Fluss angewiesen.

Das zweite Szenario beschäftigt sich mit isolierten Soft-X-Ray Attosekundenpulsen, die durch HHG in Neon erzeugt werden und von polarisationskontrollierten Wenigzyklen-MIR-Pulsen angetrieben werden, was üblicherweise als Polarisationsgating bezeichnet wird. Eine genaue Abschätzung der Soft-X-Ray Attosekundenpulse in einem solchen Experiment bleibt aufgrund ihrer höheren Photonenenergien und breiten spektralen Bandbreite herausfordernd. In dieser Arbeit wird eine numerische Studie, basierend auf der Starkfeldnäherung präsentiert, um die mit realistischen polarisationskontrollierten MIR-Laserpulsparametern einschließlich makroskopischer Ausbreitungseffekte erreichbare Pulsdauer der Soft-X-Rays abzuschätzen. Die intrinsische Dispersion (Attochirp) eines solchen Pulses in den Berechnungen wird durch das Durchlaufen einer 90 cm Plasmakolonne kompensiert, wonach eine Pulsdauer von 110 as erreicht wird, während die Fouriergrenze bei 31 as liegt.

Diese theoretische Schätzung dient als Referenz zur Beurteilung der Genauigkeit neuer Retrieval-Techniken und betont auch die Notwendigkeit neuer Kompressionsschemata, die höhere Ordnungen des Chirps im Soft-X-Ray Bereich ausgleichen.

Das dritte und letzte Szenario dieser Arbeit beschäftigt sich mit der Verwendung von starken dreiblättrigen Kleeblattförmigen Lichtfeldern weit von der Resonanzfrequenz, um die Zeitumkehrsymmetrie zu verändern und eine selektive Bandlückenmodifikation im K- und K'-Punkt im Impulsraum hervorzurufen. Das gewählte Material ist ein inversionssymmetriebrechender zweidimensionaler Isolator (Monolayer hBN). Ein solches Schema wurde nur theoretisch vorhergesagt aber experimentell noch nicht gezeigt. Hier wird eine neuartige Vorrichtung entwickelt, um dreiblättrige Kleeblattförmige Lichtfelder zu erzeugen, indem man zwei Farben ($\omega - 2\omega$) gegenläufiger Pulse kombiniert. Eine kontrollierte Verzögerung zwischen den Farben induziert eine Drehung bezüglich des hBN-Gitters, welche die Bandlücke dynamisch verändert und damit die Elektronenpopulation in jedem Tal beeinflusst. Dies verursacht eine Valley-Polarisation. Durch einen dritten Puls wird die dadurch verursachte Änderung in der Helizität der Zwischenband Harmonischen dritter Ordnung untersucht. Die hier präsentierten Ergebnisse eröffnen weitere Möglichkeiten in Richtung ultraschnell Modifikation von Bandlücken bei Petahertzfrequenzen, die zukünftig die Elektronik revolutionieren können.

Abstract

This thesis reports on three distinct scenarios of strong tailored light fields interacting with matter in its gaseous and two-dimensional solid phases. Tailored light fields in the near- and mid-infrared (NIR, MIR) region facilitate precise control over electronic motion on an atomic level at atto- to femtosecond timescales.

The first scenario deals with high-harmonic generation (HHG), a source of coherent and ultra-short XUV light pulses. The obtained XUV spectra often require modification for various applications which are primarily carried out using highly absorptive filters or custom-designed dielectric mirrors which drastically reduce the flux of the XUV light. This thesis reports on a novel scheme enabling the suppression of individual harmonics of such an extreme ultraviolet (XUV) comb, simultaneously affecting specific even and odd orders in the high-harmonic spectra generated by strongly tailored, two-colour ($\omega - 2\omega$), multi-cycle laser pulses in neon. Realistic macroscopic strong-field approximation calculations confirm the experimental observations and correlate the effect to the use of symmetry-broken laser fields. Semi-classical calculations further corroborate the effect and reveal their underlying mechanism, where a nontrivial spectral interference between subsequent asymmetric half-cycles is found to be responsible for the suppression. This scheme particularly benefits future molecular time-resolved spectroscopy studies relying on narrow-band XUV light excitation around different photon energies with high flux.

The second scenario deals with isolated soft-X-ray attosecond pulses generated via HHG in neon and driven by polarization-tailored few-cycle MIR pulses, commonly referred to as polarization gating. Accurate estimation of the attosecond soft-X-ray pulses in such experiments remains challenging given their higher photon energies and broad spectral bandwidth. Numerical results, based on strong-field approximation, are presented in this thesis to estimate the soft-X-ray pulse durations achievable using realistic polarization-gated MIR laser pulse parameters including macroscopic propagation effects. The intrinsic dispersion (attochirp) of such a pulse in the calculations is compensated by traversing it through a 90 cm plasma column after which a pulse duration of 110 as is obtained while the Fourier limit lay at 31 as. This theoretical estimate serves as a reference in judging the accuracy of new retrieval techniques while also highlighting the need for new compression schemes which compensate for higher-order dispersion in the soft-X-ray region.

The third and final scenario presented in this thesis deals with using strong and far-off-resonant trefoil-shaped tailored light fields to alter time-reversal symmetry and induce valley selective bandgap modification (K and K' points in momentum space). The material chosen is monolayer hBN, an inversion-symmetry broken two-dimensional insulator. Such a scheme has only been predicted theoretically but not yet experimentally realized. Here, a novel apparatus is developed to produce trefoil light fields by combining two-colour ($\omega-2\omega$) counter-rotating pulses. Further, a controlled delay between the colours induces a rotation w.r.t. the hBN lattice, dynamically altering the band-gap and thereby electron population at each valley. A third linearly polarized pulse is then used to probe the induced valley polarization through a correlated change in the detected helicity of its intraband harmonics (third harmonic). The results presented here open further avenues in the direction of ultra-fast band engineering at petahertz frequencies which could revolutionize the future of electronics.

Chapter 1

Introduction

Most observable phenomena in the macrocosmic universe are directly or indirectly linked to microcosmic manifestations on the atomic scale. The electrons surrounding the nuclei are the protagonists, governing how atoms interact to form matter and give rise to a plethora of unique material properties. Decades of theoretical and experimental studies on electrons and their quantum nature in matter have led to a deep understanding of how atoms, molecules, and complex systems behave.

On the other hand, the propagation and detection of light are inherently linked to how it interacts with the medium through which it travels, making it a highly reliable probe of electronic processes in matter. The rapid development of lasers since 1960 [104], which produce light with a high degree of coherence, with the possibility of reaching high intensities [148], along with the ability to be switched (on and off) at ultrashort time scales [59], has further enhanced our ability to precisely probe and control electronic properties of matter [169].

In this dissertation, the primary focus is on controlling fundamental electronic processes in matter by tailored light. This tailoring is best understood within the electromagnetic formalism of light, where it is described as a sinusoidal oscillation of the electric field[1] [53]. As is usually the case with high-intensity coherent light sources, they radiate as a train of ultrashort wave packets with an underlying sinusoidal electric field oscillating at a specific central frequency. At a fixed point in space, light is tailored by modifying the shape of the sinusoidal electric field in one or both polarization directions, leading to exotic electric field structures. As described in the later chapters, this is realized in the lab by interferometrically combining a secondary sinusoidal light field with slightly different parameters, such as intensity, central wavelength, polarization helicity, and time delay. When such tailored light interacts with electrons in matter, they give rise to a new electronic motion controlled by tailored light and influenced by the morphology of the material. Three such scenarios were studied within the framework of this doctoral thesis and can be categorized as follows:

1. Controlling extreme ultraviolet (XUV) combs using symmetry-broken two-color light

---

[1] Given the light intensities used in this thesis, the magnetic component can be safely ignored.

fields in gaseous neon (zero-dimensional material)

2. Controlling pulse duration of soft-Xray emission using polarization-gated light fields in gaseous neon (zero-dimensional material)
3. Controlling valley polarization using off-resonant polarization-shaped bi-circular two-color light fields in monolayer hBN (two-dimensional material)

First scenario

XUV combs, produced by infrared multi-cycle pulsed laser sources through high harmonic generation, exhibit sharp peaks in the spectral domain separated by twice the photon energy of the driving laser [96]. The XUV combs are additionally restricted in time to a few tens of femtoseconds, making them stand out in comparison with synchrotron radiation. Furthermore, in the XUV spectral region, many atoms and molecules possess large valence- and inner-shell photo-absorption cross-sections, making the combs a useful tool for pump-probe spectroscopy experiments. In particular, investigations involving ultrafast molecular dissociation dynamics are well suited [158, 70, 1]. The kinetic energy of the photoemitted electrons reveals the intermediatory states involved in wavepacket motion, and the presence of multiple peaks in the XUV comb generated by the high-harmonic process can obscure the photoelectron spectrum with the signal from harmonic peaks. Often, thin metallic spectral filters [64, 43] or multi-layer mirrors [58] are used to isolate a single or a few peaks from the complete XUV harmonic comb. However, this process is lossy, given the strong absorption of XUV in solid-state spectral filters. Multi-layer mirrors restrict flexibility as they work well only for a very specific range of photon energies and must be replaced when a different spectral region is to be filtered, if at all allowed by the combination of materials used to fabricate it. The results obtained in Chapter 3 address this particular issue by demonstrating the ability to manipulate the spectral density of the XUV comb down to any single harmonic intrinsically, through modifications in the high-harmonic generation process, which predominantly redistributes the spectral density without sacrificing photon flux (ignoring propagation effects).

Second scenario

Looking beyond XUV, the rapid development of laser technology, especially in the direction of high-power long-wavelength drivers spanning from 1.5 µm to 3 µm, has led to the availability of high-harmonic generation-based soft-X-ray sources on a tabletop [26, 32, 94]. Such highly energetic light with high spatial and temporal coherence is also an extremely useful tool for the spectroscopy of electronic properties of materials, otherwise not possible with lower-energy radiation [92]. Namely, involving a K-shell excitation in matter containing carbon and oxygen extending from 282 eV to 533 eV, respectively [127, 4, 128], commonly referred to as the water window, owing to its transparency in water and making it an ideal tool for studying organic molecules in live specimens. Given the lack of convincing experimental retrievals on the pulse duration of such soft-X-ray pulses, Chapter 4 theoretically sheds light on the possible pulse duration using a polarization-gated driving laser configuration, including propagation effects.

Third scenario

Since the first isolation of graphene in 2004 [122], research on atomically thin two-dimensional materials has grown exponentially owing to their unique electronic properties. More specifically, in two-dimensional materials with broken spatial-inversion symmetry, there exist two valleys or minima in the conduction and valence bands in momentum space at the K and K' points of the Brillouin zone. These points, although degenerate in energy, possess a unique degree of electronic freedom referred to as the valley pseudospin. The ability to address the valleys individually, for example by the use of resonant circularly polarized light, has given birth to a new research field referred to as valleytronics. Such a system leads to fundamentally new material physics, many of which have already been explored in the literature. These range from nonlinear optical properties [141, 5], Hall effect [103, 34], valley-contrasting physics [108, 137, 88, 109], spin-orbit coupling [160], chirality of quasiparticles [173], piezoelectric effects [161], and superconductivity [100, 17]. In terms of applications, they are promising candidates for replacing MOSFETs (Metal-oxide-semiconductor field-effect-transistor) as a more power-efficient switching device in classical digital electronics [155], or realizing easily scalable valley qubits for quantum computing [155, 143], or even in integrated photonics as circularly polarized light emitters and polarization-sensitive detectors [155, 159]. Most of the above-mentioned studies involving light interaction occur close to the resonant regime except what Langer and co-workers report, where they demonstrate control over valley polarization using off-resonant terahertz laser pulses after a resonant excitation [88]. Chapter 5 aims to extend the studies in the off-resonant regime further by demonstrating exclusive far-off-resonant control over valley polarization using tailored light fields and their subsequent all-optical readout with mid-infrared driving lasers in a wide-bandgap two-dimensional material (hexagonal boron nitride).

Thesis overview

This thesis is organized in a way where Chapter 2, following this introduction, provides a formal description of ultrashort laser pulses and the principles used to characterize them. The chapter further highlights specific theoretical aspects of light-matter interaction in gases and solids, respectively, which are useful for understanding the methods and results discussed in the following chapters. Subsequently, Chapter 3 reports on experiments and numerical simulations carried out in the direction of the first scenario, where the individual (even or odd order) peaks of the high-harmonic XUV comb produced by multi-cycle femtosecond laser pulses could be controlled using two-color laser electric field shaping [114]. The second scenario investigated in this thesis in Chapter 4 is a numerical study involving high-harmonic generation by polarization-gated mid-infrared laser pulses, considering a realistic gas medium, and reporting on the shortest possible soft-X-ray pulses that can be obtained. The final and third scenario discussed in Chapter 5 reports on experiments performed on large-bandgap two-dimensional materials[2]. The valley degree of freedom in this material is selectively accessed using strong polarization-tailored mid-infrared laser pulses based on light-induced band structure modification at sub-cycle timescales [137, 76].

---

[2] Specifically refers to hexagonal two-dimensional systems with broken spatial-inversion symmetry

Publications co-authored relevant to this dissertation:

1. **Lightwave-controlled band engineering in quantum materials**
   S Mitra, Á Jiménez-Galán, M Neuhaus, REF Silva, V Pervak, MF Kling, S Biswas
   arXiv:2303.13044, submitted to: *Nature* (2023)

2. **Suppression of individual peaks in two-colour high harmonic generation**
   S Mitra, S Biswas, J Schötz, E Pisanty, B Förg, GA Kavuri, C Burger, W Okell, M Högner, I Pupeza, V Pervak, M Lewenstein, P Wnuk, MF Kling
   Journal of Physics B: Atomic, Molecular and Optical Physics 53 (13), 134004 (2020)

Other publications co-authored during this dissertation:

3. **Anomalous formation of trihydrogen cations from water on nanoparticles**
   MS Alghabra, R Ali, V Kim, M Iqbal, P Rosenberger, S Mitra, R Dagar, P Rupp, B Bergues, D Mathur, MF Kling, AS Alnaser
   Nature Communications 12 (1), 1-8 (2021)

4. **Near-field induced reaction yields from nanoparticle clusters**
   P Rosenberger, P Rupp, R Ali, MS Alghabra, S Sun, S Mitra, SA Khan, R Dagar, V Kim, M Iqbal, J Schotz, Q Liu, SK Sundaram, J Kredel, M Gallei, C Costa-Vera, B Bergues, AS Alnaser, MF Kling
   ACS Photonics 7 (7), 1885-1892 (2020)

5. **High-contrast, intense single-cycle pulses from an all thin-solid-plate setup**
   M Seo, K Tsendsuren, S Mitra, M Kling, D Kim
   Optics Letters 45 (2), 367-370 (2020)

6. **Few-cycle laser driven reaction nanoscopy on aerosolized silica nanoparticles**
   P Rupp, C Burger, NG Kling, M Kübel, S Mitra, P Rosenberger, T Weatherby, N Saito, J Itatani, AS Alnaser, MB Raschke, E Rühl, A Schlander, M Gallei, L Seiffert, T Fennel, B Bergues, MF Kling
   Nature Communications 10 (1), 1-7 (2019)

7. **Nonadiabatic ponderomotive effects in photoemission from nanotips in intense midinfrared laser fields**
   J Schötz, S Mitra, H Fuest, M Neuhaus, WA Okell, M Förster, T Paschen, MF Ciappina, H Yanagisawa, P Wnuk, P Hommelhoff, MF Kling
   Physical Review A 97 (1), 013413 (2018)

8. **Attosecond-controlled photoemission from metal nanowire tips in the few-electron regime**
   B Ahn, J Schötz, M Kang, WA Okell, S Mitra, B Förg, S Zherebtsov, F Süßmann,

C Burger, M Kübel, C Liu, A Wirth, ED Fabrizio, H Yanagisawa, D Kim, B Kim, MF Kling
APL Photonics 2 (3), 036104 (2017)

Chapter 2

Theoretical Background

2.1 Ultrashort laser pulses

Since the invention of the laser by Theodore H. Maiman in 1960, there has always been a push to access very high optical laser intensities and temporally short laser pulses [104]. The subsequent milestone in this direction can probably be attributed to the discovery of mode-locked Titanium-Sapphire as a broadband lasing medium by Peter Moulton in 1982, as the achievable pulse duration of a laser pulse is intrinsically related to its spectral bandwidth [117]. This can be intuitively understood by considering a broad range of sinusoidal waves with different wavelengths phase-coherently adding up, to produce a sharp spike. Additionally, this gain medium has led to the development of some of the world's highest pulse-energy laser sources through the recent Nobel-Prize winning technique of chirped pulse amplification (CPA) and withstanding very high pulse energies [148, 168]. Although the gain medium has changed over the years, including within the experiments conducted in this thesis where a Yttrium Aluminium Garnet (YAG) crystal is used, most of the fundamental principles still remain the same.

2.1.1 Mathematical description

Intense ultrashort laser pulses have revolutionized the way in which people study light-matter interaction as already recognized by a Nobel prize for his contribution to the field of femtochemistry to Ahmed H. Zewail in 1999. At the intensities relevant to the experiments in this thesis, only the electric field $E(t)$ of the laser pulse plays a role and can be described as

$$E(t) = 0.5\sqrt{I_{env}(t)}e^{i\omega_0 t}e^{-i\phi(t)} + c.c. \tag{2.1}$$

where $\sqrt{I_{env}(t)}$ is the envelope which is usually approximated to a Gaussian (for a flat spectral phase) but can take other shapes depending on the spectral distribution, ω_0 is the central wavelength which can be computed using the weighted mean of the spectral distribution of the laser output and $\phi(t)$ is the temporal phase which includes a time-independent factor ϕ_{CEP}, better known as the carrier-envelope-phase (CEP) indicating

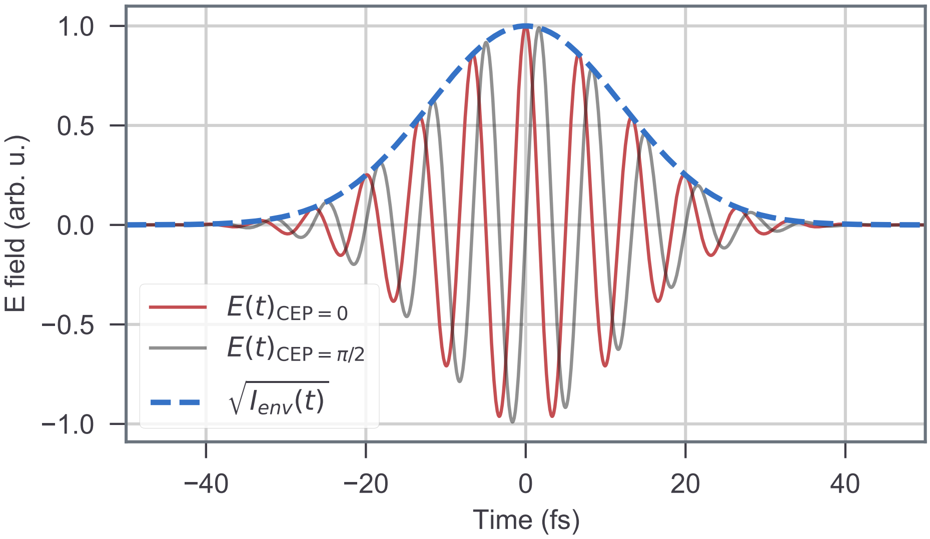

Figure 2.1: An illustrative example of a Fourier-transform limited (flat spectral phase) laser pulse at a central carrier wavelength of 2 µm and a Gaussian envelope with a pulse duration of 20 fs. Here, the Gaussian envelope is defined as $\sqrt{I(t)} = e^{-2\ln 2\left(\frac{t}{\tau}\right)^2}$ where $\tau = 20\,\mathrm{fs}$.

any phase slip between the envelope and the effective carrier wave, which however becomes less relevant for laser pulses with multiple optical cycles as is the case in the experiments shown in chapters 3 and 5 [151]. The same is illustrated in Figure 2.1 where $E(t)$ and the envelope are displayed separately. In real space, the $E(t)$ oscillations can be resolved into two orthogonal axes $E_x(t)$ and $E_y(t)$. On the modification of the x and y components, not only can the axis of oscillations be rotated, but they can also be made elliptically polarized when a relative phase between the two orthogonal components is introduced.

2.1.2 Pulse characterization

The laser pulses used in this thesis are well below 50 fs where a simple characterization of the pulse is no longer possible using electronic means such as using photodiodes or streak cameras. Although the spectrum of the laser pulse is easily detected by a spectrometer, its spectral phase remains unknown and can often lead to significant temporal elongation or ripples in the temporal profile of the pulse. Such modifications also lead to a strong reduction in the achievable peak intensity of the pulses.

The primary reason for this is the dispersion or how different wavelength components in broadband radiation experience different refractive indices and thereby different velocities in a medium. To obtain a more quantitative feeling for this, we look at the representation of the laser pulse in the time domain (Eqn. 2.1) to its spectral domain, which through a

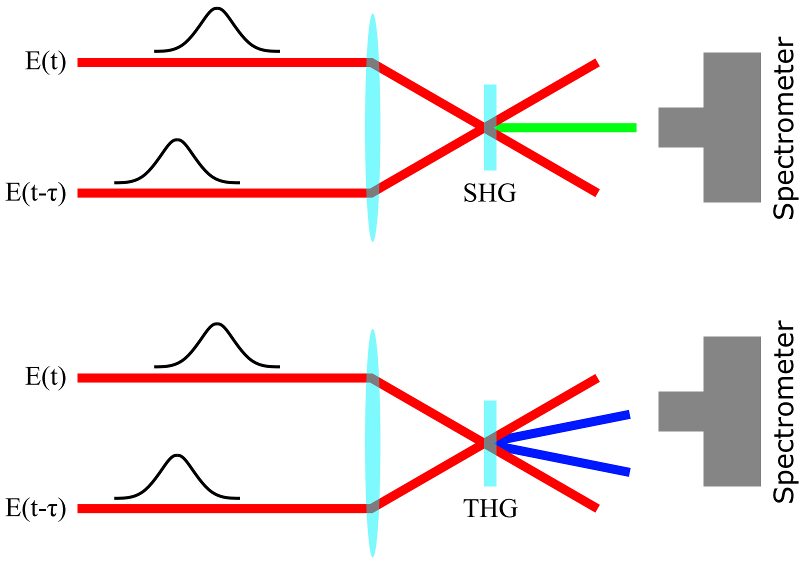

Figure 2.2: Ideal schematic representation of an SHG and THG FROG measurement, as discussed later in this thesis. The non-collinear three-wave mixing process in SHG FROG leads to a single resulting $\vec{k}$ while in the case of THG FROG, it is a four-wave process which results in two different $\vec{k}$ components and only one of them is recorded. In the actual experiment, an off-axis parabolic mirror is used for the focusing instead of a lens to avoid additional dispersion.

Fourier transform is expressed as

$$\tilde{E}(\omega) = \sqrt{S(\omega)}e^{-i\varphi(\omega)} \tag{2.2}$$

after ignoring the negative frequency component and not centering the pulse around zero frequency [151]. Here, $S(\omega)$ is the observable spectral distribution as detected by a spectrometer, and $\varphi(\omega)$ is the spectral phase which is unknown.

The widely popular 'frequency-resolved optical gating' (commonly referred to as FROG) is used to obtain the spectral phase through a complete extraction of the electric field $E(t)$, as introduced to the community by Rick Trebino and Daniel J. Kane [152, 151]. This technique relies on recording a complete spectrogram (spectrum as a function of another variable) instead of just one spectrum which is gated by a second function. Such a general spectrogram can be expressed as

$$S(\omega,\tau) \approx \left| \int_{-\infty}^{\infty} E(t)g(t-\tau)e^{-i\omega t}dt \right|^2 \tag{2.3}$$

where $E(t)$ is the pulse E-field in question, $g(t-\tau)$ is the gating function and τ is the time delay introduced between the pulse in question and the gating pulse. In reality, the FROG spectrogram is generated from an instantaneous non-linear signal between the unknown and the gate pulse, where the gate pulse is often the replica of the unknown pulse itself and is illustrated in Figure 2.2. In this thesis, two different non-linear processes are used, namely second harmonic generation (SHG) and third harmonic generation (THG) where the gating pulse is itself. The second harmonic FROG spectrogram can be expressed as

$$S(\omega,\tau) = \left| \int_{-\infty}^{\infty} E_{sig}(t,\tau) e^{-i\omega t} dt \right|^2 \tag{2.4}$$

where

$$E_{sig}(t,\tau) = E(t)E(t-\tau). \tag{2.5}$$

The unknown $E(t)$ is computed in an iterative process where $E_{sig}(t,\tau)$ is guessed, and the difference between the computed spectrogram $S_{SHG}(\omega,\tau)$ and the measured spectrogram is minimized. Similarly, for THG FROG the nonlinearity alters the spectrogram signal which is expressed as

$$E_{sig}(t,\tau) = E(t)^2 E(t-\tau) \tag{2.6}$$

or

$$E_{sig}(t,\tau) = E(t)E(t-\tau)^2 \tag{2.7}$$

depending on which of the two spatially separated THG components (as shown in Figure 2.2) are considered. This does not affect the retrieval but the recorded temporal structure of the pulse is inverted.

Although in theory, this technique works well to reproduce broadband ultrashort laser pulses, it becomes significantly error-prone once the pulse duration falls below 4 to 5 fs in the infrared region due to a drop in the nonlinear conversion efficiency where the recorded spectrum is narrower than in reality due to poor phase matching over the complete spectrum. Additionally the instantaneous response of the non-linear medium fails, which is otherwise assumed in the retrieval algorithm.

2.2 Strong light-matter interaction in gases

When intense coherent light emanating from a laser interacts with gases (atoms), it modifies the surrounding electronic states in various ways often accompanied by re-radiation of light as a fingerprint of the underlying processes. When the photon energy is close to resonance with any of the electronic states in the atom, it leads to a single or multi-photon excitation and subsequent electron photo-ionization or non-radiative and radiative relaxation. At photon energies significantly below resonance and at intensities significantly below $1 \times 10^{14}\,\mathrm{W\,cm^{-2}}$, light can be treated as a small perturbation in which multiple photons are absorbed by the electron to a virtual state (below resonance) and instantaneously relaxes to the ground state re-emitting a single photon with the total energy absorbed [10]. This can also be understood classically where the electron cloud and nuclei undergo a forced harmonic oscillation by the light field leading to the emission of harmonics through dipole oscillations and will be described in greater detail in subsection 2.3.1. However, for even

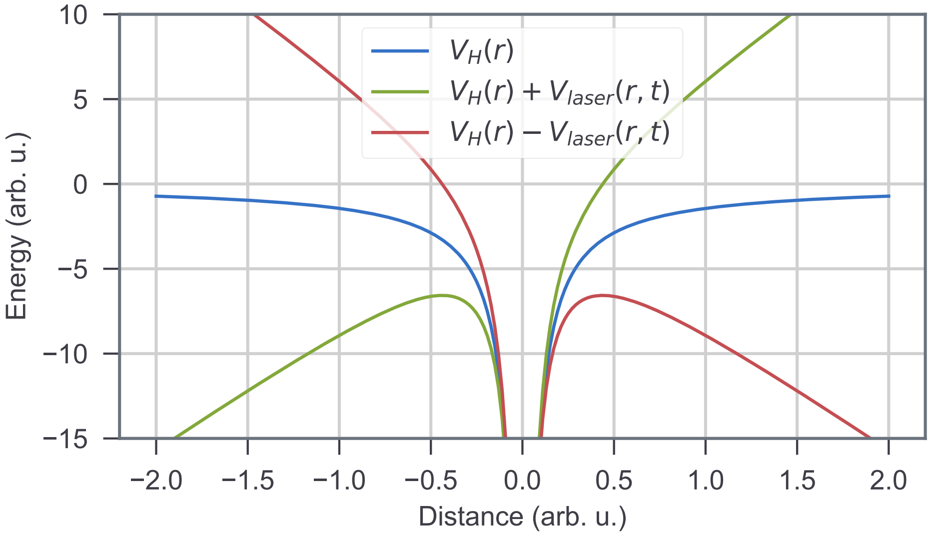

Figure 2.3: The Coulomb potential well of a valence electron in a hydrogen atom under three conditions. i) Without any additional perturbation. ii) Under the influence of a strong electric field. iii) Under the influence of a strong electric field in the opposite direction.

higher intensities, the perturbative treatment fails. To better understand the interaction of very strong light fields with atoms, an intuitive semi-classical interpretation is often used which reproduces the significant features of their interaction. Commonly referred to as the three-step-model where the first step involves laser-induced electron tunneling of the valence electron into the continuum, followed by a ponderomotive acceleration in the laser field, and finally followed by re-scattering and recombination with its parent ion to re-radiate its energy in the form of photons [28]. A brief summary of the three-step-model is presented in this section along with other relevant backgrounds as a context to the results presented in chapter 3.

2.2.1 Three step model

Laser induced tunnelling

When the laser intensities interacting with atoms are significantly strong ($\geq 1 \times 10^{14}$ W cm^{-2}), such that the electric field of the light pulse is strong enough to alter the potential well of the valence electron in the atom the linear or multi-photon ionization using a perturbative approach fails. Once the potential barrier is significantly suppressed (as shown in Figure 2.3), it enables the valence electron to tunnel through into the continuum. This constitutes the first step of the three-step model (also illustrated in Figure 2.3) and such a regime can be qualitatively identified based on the Keldysh adiabaticity parameter γ which can be expressed as [80]

$$\gamma = \sqrt{\frac{I_\mathrm{p}}{2U_\mathrm{p}}} \tag{2.8}$$

where I_p is the ionization potential of the atom and U_p is the ponderomotive energy which is further expressed as

$$U_\mathrm{p} = \frac{e^2 E_\mathrm{a}^2}{4m\omega_0^2} \tag{2.9}$$

and it quantifies the cycle-averaged energy of a free-electron in an oscillating laser field. Here, e is the electron charge, $E_\mathbf{a}$ is the electric field amplitude of the oscillating field, m is the electron mass and ω_0 is the laser carrier frequency. A value of $\gamma >> 1$ indicates a strongly multi-photon regime while $\gamma << 1$ indicates a tunneling regime. As evident from the relationships, for a given atomic species and hence ionizing potential, the intensity of the laser field and the wavelength are directly proportional to how strongly a system is in the tunneling regime.

The ionizing rate of such a system in the tunneling regime ($\gamma << 1$) is highly non-linear and is approximated in an analytical form. It is commonly referred to as the Ammosov-Delone-Krainov (ADK) tunneling rate which is related to the laser E-field as follows[3]

$$W_\mathrm{ADK} \propto C(E(t)) \cdot e^{-(2(2I_\mathrm{p})^{\frac{3}{2}}/3E(t))} \tag{2.10}$$

where $E(t)$ is the instantaneous laser E-field strength, I_p is the ionization potential of the atom and $C(E(t)) \propto 1/E(t)^{\frac{2Z}{\sqrt{2E_\mathrm{i}}}}$, where Z is the atomic charge. This relationship (Eqn. 2.10) highlights the strong non-linearity of the tunneled charge injection into continuum w.r.t the laser E-field, compared to other perturbative non-linear phenomena which are primarily sensitive to the envelope of the laser pulse [10]. Such a strong non-linearity (as evident from equation 2.10) inherently makes this process temporally restrict charge injection to sub-cycle timescales. In the case of typical Ti:Sapphire infrared lasers, the sub-cycle temporal resolutions are of the order of few attoseconds ($1\,\mathrm{as} = 1 \times 10^{-18}\,\mathrm{s}$) and stand out as one of the fastest ways to control charge forming the backbone of attosecond physics [30, 87]. Additionally, although the form of the tunneling rate does not change drastically, later reports in the literature use updated versions accounting for differences in complex atoms [150, 171].

Ponderomotive acceleration

Once the electron wavepacket tunnels out into the continuum, its propagation is defined by the time-dependent laser field $E(t)$ it experiences at the time of birth right after tunneling. This step constitutes the second in the three-step-model as depicted in Figure 2.4. This step can be treated classically by considering the electron as a point-charged particle being accelerated by the Lorentz forces in the laser fields. Depending on the time of birth of the ionized electron, it can either be accelerated only in a single direction, eventually fully escaping the parent atom and reaching maximum kinetic energies of up to $2U_\mathrm{p}$, or it can

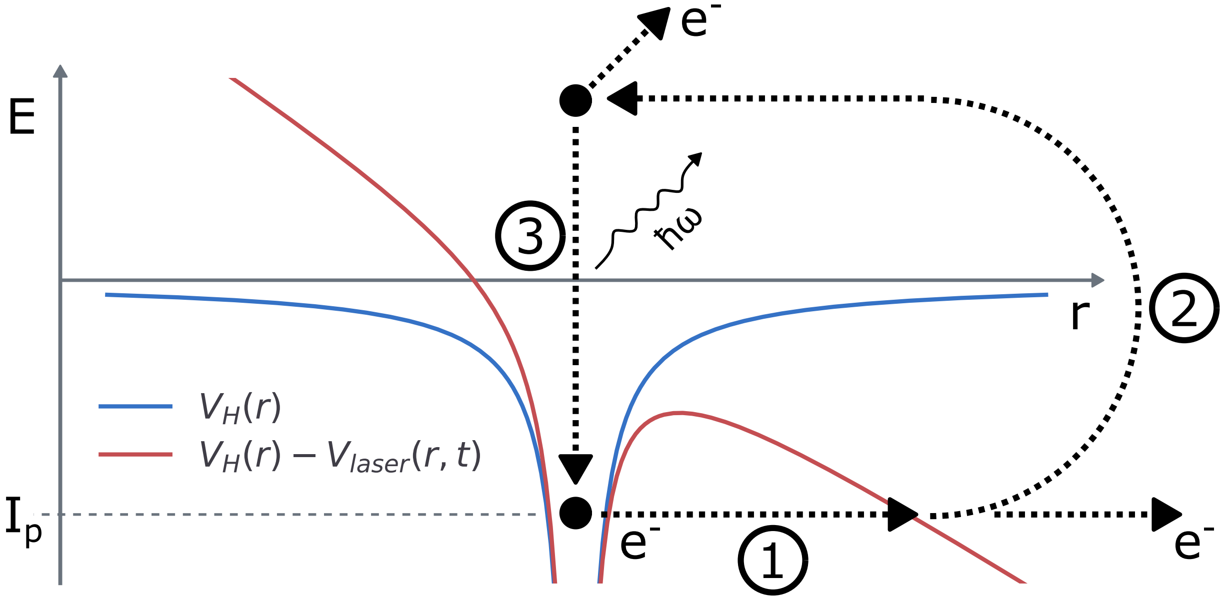

Figure 2.4: Schematic representation of the three-step-model of high harmonic generation in strong laser fields. The potential well represents a bound valence electron in a hydrogen atom as shown in Figure 2.3. Step 1 - Tunnel ionization upon significant barrier suppression by the laser field $(E(t) \cdot r)$. Step 2 - Ponderomotive acceleration of electrons in the continuum after tunneling with two possible pathways where one escapes as direct electrons and the other is accelerated back to the parent ion. Step 3 - Inelastic re-scattering of the accelerated electron with parent ion to emit photons or elastic scattering with electron emission.

turn around mid-way and accelerate back toward the parent ion with a maximum kinetic energy of upto $3.17U_\mathrm{p}$ which can all be derived analytically using Newtons laws where the velocity of the particle is given by [87, 21]

$$v(t) = -\frac{eE_L}{m_e\omega_0}[\sin(\omega_0 t) - \sin(\omega_0 t')] \tag{2.11}$$

where the laser field is defined as $E_\mathrm{L}\cos(\omega_0 t)$ and t' is the electron birth time.

Re-scattering with parent ion

The third and final step involves the electrons being accelerated back by the laser field to re-scatter with the parent ion either leading to the release of photons with a maximum energy of $3.17U_\mathrm{p}$ or elastic re-scattering which leads to final electron energies up to $10U_\mathrm{p}$ [21]. In this thesis, the characteristics of the photons generated through this process are of primary importance. Here, the classical picture with a point-like charged particle works well to reproduce the primary features of the generated photons. Namely, the chirp which is given by the kinetic energy of electrons in the field vs birth or re-scattering time, and the cutoff energy or the maximum energy of photons attainable given by $E_\mathrm{cutoff} = I_\mathrm{p} + 3.17U_\mathrm{p}$. Given the nature of a sinusoidal E-field oscillation of the laser, two electron trajectories end up with the same final re-scattering energy within a single half cycle. One takes less time and is referred to as the short trajectory and the other is the long trajectory.

2.2.2 Lewenstein model (Strong-field approximation)

Although the purely classical trajectory calculation reproduces qualitative aspects of the optical response in a strong-field regime as discussed above, it still fails to reproduce a quantitative match and other intricate features. Namely, the harmonic combs arise from interfering bursts of photon emission from each laser half-cycle. This phenomenon was first observed in 1987 by McPherson and co-workers and later succeeded by similar demonstrations up to keV photon energies [113, 96, 140].

In 1994, Lewenstein and co-workers built upon the three-step-model to develop a more general formulation that accurately reproduces the intricate features such as the combs and reaches an overall quantitative agreement within acceptable error bars while being far less computationally intensive as compared to full time-dependent Schrödinger equation (TDSE) calculations [90]. Following the same prescription, the electrons can be treated quantum mechanically, and using a single active electron approximation the TDSE in the length gauge can be expressed as [90, 89]

$$i\frac{\partial}{\partial t}|\psi(r,t)\rangle = \left[-\frac{1}{2}\nabla^2 + V(r) + r\cdot E(t)\right]|\psi(r,t)\rangle \tag{2.12}$$

where the potential due to the oscillating laser field is $r\cdot E(t)$ and $V(r)$ is the potential due to the atom. This model works well in situations where the Keldysh parameter $\gamma \leq 1$ and certain additional approximations can be made. Namely:

1. Excited bound states are neglected assuming direct tunneling of electrons from the ground state to the continuum.
2. The ground state population depletion is ignored. This assumption fails at significantly higher intensities despite the Keldysh parameter condition of $\gamma \leq 1$.
3. The atomic potential $V(r)$ is considered as only a small perturbation to the electron wavepacket in the continuum under the influence of the strong laser fields.

Intuitively, the whole three-step-model can be reformulated by considering only a small part of the ground state electron wave function being tunneled out and being propagated under the influence of the potential in the laser field. Once the wavepacket is driven back, it interferes with the ground state wave function leading to radiation of light by induced dipole oscillations. The dipole can be expressed as [90, 89]

$$D_{\mathrm{x}}(t) = e_{\mathrm{x}} \cdot \langle \psi(t) | r | \psi(t) \rangle \tag{2.13}$$

where e_x is a fixed axis. Using a saddle-point approximation, the dipole oscillation can be derived to the following form [90, 89]

$$\begin{aligned} D_x(t) \quad = \quad & e_{\mathrm{x}} \cdot -i \int_{-\infty}^{t} \mathrm{d}t' \left(\frac{-2\pi i}{t - t' - i\epsilon}\right)^{3/2} \mathrm{d}_x^*(p_s + A(t)) \\ & \times \mathrm{d}_x(p_s + A(t')) E(t') \mathrm{e}^{-iS(p_s,t,t')} + \mathrm{c.c.} \end{aligned} \tag{2.14}$$

where t is the electron wavepacket recombination time, t' the time of birth or ionization, p_s is the canonical momentum, $A(t)$ is the vector potential and d_{x} is the transition dipole moment. The term $\mathrm{d}_x(p_s + A(t'))E(t')$ accounts for the probability that the electron wavepacket tunnels into continuum under the influence of the laser field while $\mathrm{d}_x^*(p_s + A(t))$ is used to include the probability amplitude for recombination or interference of the electron wavepacket with its ground state. The term $\mathrm{e}^{-iS(p_s,t,t')}$ accounts for the phase acquired by the wavepacket when propagating in the continuum under the influence of the strong laser field until it recombines with the ground state, or from t' to t. The final resulting dipole is then obtained by the coherent sum or integral over all trajectories arising from different birth times t', which on being Fourier transformed, gives access to the high harmonic spectra.

This treatment leads to the production of a fairly accurate single atom HHG spectrum which reproduces all the essential features, especially above the I_{p} of the atom, including the plateau, the harmonic comb (for multi-cycle laser pulses) structure, the cutoff energy, and the overall spectral distribution. Given the nature of the model, harmonics below the I_{p} cannot be computed and harmonics close to it have large inaccuracies. This is primarily due to the used dipole matrix elements which rely on a scaled I_{p} according to the gas or atomic species in question, ignoring the core potential. Such an approximation works well for the higher energy regions of the harmonics which are often the focus of related studies. Hence, this model provides an appropriate platform to model experiments shown in this thesis modifying the laser field in unique ways to alter the high harmonic spectra through trajectory interference [114].

2.2.3 Macroscopic propagation effects - Phase matching

All the above-mentioned processes are described at a microcosmic single-atom level. In reality, however, the survival of the harmonics or dipole radiation strongly depends on the macroscopic environment as multiple atoms participate in this process leading to a coherent buildup (constructive interference) or destruction (destructive interference) of the radiation [136, 2]. Thus, it becomes critical to have the phase of the driving laser matched to the radiating dipole at each position within the macroscopic medium.

The phase mismatch Δk, for a certain harmonic q is usually expressed as [27]

$$\Delta k = k_q - qk_0 \tag{2.15}$$

where k_q is the wave vector of the harmonic radiation while k_0 is the wave vector of the driving laser field. In case of a phase mismatch, or $\Delta k \neq 0$, the generated harmonic yield gradually dies down as the newer harmonics are generated out of phase and the length traveled in this process is referred to as the coherent length L_c. In the process of high harmonic generation in a realistic macroscopic medium, four different parameters contribute to the mismatch (Δk) and are expressed as [91]

$$\Delta k = \Delta k_\mathrm{at} + \Delta k_\mathrm{fe} + \Delta k_\mathrm{foc} + \Delta k_\mathrm{d}. \tag{2.16}$$

The term Δk_at arises from dispersion in the atomic gas medium and contributes positively [91]. The phase mismatch for each harmonic q is expressed as

$$\Delta k_\mathrm{at} = q\frac{\omega}{c}(n_1 - n_q) \tag{2.17}$$

where n_1 is the refractive index of the fundamental driving laser while n_q represents the same for the q^th harmonic. The term Δk_fe arises from dispersion in the free electron gas (plasma) and is expressed as [91]

$$\Delta k_\mathrm{fe} = q\frac{\omega}{c}(n_1^\mathrm{e} - n_q^\mathrm{e}) \tag{2.18}$$

which has the same form as equation 2.17, but in contrast, contributes negatively as $n_1^\mathrm{e} < n_q^\mathrm{e}$. The term Δk_foc accounts for the intrinsic Gouy phase shift within the focal region of the driving laser. It is expressed as [66]

$$\Delta k_\mathrm{foc}(x, z) = -q\frac{\partial}{\partial z}\left[G(z) - \frac{kx^2}{2R(z)}\right] \tag{2.19}$$

where $G(z)$ is the phase shift along z while $R(z)$ is the radius of curvature of the beam wavefront at z. Overall, Δk_foc contributes negatively in terms of the phase shift. Finally, Δk_d is the dipole phase term that arises from deviations in the electron trajectory under the influence of the laser intensity which is imprinted on the phase of the dipole oscillation generating the harmonics. It can be expressed as [90]

$$\Delta k_\mathrm{d}(x, z) = \alpha\frac{\partial I(x, z)}{\partial z} \tag{2.20}$$

where $I(x, z)$ is the spatially varying intensity distribution. Given the intensity profile in a Gaussian focus, it reduces Δk for the harmonics generated before the focal plane (negative contribution for $z < 0$) and adds to it when generated after (positive contribution for $z > 0$).

In the macroscopic domain, these terms need to be adjusted based on their sign of Δk contribution to match the phase between the driving laser and the harmonics to allow an observable or usable yield of harmonics. Namely, the experimental parameters such as gas pressure, the position of the gas target w.r.t. the Rayleigh region, the intensity of the driving laser, and the ionization potential of the gas species all play a critical role in not only determining the absolute yield of the HHG spectra but also its spectral distribution. Additionally, certain spectral features which may be observed and understood clearly in terms of the three-step model in a single atom, may not even survive the macroscopic propagation through the medium. On the contrary, certain features observed after macroscopic propagation, may not have any physical significance on a single-atom level but purely be an artifact or feature of propagation. These points above make it essential to compare the experimental results with simulations including macroscopic propagation effects as has been shown in chapter 3 and include propagation effects in theoretical studies as reported in chapter 4.

2.3 Strong light-matter interaction in solids

2.3.1 Perturbative non-linear optics in 2D materials

Although the main results from the experiments on 2D materials in chapter 5 cannot be explained using a fully perturbative approach, a separate set of characterization measurements are also performed where the polarization-resolved second harmonic generation, which is a perturbative process, plays an essential role in positioning and finding the orientation of 2D materials within the laser-matter interaction region. A background for its expected behaviour is presented in this section.

Non-linear optics

Since the wide availability of laser sources, precise control over coherent light radiation has made extreme optical intensities reachable upon compression in space (tight Gaussian focus) and time (chirped pulse amplification) [135, 148]. When intense light interacts with matter, it gives rise to new properties which modify the propagating light. In this case, the strength of the new property is non-linearly related to the strength of the input light. To better understand the origin of such non-linearity, it is worthwhile to intuitively think of matter as a collection of atomic cores where the valence electron cloud and the nuclei undergo a dipole-like oscillation induced by the impinging light like a spring, forming the basis of the Lorentz oscillator model. In the simplest case, the light after interaction can be expressed in terms of a linear expression as

$$P(t) = \epsilon_0 \chi^{(1)} E(t), \tag{2.21}$$

where $P(t)$ is the induced polarization and $E(t)$ is the irradiated light electric field oscillating in time with a certain frequency [10]. Additionally, ϵ is the dielectric constant and χ is the electric susceptibility representing the material-specific response to light. The effective field or the electric displacement is then expressed as

$$D(t) = \epsilon_0 E(t) + P(t). \tag{2.22}$$

Within certain light field strengths, the expression can be generalized to

$$P(t) = \epsilon_0 [\chi^{(1)} E(t) + \chi^{(2)} E(t)^2 + \chi^{(3)} E(t)^3 + ... + \chi^{(\mathrm{n})} E(t)^n], \tag{2.23}$$

where the higher-order terms correspond to the non-linear response of the material. The response of the material χ is direction dependent in the case of non-isotropic material and is a tensor of rank $n+1$ where n is the order of nonlinearity. The susceptibility is classically derived in the Lorentz oscillator model. This models a single resonance frequency while a more accurate quantum mechanical model accounts for multiple higher-lying resonance frequencies which could play a role. However, for optical frequencies far below the lowest resonance, as is the case in our experiment, the classical approximation works well. Further discussions on the absolute nature of the susceptibility are omitted in this thesis as the symmetry of the system or the exact form of the $\chi_{(\mathrm{n})}$ tensor is of greater importance for the results shown later.

Second harmonic generation

The non-linear terms in equation 2.23 lead to corresponding new optical frequencies which also act as a probe of the particular non-linearity in question. The simplest is in the case of second-order non-linearity which leads to second harmonic generation and is one of the first experimentally demonstrated phenomena in non-linear optics [41]. Here, the frequency of the fundamental driving optical field is doubled which is a direct consequence of the second-order term in equation 2.23. This can be understood by first considering the optical electric field $E(t)$ oscillating at an angular frequency of ω expressed as

$$E(t) = \Re(E_0 e^{-i\omega t}) \tag{2.24}$$

$$\implies E(t) = \frac{E_0}{2}(e^{-i\omega t} + e^{i\omega t}). \tag{2.25}$$

On squaring the field as present in equation 2.23, we obtain

$$E(t)^2 = \frac{E_0^2}{4}(e^{-i2\omega t} + e^{i2\omega t} + 2) \tag{2.26}$$

where the exponents now contain a 2ω frequency doubled term and a DC component, commonly referred to as optical rectification.

Role of symmetry

The generation of the second harmonic in the section above relies on the condition that the second order susceptibility $\chi^{(2)} \neq 0$, which requires an inversion symmetry breaking in the periodic oscillation. Since the driving field is usually inversion symmetric, the breaking of symmetry here needs to be present in the crystalline structure itself. To back this statement, we look at the non-linear polarization in this case where

$$P_{NL}(t) = \epsilon_0 \chi^{(2)} E(t)^2. \tag{2.27}$$

If the field $E(t)$ is reversed or made negative in an inversion symmetry preserving system, the Polarization $P(t)$ should also change sign, implying that the expression

$$-P_{NL}(t) = \epsilon_0 \chi^{(2)} (-E(t))^2 \tag{2.28}$$

$$\implies -P_{NL}(t) = \epsilon_0 \chi^{(2)} E(t)^2 \tag{2.29}$$

is satisfied. It is now evident that the equations 2.27 and 2.29 can be simultaneously satisfied only when $\chi^{(2)} = 0$ [10].

Before diving deeper into the symmetry arguments and the need for them, it's important to realize the reason for χ being a tensor of a certain rank as highlighted earlier. In case of non-isotropic crystalline solids, depending on their structure, they may exhibit dipole oscillations with unique characteristic susceptibility (or spring constant in a classical analogy) in X, Y or Z directions, which may be arbitrarily aligned to the propagation direction ($\vec{k}$) of the optical field. The linear term for polarization $P(t)$, $\chi^{(1)}$ is a tensor of rank two, which is a 3×3 matrix, which is multiplied to a 3×1 $\vec{E}$. Similarly, second harmonic generation requires the second order non-linear term for polarization $P(t)$ where $\chi^{(2)}$ is a tensor of rank three, which is a $3 \times 3 \times 3$ tensor. However, this can be further simplified due to multiple symmetry considerations [10].

In general, where the exciting optical field has an angular frequency far lower than the resonance and χ therefore a frequency-independent parameter, the second-order polarization can be more generally expressed as

$$P_i(\omega_m + \omega_n) = \epsilon_0 \sum_{jk} \sum_{mn} 2 d_{ijk} E_j(\omega_m) E_k(\omega_n) \tag{2.30}$$

is also known as the Kleinmann symmetry condition where

$$d_{ijk} = \frac{1}{2} \chi_{ijk}{}^{(2)} \tag{2.31}$$

is a matrix in contracted notations used to simplify the 27 elements of the $3 \times 3 \times 3$ $\chi^{(2)}$ tensor. Under the assumption of Kleinmann symmetry and having $\omega_m = \omega_n$ in case of second harmonic generation resulting in the last two indices of d_{ijk} to be symmetric, $3 \times 3 \times 3$ tensor can be simplified and reduced to a 2D matrix where

$$d_{il} = \begin{bmatrix} d_{11} & d_{12} & d_{13} & d_{14} & d_{15} & d_{16} \\ d_{21} & d_{22} & d_{23} & d_{24} & d_{25} & d_{26} \\ d_{31} & d_{32} & d_{33} & d_{34} & d_{35} & d_{36} \end{bmatrix}. \tag{2.32}$$

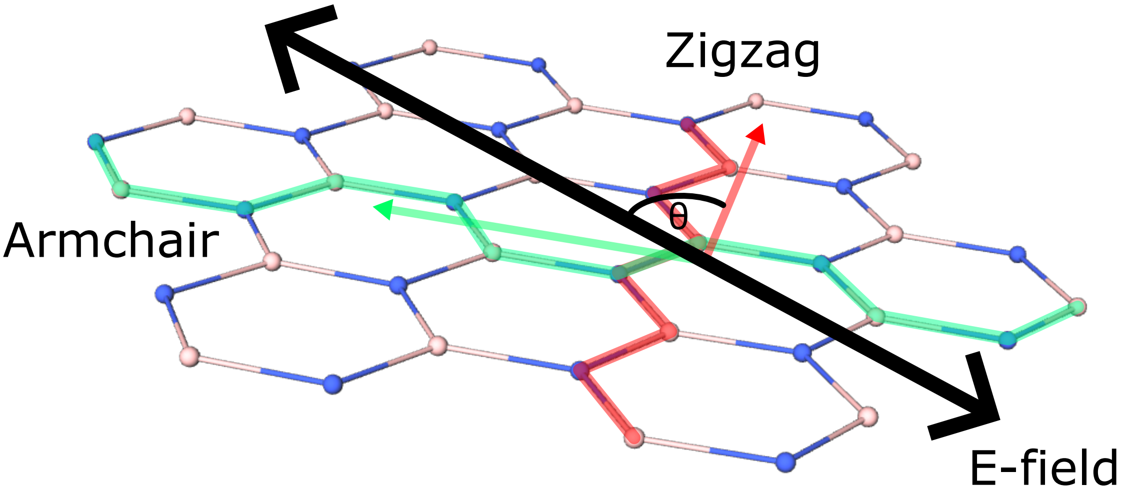

Figure 2.5: A graphical representation of hBN where the armchair and zigzag directions are highlighted in green and red respectively. The incident optical field polarization is shown in black which forms an angle θ with the Zigzag direction.

The indices jk have been merged with l with the following prescription

$$\begin{array}{lcccccc} \text{jk:} & 11 & 22 & 33 & 23{,}32 & 31{,}13 & 12{,}21 \\ \text{l:} & 1 & 2 & 3 & 4 & 5 & 6 \end{array} . \tag{2.33}$$

SHG in 2D honeycomb mono- / odd-layers

This sub-section deals with the physical phenomenon observed in monolayer hexagonal boron nitride (hBN) which exists as an inversion symmetry broken 2D honeycomb structure. Such a structure falls into the D_{3h} spatial symmetry group where for $\chi^{(2)}$, there exists only a single independent non-zero susceptibility component which is as follows:

$$\chi_{\text{hBN}} = \chi_{yyy} = -\chi_{yxx} = -\chi_{xxy} = -\chi_{xyx} \tag{2.34}$$

$$\implies -d_{21} = d_{22} = -d_{16}. \tag{2.35}$$

Using this condition, equation 2.32 can be drastically simplified and the expression in equation 2.30 can be rewritten as

$$\begin{pmatrix} P_x(2\omega) \\ P_y(2\omega) \\ P_z(2\omega) \end{pmatrix} = \epsilon_0 \chi_{hBN} \begin{pmatrix} 0 & 0 & 0 & 0 & 0 & -1 \\ -1 & 1 & 0 & 0 & 0 & 0 \\ 0 & 0 & 0 & 0 & 0 & 0 \end{pmatrix} \begin{pmatrix} E_x(\omega)^2 \\ E_y(\omega)^2 \\ E_z(\omega)^2 \\ 2E_y(\omega)E_z(\omega) \\ 2E_x(\omega)E_z(\omega) \\ 2E_x(\omega)E_y(\omega) \end{pmatrix} \tag{2.36}$$

$$\implies \begin{pmatrix} P_x(2\omega) \\ P_y(2\omega) \\ P_z(2\omega) \end{pmatrix} = \epsilon_0 \chi_{hBN} \begin{pmatrix} -2E_x(\omega)E_y(\omega) \\ -E_x(\omega)^2 + E_y(\omega)^2 \\ 0 \end{pmatrix}. \tag{2.37}$$

If the irradiated optical field is propagated in the 'Z' direction with its polarization in the XY plane with an arbitrary angle θ with respect to the 'X' axis, the corresponding E field can be expressed as

$$\begin{pmatrix} E_x(\omega) \\ E_y(\omega) \\ E_z(\omega) \end{pmatrix} = E(\omega) \begin{pmatrix} \cos\theta \\ \sin\theta \\ 0 \end{pmatrix}. \tag{2.38}$$

Using equation 2.38 in 2.37, the second harmonic polarization is simplified to

$$\begin{pmatrix} P_x(2\omega) \\ P_y(2\omega) \\ P_z(2\omega) \end{pmatrix} = \epsilon_0 \chi_{\mathrm{hBN}} E(\omega)^2 \begin{pmatrix} -\sin 2\theta \\ -\cos 2\theta \\ 0 \end{pmatrix} \tag{2.39}$$

after simplification using trigonometric identities. Further, as shown in the literature it is also useful to look at the parallel and perpendicular SHG intensity components in the frame of incident polarization. This can be obtained from equation 2.39 by multiplying a rotation matrix to the non-linear susceptibility around the z-axis following the incident polarization angle. This also translates to a case where the hBN crystal is rotated instead of the incident light polarization. The expression, in this case, is as follows

$$\begin{pmatrix} P_{\|}(2\omega) \\ P_{\perp}(2\omega) \\ P_z(2\omega) \end{pmatrix} = \epsilon_0 \chi_{\mathrm{hBN}} E(\omega)^2 \begin{pmatrix} \cos\theta & \sin\theta & 0 \\ -\sin\theta & \cos\theta & 0 \\ 0 & 0 & 1 \end{pmatrix} \begin{pmatrix} -\sin 2\theta \\ -\cos 2\theta \\ 0 \end{pmatrix} \tag{2.40}$$

which can be further simplified using trigonometric identities to

$$\begin{pmatrix} P_{\|}(2\omega) \\ P_{\perp}(2\omega) \\ P_z(2\omega) \end{pmatrix} = \epsilon_0 \chi_{\mathrm{hBN}} E(\omega)^2 \begin{pmatrix} -\sin 3\theta \\ -\cos 3\theta \\ 0 \end{pmatrix}. \tag{2.41}$$

Through equation 2.39, the unique polarization dependence of SHG from monolayer hBN or other crystals with a D_{3h} symmetry as a function of the polarization angle of the input optical field can be clearly understood. It is important to note that the derivation here assumes that the 'X' axis is oriented along the 'zigzag' axis and 'Y' along the 'armchair' axes of the D_{3h} crystal as illustrated in Figure 2.5. Except for certain differences in the nomenclature, this derivation closely follows what can be found in the literature [115, 10].

Polarization dependence of SHG from monolayer hBN ($D_{3\mathrm{h}}$ crystals)

A quantitative description of the behaviour of the polarization of SHG is presented in Figure 2.6 (a), which describes the primary feature. The plot demonstrates that the SHG

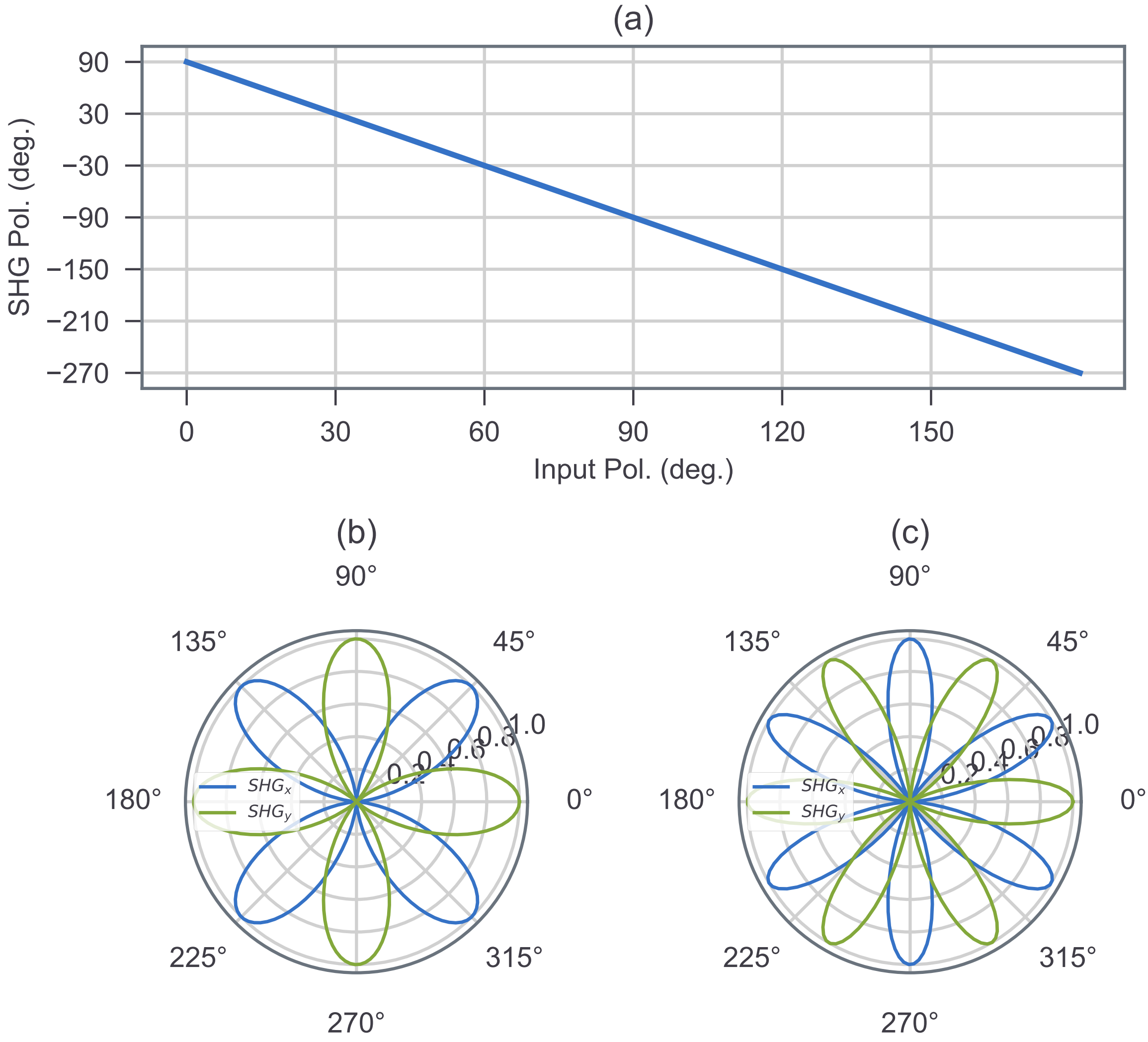

Figure 2.6: Polarization dependence of SHG in D_{3h} symmetric crystals such as monolayer hBN. Subplot (a) shows the SHG angle ($\arctan \frac{P_y(2\omega)}{P_x(2\omega)}$) as a function of the input optical field polarization angle. Subplot (b) displays the ‘X’ and ‘Y’ components of SHG intensity in the laboratory frame ($\propto P_x(2\omega)^2$ and $P_y(2\omega)^2$) also as a function of the input polarization angle rotation. Finally, subplot (c) shows the intensity of SHG in the parallel and perpendicular components ($\propto P_{\parallel}(2\omega)^2$ and $P_{\perp}(2\omega)^2$) of the incident field polarization as a function of its rotation.

polarization angle (‘Y’ axis) scales with a factor of two, and in the opposite direction as compared to the input optical field polarization angle (‘X’ axis). Additionally in this plot, one can also observe that whenever the input polarization is aligned along the zigzag direction (0°, 60°, 120°, 180°....), the SHG is polarized perpendicular to the input. Similarly, when the input polarization is along the armchair direction (30°, 90°, 150°, 210°....), the

SHG is polarized parallel to the input polarization.

Figure 2.6 (b) represents the SHG intensities $P_x(2\omega)^2 \propto \sin^2 2\theta$ and $P_y(2\omega)^2 \propto \cos^2 2\theta$ (equation 2.39) as a function of the input polarization rotation about the z-axis, which shows a four-lobe structure as a characteristic signature of the hBN crystal with D_{3h} symmetry and is the observable recorded in the experiments as shown in the later sections. A rotation of the hBN crystal is imprinted as a rotation on the four-lobe structure as an angular offset and has been used in the literature to probe the structure of such materials [174]. Experimentally realizing this scheme is rather straightforward as it is enough to rotate the input polarization and keep all the other elements such as the crystal and a polarizer/analyzer at a fixed angle, although it is not as straightforward to extract the exact angle of rotation of the crystal compared to another.

Figure 2.6 (c) represents the SHG intensities $P_{\|}(2\omega)^2 \propto \sin^2 3\theta$ and $P_{\perp}(2\omega)^2 \propto \cos^2 3\theta$ (equation 2.41) as a function of the input polarization rotation about the z-axis, which turns out to be a six-lobe structure as a characteristic signature of monolayer hBN or other D_{3h} crystals and has been more commonly used in the literature to probe the orientation of such structures [97, 133]. A rotation of the hBN crystal in this particular case with respect to another is directly proportional to the angular offset that is obtained in the six-lobe structure. However, experimentally this is more challenging to record since the sample needs to be rotated. For arbitrarily distributed small grain sizes of the order of 10 microns, this was not achievable. Additionally, this may be probed by rotating two elements (incident polarization and a polarizer/analyzer) at the same time, which is also difficult to control precisely. Other clever techniques can be utilized in a reflection geometry where the SHG is split off using a beamsplitter after reflection. The incident light here is required to be circularly polarized which eventually goes through a polarizer, which also acts as the analyzer at the same time. On the downside, the use of an additional beamsplitter is undesired when working with short pulsed light due to dispersion or in polarization-sensitive experiments due to strong phase shifts and reflectance differences between ‘s’ and ‘p’ polarization components on dielectric surfaces.

2.3.2 Band structure of 2D materials

As atoms come close together to form molecules, the electron orbitals with distinct energy levels split up in multiple closely spaced levels to form hybridized molecular orbitals, with the electrons populating in line with Pauli’s exclusion principle. When more and more atoms are brought close to each other extending over large areas such as in solids, repeated discrete splitting in energy levels keeps occurring, forming wide bands instead of a single discrete energy level [84]. The bonding region of the band forms the valence band while the anti-bonding band forms the conduction band and in between lies a forbidden region (depending on the material), commonly referred to as the band gap. The magnitude of the band gap defines whether the material behaves like an insulator (large band gap), a semiconductor (small band gap), or a conductor (no band gap) [84].

This section provides a background on the band structure of two-dimensional (2D) solid-state systems which are closely linked to the material being investigated in this

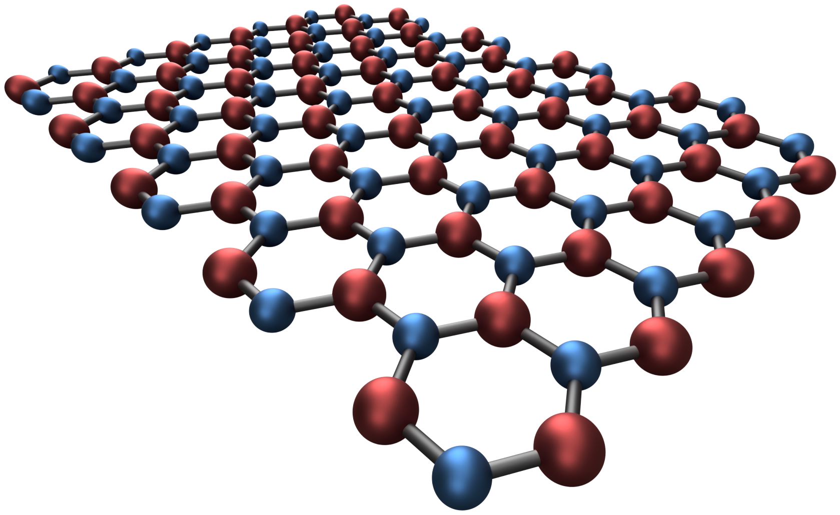

Figure 2.7: A real-space illustration of a 2D material with a hexagonal chicken wire lattice and alternating species of atoms on each node leading to a broken spatial inversion symmetry.

thesis. Namely, the focus here is on 2D hexagonal lattices and a brief discussion on a well-investigated 2D hexagonal system like Graphene is a useful precursor.

In real space, the Graphene lattice is made up of six carbon atoms forming a hexagonal chain, repeated infinitely in the form of an atomic monolayer sheet. Three of the four valence electrons in Carbon are used to form three sp^2 hybridized bonds with other Carbon atoms. The fourth electron occupies the p_z orbital which sticks out of the plane and its interaction with the neighboring p_z orbitals leads to the formation of the most interesting and physically relevant low-energy band structures in Graphene. The two neighboring atoms form a unit cell with a as the spacing between them. Given the 2D form in real space, unlike the previous discussion, the momentum vectors also span over two axes k_x and k_y. The band structure in this case turns out to be a surface that is a function of k_x and k_y while the Z axis represents the energy. The hexagonal structure in real space maps to a hexagonal Brillouin zone in momentum space and their high symmetry points are highlighted in table **??**.

Valley physics - role of symmetry

The electronic properties of Graphene are primarily governed by the overlap of the p_z orbitals forming the π bands. The corresponding band structure is theoretically constructed using a tight-binding approach where the Hamiltonian includes a parameter t_1 which ac-

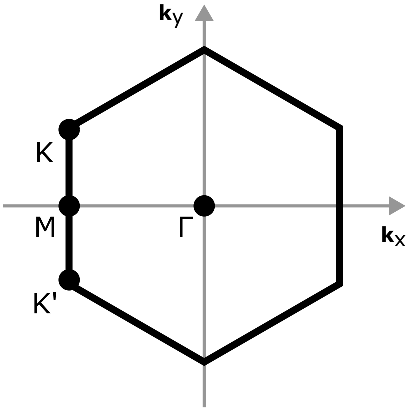

label	wave vector
$\mathbf{\Gamma}$	$0k_x + 0k_y$
$\mathbf{M}$	$(2\pi/\sqrt{3}a)k_x + 0k_y$
$\mathbf{K}$	$(2\pi/\sqrt{3}a)k_x + (2\pi/3a)k_y$
$\mathbf{K'}$	$(2\pi/\sqrt{3}a)k_x - (2\pi/3a)k_y$

Figure 2.8: A graphical representation of the significant points in k-space in a hexagonal Brillouin zone with a as the lattice constant.

counts for the electron hopping between the three nearest neighbors of each Carbon atom in the 2D lattice. This has been commonly shown in the literature and the resulting energy dispersion relation takes the following form

$$|E(k)| = t_1\sqrt{1 + 4\cos\left(\frac{\sqrt{3}k_x a}{2}\right)\cos\left(\frac{k_y a}{2}\right) + 4\cos^2\left(\frac{k_y a}{2}\right)}. \tag{2.42}$$

On plotting equation 2.42 as a function of k_x and k_y over the whole Brillouin zone, one can observe the unique band structure $E(k)$ where the conduction and valence band form deep conical valleys (degenerate in energy) and intersect each other at the K and K' points (see Figure 2.9 (a)). The implications of this for its electronic properties have been a subject of research for many years and any further discussion on it is omitted in this thesis [45]. Instead, this thesis deals with a 2D system that is closely related but exhibits a clear gap at the K and K' points in the Brillouin zone.

Most 2D materials apart from Graphene exist in the same hexagonal format but with two different atomic species next to each other such as hexagonal Boron Nitride (hBN) or transition-metal (M) dichalcogenides (X) of the form MX_2 and commonly referred to as TMDCs or TMDs (see Figure 2.7). The slightly varying potential at the two neighboring atoms leads to a different onsite energy where Δ is the difference. This modifies the original Hamiltonian and dispersion relation (equation 2.42) in a way that leads to a new dispersion relationship given by

$$E_\Delta(k) = \pm\sqrt{E(k)^2 + \Delta^2}, \tag{2.43}$$

which explains the gap opening (proportional to Δ) at the K and K' points (see Figure 2.9 (b)). Consequently, this also breaks the spatial inversion symmetry of the system which is a necessary precursor for realizing valley contrasting physics [163, 166].

---

[2] The calculations have been performed using the code provided at `https://github.com/topocm/topocm_content`

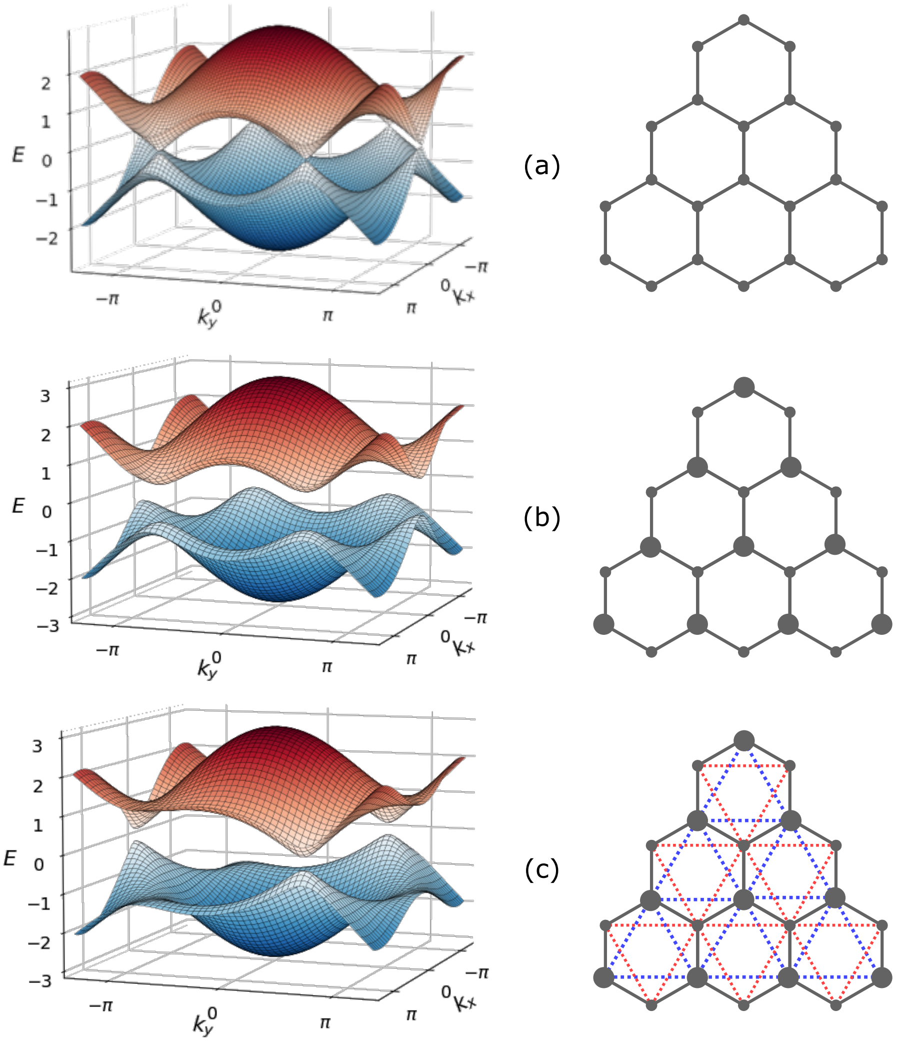

Figure 2.9: Bandstructure of 2D materials under various symmetries calculated using a tight binding model[2]. The figures on the left show the conduction band (red) and valence band (blue) as a function of crystal momentum in a hexagonal Brillouin zone, while on the right side the illustrations depict the real-space configuration of the 2D hexagonal lattice which the tight-binding model is based on. (a) A Graphene-like lattice with equal onsite energy at each atomic site with a full probability of electron hopping between each neighboring site. In momentum space, this leads to the famous Dirac cones as observed in Graphene where the conduction and valence bands touch each other at the K and K' points in the Brillouin zone. (b) A spatial inversion symmetry broken configuration due to unequal onsite energy between two neighboring atoms, similar to a situation where the atoms themselves are different as in TMDCs or hBN. In momentum space, this leads to an opening up of the Dirac points and the formation of a band gap and valleys at the K and K' points. (c) In addition to spatial inversion symmetry, the time-reversal symmetry is broken by introducing a complex next to the nearest hopping parameter t_2, where the pathways are graphically indicated by dotted lines in blue and red. The sign of t_2 indicates the chirality or direction of the hopping, resulting in the closing/opening of the other valley.

2.3.3 Valleytronics

Although the valleys (possessing a direct band gap) in spatial inversion symmetry broken 2D materials are identical in their dispersion and energy, they possess a crucial parameter that distinguishes them. Namely, the valley pseudospin, which gives rise to new optical 'valley' selection rules [167, 162]. TMDCs in particular are in the spotlight given their applicability as semiconductors but with a unique way to address the electron population in each valley, paving the way for 'valleytronics' [137, 155]. The valley pseudospin gives rise to the selective excitation of electrons into a specific valley (K or K') by weak and resonant left or right circularly polarized light [163, 162, 106].

Theory of non-resonant valleytronics

Very recently in 2020, Álvaro Jiménez-Galán and co-workers theoretically demonstrated a scheme in which far-off resonance 'tailored' light fields were used to realize valley selective electron population [76]. Their fundamentally new and path-breaking proposal forms the basis of our experimental undertaking discussed in detail in chapter 5, and hence this subsection is dedicated to a discussion on their report. Their approach uses hBN[3] as a model system given its gapped Graphene-like band structure with a large band gap $\approx 5.9\,\mathrm{eV}$ along with a driving laser photon energies of $0.41\,\mathrm{eV}$ ($\lambda = 3000\,\mathrm{nm}$) and lower.

The authors achieved this theoretically by using a laser pulse with its E-field tailored in the form of a trefoil structure in the XY polarization plane, which closely resembles the shape of a triangular sub-lattice of hBN, i.e. a B-B-B or an N-N-N lattice. A more detailed description of the pulses with two-color bi-circular fields can be found in subsection 5.2.1. Such a pulse at significant strengths can break the time-reversal symmetry and result in significant band-structure modification where the band gap at the two valleys (K and K') further closes down or opens out. This is explained using the Haldane model where in addition to the nearest neighbor electron hopping parameter t_1 introduced earlier, a complex next-to-nearest electron hopping parameter t_2 can be used to transform a trivial system into a topological one by the light field, which in-turn allows selectively population of the valleys (K or K') through unequal ionization probabilities due to a band gap modification [54]. Control over the magnitude and phase of t_2 is established as a function of rotation of the cycle-averaged trefoil laser pulse which modifies the Berry curvature and the cycle-averaged band structure of hBN. The relationship between t_2 and the laser field has been derived as [76]

$$\mathscr{I}\{\bar{t_2}\} \sim 2J_2\left(\frac{\sqrt{3}\ a_0\ F_1}{\omega}\right) J_1\left(\frac{\sqrt{3}\ a_0\ F_2}{2\omega}\right)\cos\varphi \tag{2.44}$$

where $\mathscr{I}$ is the cycle averaged imaginary component of t_2, a_0 is the crystal lattice constant, F_1 and F_2 are the electric field strength of the fundamental and second harmonic bi-circular fields respectively used to construct the trefoil pulse, while ω and 2ω are the fundamental and second harmonic angular frequencies. Finally, φ is the phase delay between the two-color pulses which controls the rotation of the tre-foil and subsequently the cycle averaged

---

[3] MoS_2 was also investigated as a secondary material

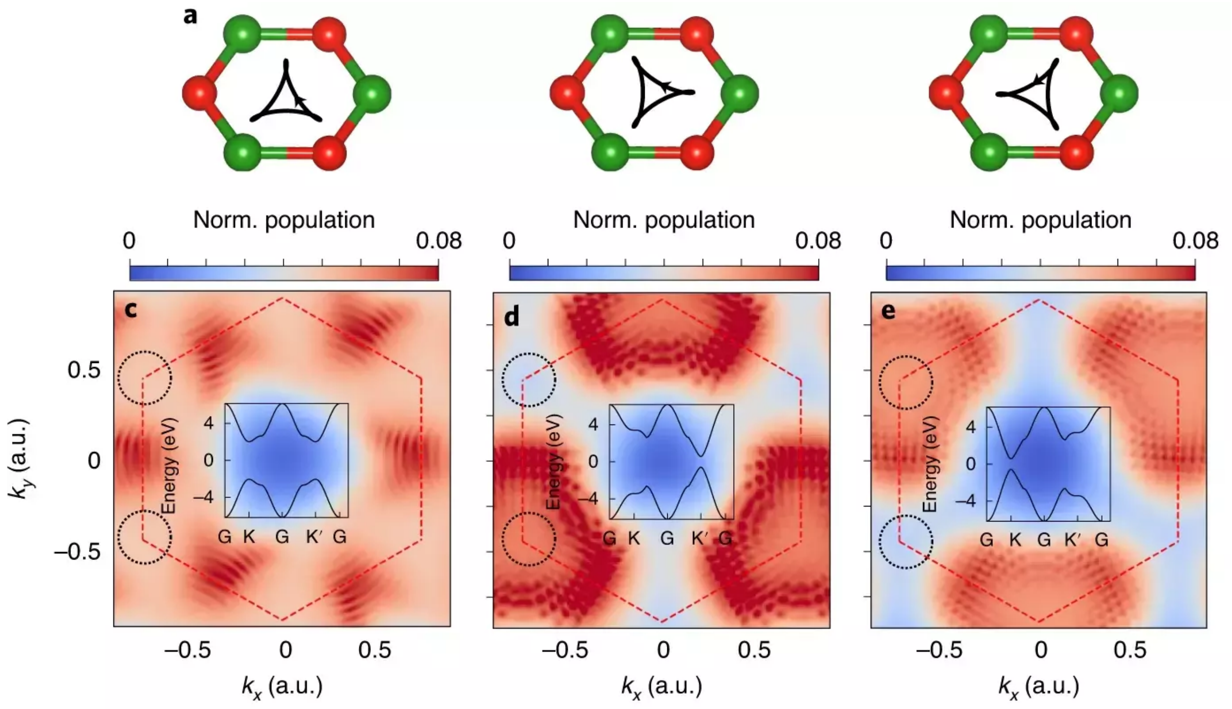

Figure 2.10: Theoretical demonstration of off-resonant lightwave valley selection and optical readout by Jiménez-Galán et al [76]. a) Real-space illustration of the hBN lattice with the trefoil laser pulse orientation. c)-e) Electron population in the p_z conduction band of hBN over the momentum space for respective orientations of the trefoil laser pulse with respect to the hBN lattice while the inset shows the respective band structure modification, especially at the valleys. Reproduced with permission from Springer Nature.

t_2 parameter. The computed changes in the band structure and the subsequent population in the conduction band are shown in Figure 2.10 for a fundamental pulse with a wavelength of 3 µm at a pulse duration of 200 fs and a field ratio $F_1/F_2 = 2$. J_n is a Bessel function of order n. Additionally, numerical calculations were performed to simulate the laser pulse interaction with hBN and the calculated population of the conduction band with respect to the trefoil pulse rotation is also shown in subplots c-e in Figure 2.10. The details of the calculation can be found in the literature [145, 76].

2.3.4 Optical probing of valley population

In TMDCs, previous works in the field have convincingly demonstrated the existence of a Valley-Hall effect [108]. Here an in-plane applied electric field generates currents at the two valleys K and K' in the orthogonal directions opposite to each other due to the anomalous Hall conductivity, which is proportional to the population contrast [118]. An equal population of the Valleys leads to a net deflection which is zero, but an imbalance, as produced by a resonant circularly polarized light, leads to a net current which has been measured as a transverse Hall voltage [106, 108]. Additionally, people have also measured it fully optically by high-harmonic generation using terahertz laser pulses [88].

Anomalous Hall conductivity

In this thesis, the prescription by Jiménez-Galán and co-workers is used where an optical probing of the valley polarization is achieved without using strong terahertz laser pulses [76]. In this prescription, an additional linearly polarized probe pulse is used at the same wavelength of fundamental (ω) to induce an anomalous Hall conductivity as a fingerprint of the valley polarization, which is eventually imprinted in the helicity of the harmonics produced by the probe pulse. The anomalous Hall conductivity σ_{xy} can be expressed as [162, 108, 76]

$$\sigma_{xy} = -\frac{e}{\hbar} \sum_n \int_{\mathrm{BZ}} \frac{\mathrm{d}\mathbf{k}}{(2\pi)^3} f_n(\mathbf{k}) \mathit{\Omega}_{n,z}(\mathbf{k}) \tag{2.45}$$

where the integral runs over crystal momentum k covering the full Brillouin zone (BZ). The integral is further summed over multiple bands differentiated with the index n. Apart from the common universally recognized constants, $f_{\mathrm{n}}(k)$ and $\Omega(k)_{\mathrm{n,z}}$ represent the electron population and the Berry curvature, respectively, of the n^{th} band. The results from numerical simulations shown in Figure 2.10 only include two bands arising from overlapping p_{z} orbitals although computations using higher bands have not produced significant deviations. As evident from equation 2.45, a non-zero anomalous conductivity (AHC) arises whenever there is a difference in electron population between the K or K' valleys. In the case of an equal population of the valleys, the AHC cancels out when integrated over the whole Brillouin zone due to equal and opposing AHC due to the equal and opposing Berry curvatures.

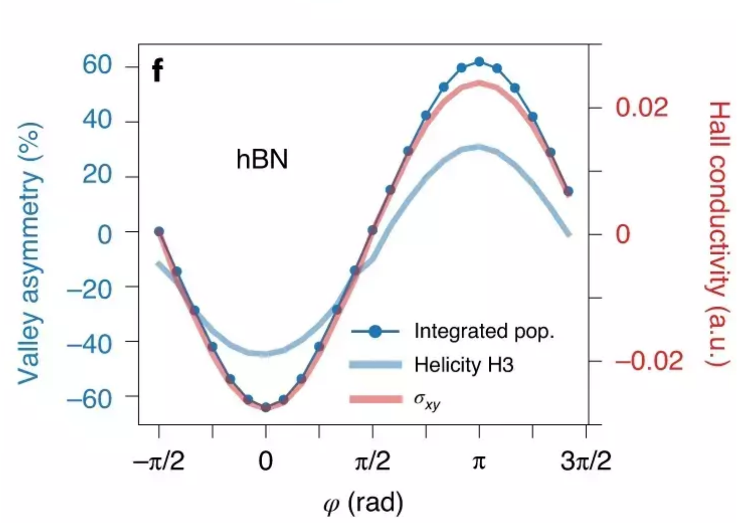

Figure 2.11: Theoretical demonstration of optical readout (valley polarization) through harmonic helicity detection in hBN by Jiménez-Galán et al [76]. The anomalous Hall conductivity, asymmetry in integrated valley population (as shown in Figure 2.10), and asymmetry in helicity of the third harmonic of a linearly polarized probe are all plotted against the rotation of the trefoil pump pulse. Reproduced with permission from Springer Nature.

Mapping of anomalous currents with helicity of harmonics

In the literature, the effect of a linearly polarized probe pulse right after the trefoil pump pulse to readout the valley polarization is described and understood semi-classically [144, 76]. The intraband harmonics generated by a linearly polarized probe pulse depend on the motion of the electrons in the conduction band. When the probe is polarized in the y direction, the vector potential of the field $\mathbf{A}_\mathrm{L}(t)$ (where the laser field $\mathbf{E}(t) = -\partial\mathbf{A}_\mathrm{L}/\partial t$) modifies the electron wavepacket momentum and it can be expressed as

$$\mathbf{k} = \mathbf{k}(t) = \mathbf{k}_\mathrm{i} + e\mathbf{A}_\mathrm{L}(t) \tag{2.46}$$

where $\mathbf{k}_\mathrm{i}$ is the initial momentum of the electron wavepacket. Hence, the motion of the wavepacket along the y axis can be expressed as

$$\dot{\mathbf{r}}_n(t)\hat{e}_y = \nabla_\mathbf{k}\varepsilon_n(\mathbf{k}(t)) \cdot \hat{e}_y \tag{2.47}$$

for the n^{th} energy band where $\varepsilon_n(\mathbf{k}(t))$ is the band energy dispersion. However, the presence of a non-zero Berry curvature $\mathbf{\Omega}(\mathbf{k}(\mathbf{t}))$ results in a deflection of the motion in the perpendicular direction x and can be expressed as

$$\dot{\mathbf{r}}_n(t)\hat{e}_x = e\mathbf{E}(t) \times \mathbf{\Omega}_n(\mathbf{k}(t)) \cdot \hat{e}_x \tag{2.48}$$

where e is the electron charge. As evident here, when the population is equal at both the valleys, the transverse deflection occurs in opposite directions as $\Omega(K') = -\Omega(K)$, leading to net-zero anomalous currents. However, in case of an imbalance where $\Omega(K') \neq |\Omega(K)|$, one direction dominates. Along with the direction, a phase difference is also introduced between the two x and y components. The phase difference can be intuitively understood as originating from a phase difference in oscillations arising from the dependence on the vector potential $\mathbf{A}_{\mathrm{L}}(t)$ in equation 2.47 while equation 2.48 is dependent on the electric field $\mathbf{E}(t)$ which can go up to $\pm\pi/2$ due to an intrinsic integral or differential nature of their relationship as they result in switching from a 'sin' to 'cos' function or vice-versa. This results in the harmonic emission becoming elliptical, and additionally with the helicity changing sign when the higher populated valley switches to the other valley. The numerically computed helicity which results from this behaviour is shown in Figure 2.11, where the behaviour of the outgoing helicity is plotted against the trefoil pump rotation. In particular, the helicity of the third harmonic should be measured (probe pulse has the same fundamental wavelength as in the pump pulse) as this occurs with a higher signal as compared to higher harmonics, but at a frequency ($3N\omega$) from which no harmonic emission is expected from the bicircular pump given that it is an emission channel banned by the selection rules.

Chapter 3

Controlling XUV combs with strongly tailored laser fields

3.1 Introduction

This chapter, which has already been published [114], closely follows the content presented along with further details on the methods used for investigation. Namely, this chapter deals with high harmonic generation (HHG) using intense laser pulses which have long proven to be an extremely reliable source of high-energy, ultrashort, and coherent light radiation ranging from UV to soft X-ray region [113, 96, 130]. As understood by the three-step model, HHG is a highly nonlinear process, which is strongly dependent on the electric field shape of the driving laser [29]. As a consequence, the most common approach to modify or control the temporal structure, spectral density, and yield of HHG has been through altering the driving laser field. A prominent application of such control is in the production of isolated attosecond pulses by restricting the re-scattering process within a single half-cycle using a gate in intensity [87] or polarization of the driving fields [48]. Other techniques involve mixing with an additional weak laser frequency component or color, which perturbs the fundamental laser field to either modify or probe the highly non-linear ionization probability, suppress electron re-scattering by an induced ellipticity of the laser field, or use phase matching properties unique to multi-colored fields [37, 85, 11, 157, 35].

In contrast to numerous previous experimental works using the secondary color as a weak perturbation, here, the focus is a regime that involves significant modification of the driving electric field structure in a linearly polarized configuration. A strong deviation from the usual sinusoidal shape of the laser field leads to significantly altered ionization times, electron trajectories, and their recollision kinetic energies. A few works carried out in a similar regime on two-color control have reported various degrees of control over the HHG spectrum. The synthesis of a fundamental with its strong second harmonic component was shown to produce a strong cutoff energy oscillation [112, 73] and an overall shift of central energy of the HHG spectrum as a function of the waveform [111]. The overall shift in HHG spectral density was shown to be further enhanced under certain conditions, resembling a swallowtail caustic within a parameter space of relative field strength, phase-delay of the two-color driver, and photon energy [132]. Theoretical works have explored two-colour HHG numerically and analytically over a large range of parameters, and different parent atoms [116, 42]. Additionally, others have reported on the effect of unconventional non-Gaussian temporal pulse envelopes [55] and the role of atomic Coulomb potential on the spectral density brought about by two-colour HHG [9]. Such control has already found applications in high-harmonic spectroscopy to probe multi-electron effects in noble gases [39, 40].

This chapter builds on the existing literature and investigates the suppression of individual harmonics in HHG driven by an ω-2ω field, where simultaneous suppression of odd and even order harmonics are observed. Generally, only even harmonics are suppressed in a single color driver, while none are suppressed in ω-2ω drivers as shown in the literature for weakly perturbing two-color pulses [37, 33]. The behaviour of this unique suppression is studied as a function of the driving waveform controlled by the relative phase delay. The resulting spectra are then reproduced with strong-field approximation (SFA) calculations including macroscopic and propagation effects. The degree of agreement between the experiment and SFA calculations is quantitatively extracted using a fitting procedure. Furthermore, intuitive semi-classical calculations qualitatively reproduce the suppression and hint at interference effects between harmonic emissions from subsequent laser half-cycles. The experiment and calculations are repeated for an ω-3ω configuration, given its difference in subsequent half-cycle symmetry. Finally, a detailed semi-classical analysis of spectral modulations obtained in each half-cycle of ω-2ω and ω-3ω configurations are used to identify the mechanism responsible for the observed peak suppression in the former.

3.2 Methods

3.2.1 Multi-harmonic interferometer

A critical pre-requisite of HHG is the availability of high-intensity laser pulses which are usually obtained by temporal compression. The current gold standard of achieving this is through using broadband amplified laser pulses which can be compressed to a few femtoseconds. The HHG experiments in this chapter not only require enough intensities to generate HHG, but also sufficient pulse-energy to generate three perturbative harmonics (ω, 2ω and 3ω) to interferometrically combine them for strong laser field tailoring. To realize this, a commercial amplified Ti:Sapphire laser system from Spectra-Physics (formerly Femtolasers) was used, as elaborated in Figure 3.1. The laser pules obtained from the source are centered around 780 nm, temporally compressed down to 25 fs and a pulse energy of $\approx 800\,\mu$J.

At these pulse energies, the 25 fs pulses possess sufficient intensities to produce phase-matched harmonics in non-linear crystals without spatial tight-focusing [10]. The multi-harmonic interferometric scheme used here closely follows the scheme already used within the group for a different experiment [13]. The interferometer was, however, redesigned and

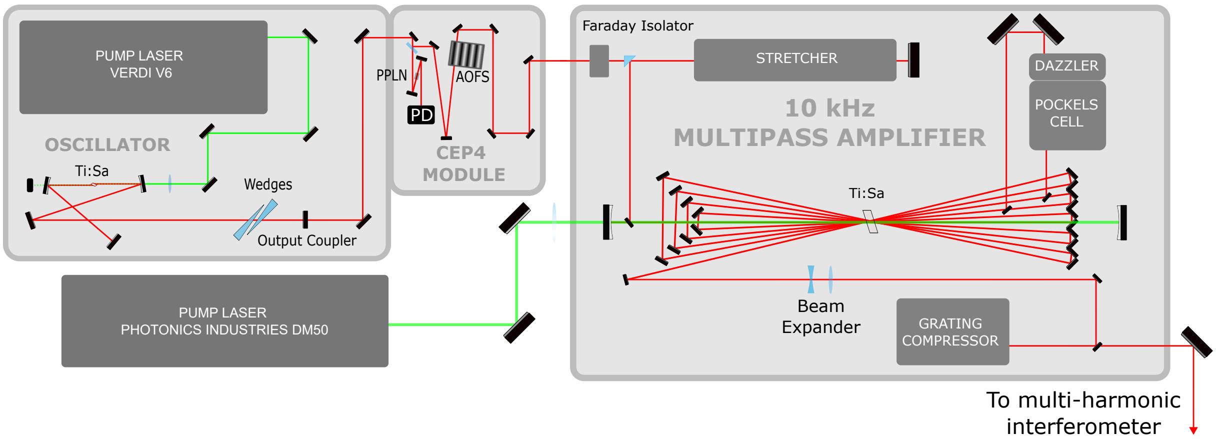

Figure 3.1: Commercial carrier-envelope-phase (CEP) stable 10 kHz Ti:Sapphire laser setup from Spectra-Physics (formerly Femtolasers). The mode locked output of the Ti:Sapphire oscillator (top right) goes through a feed-forward CEP stabilization module [102]. Next, the laser pulses go through a multipass Ti:Sapphire chirped pulse amplifier (CPA) designed to operate at 10 kHz with an average power output ≈ 8 W [148]. The chirped seed pulses make nine round trips through the laser-pumped Ti:Sapphire gain medium before being expanded and compressed using a grating pair. The pulses are temporally compressed down to ≈ 25 fs.

re-built to further reduce the optical path length and thereby significantly improve the interferometric stability of the HHG experiments. The first step involves producing SHG, where the polarization of the incoming ω (780 nm) pulses are adjusted (using a $\lambda/2$ plate) and subsequently undergo type-I phase-matching in a β-Barium Borate[1] (BBO) crystal to produce 2ω [10]. As governed by type-I phase-matching, the 2ω component is generated cross-polarized w.r.t. ω. Subsequently, a birefringent quartz crystal is used to adjust the time delay between ω and 2ω pulses as a function of its tilt (or medium thickness) for achieving maximal temporal overlap [135]. Another $\lambda/2$ plate is used to rotate the polarization of 2ω and make it parallel to ω. Finally, the beams propagate through a second BBO[2] to produce the third harmonic (3ω) by sum frequency generation (SFG) also with type-I phase-matching, which is a very efficient approach for generating 3ω [78, 69]. This scheme is illustrated in Figure 3.2.

Once the harmonics ($\omega, 2\omega, 3\omega$) are collinearly generated in the first stage, they are fed into the interferometer and separated using custom coated beamsplitters as illustrated in Figure 3.2. This allows the delay arms of the interferometer to host additional waveplates and polarizers to further filter the polarization state of the harmonics. This is due to the use of birefringent crystals such as BBO and quartz in the multi-harmonic generator which often introduces ellipticity or reduces the polarization contrast ratio of the beams by

---

[1] This crystal is cut at 27.2 deg and is 200 µm thick

[2] This crystal is cut at 44.3 deg and has a thickness of 100 µm

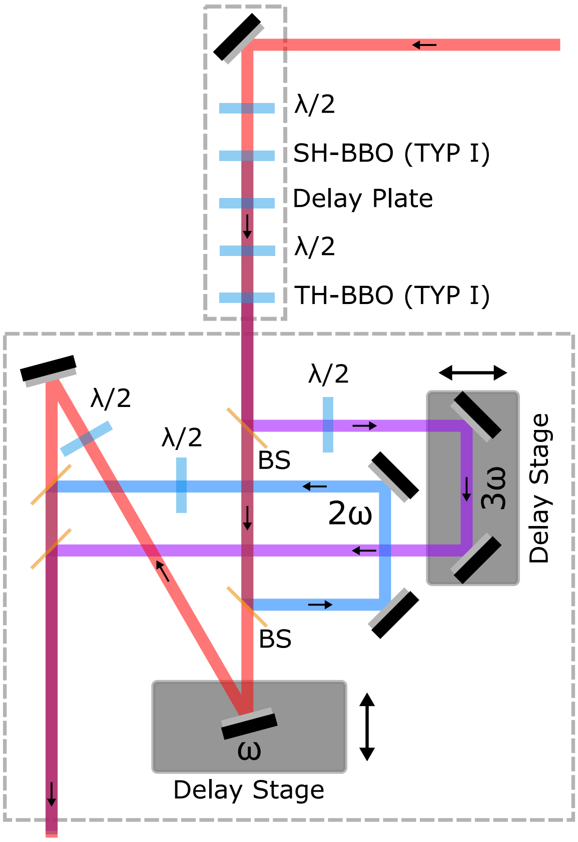

Figure 3.2: Schematic representation of the multi-harmonic interferometer used for HHG using tailored laser fields. The top section (indicated by the dashed box) represents the stage where the fundamental generates its second and third harmonic in a co-propagating configuration. The bottom section consists of a three-arm Mach-Zehnder type interferometer designed to independently control the time-delay and polarization state of each harmonic as marked by ω, 2ω, and 3ω. The interferometer has been slightly modified for greater stability from its original design published previously [13].

behaving like a waveplate. Precise individual control over the individual polarization states of the beams allows complex laser field structuring in both polarization axes. Following this, two arms bounce off delay stages, mounted on piezo stick-slip nanopositioners (Smaract GmbH) enabling precise time delay control between the arms. Finally, the beams from all three arms re-combine in a collinear path leading to the focussing optics and eventually to the AS-X beamline as depicted in Figure 3.4. This combination of efficient harmonic generation coupled with precise time delay, polarization, and power control forms the backbone of precise and strong light-field tailoring, using which, multi-color E-field tailored HHG is further investigated.

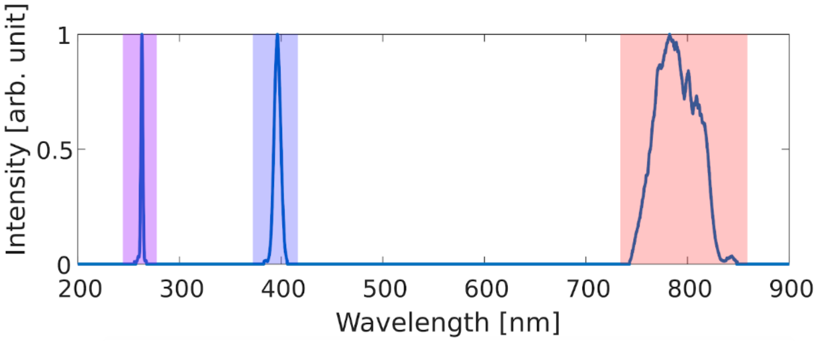

Figure 3.3: Spectra of the three harmonics ($\omega, 2\omega, 3\omega$) generated with the multi-harmonic interferometer (normalized) recorded right before the beams enter the AS-X beamline. The harmonics are centered around 780 nm, 390 nm and 260 nm, while their pulse energies were determined to be 265 µJ, 65 µJ, and 35 µJ, respectively.

3.2.2 AS-X beamline

The harmonics generated in the experiments highlighted in this chapter reach photon energies of up to 80 eV where they become significantly absorptive in air and other mediums [64]. Additionally, to make sure that the harmonics are generated purely from a chosen gas or atomic species, it becomes essential to carry out the entire experiment in a vacuum environment. Thus, in order to perform this, a vacuum beamline (AS-X) was built to study HHG under the influence of strongly tailored light fields. The scheme and design of the beamline are shown and briefly discussed in Figure 3.4 which only includes XUV beam characterization devices (XUV spectrometer and multi-channel plate coupled with a phosphor screen to observe the spatial profile), but could easily be coupled to an experiment for using such a source by replacing XUV spectrometer (McPherson Model 248/310) with an experimental vacuum chamber. Additionally, as observed in the third vacuum chamber from the left, a CMOS sensor (Figure 3.4, label 4) images the HHG target for monitoring and alignment of the laser pulses through the HHG target, which is critical for diffraction-free efficient generation of the harmonics. The implementation of a differential pumping scheme through the separation of different pumped vacuum chambers connected through a narrow opening allows vacuum levels on the order of 1×10^{-8} mbar in the experimental chamber despite having HHG target pressures up to 400 mbar. Given the driving wavelength and the achieved intensity estimates, neon was used as the medium for HHG to prevent ground state saturation issues given its high ionization potential (21.6 eV) allowing easier interpretation of the obtained results [21].

3.2.3 Experiment

As motivated in the introductory remarks in this chapter, the primary objective is to significantly tailor the laser pulses in terms of their sinusoidal electric field structure. The

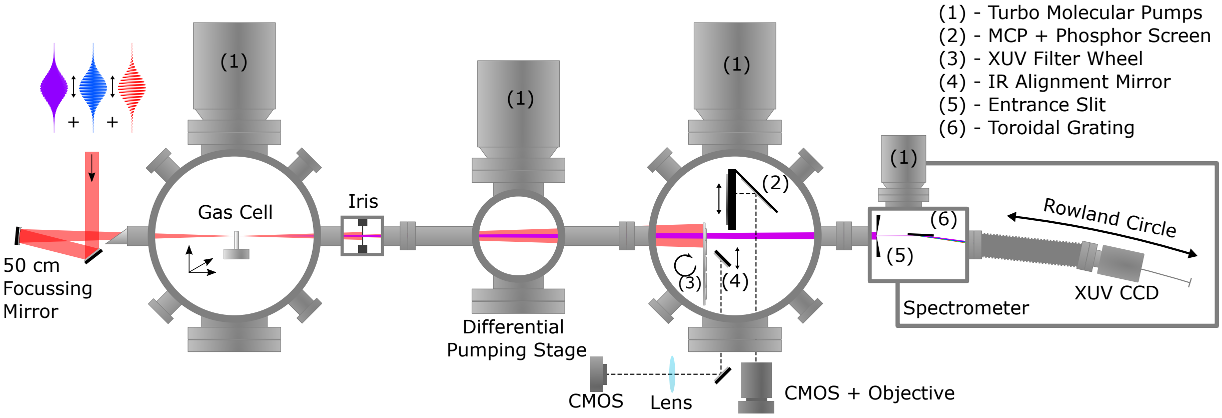

Figure 3.4: The AS-X beamline for experiments in vacuum on HHG with gases and their spectral and spatial characterization. The first vacuum chamber on the left is used to generate the harmonics in a gas target (stainless steel cylindrical target with a thickness of 1.5 mm) where the pulses from the multi-harmonic interferometer are focused into. Subsequently, the generated harmonics and the fundamental beam passes through an iris to block the high gas load in the first vacuum chamber. After propagating further in a vacuum through a differential-pumping stage the XUV harmonics are transmitted while a thin metallic filter blocks the fundamental beam in the third chamber. This chamber also features a multi-channel plate (MCP) and phosphor screen arrangement to characterize the XUV beam profile. Finally, an XUV spectrometer (Mcpherson Model 248/310) is connected to the beamline where a slit is imaged and dispersed by a flat-field grating onto a CCD, mounted on rails to accommodate a large spectral range.

tailoring is achieved by the multi-harmonic interferometer where two harmonics are interferometrically combined ($\omega - 2\omega$ or $\omega - 3\omega$), which critically depend on the temporal and spatial overlap of the harmonic arms. During the experiment, a coarse temporal overlap is first achieved by placing a BBO crystal at a suitable angle right after the multi-harmonic generator where the SFG signal between $\omega - 2\omega$ and $\omega - 3\omega$ indicates the overlap. The beams from the multi-harmonic interferometer are focused into the AS-X beamline using a 50 cm custom-coated triple-band concave mirror. Their spatial overlap at the focus is coarsely aligned by placing an intercepting mirror to image the focus with a CMOS sensor. This also serves the purpose of characterizing the focal spot size of the harmonic arms and is illustrated in Figure 3.5 where their waist diameters ($2w_0$) are 59 µm (ω), 39 µm (2ω) and 35 µm (3ω). The precise temporal and spatial alignment is performed in situ by observing the two-color high harmonics produced as both the two-color combinations ($\omega - 2\omega$ and $\omega - 3\omega$) lead to a strong fluctuation in the overall HHG yield due to suppression or enhancement of the tunnel ionization probability of the electrons in the two-color laser field [111].

A novel aspect of this work is in terms of the strength of the two-color ratio where the additional harmonic has a large contribution. To highlight the difference in such a regime, the relative power between the two-color arms was scanned by misaligning the respective

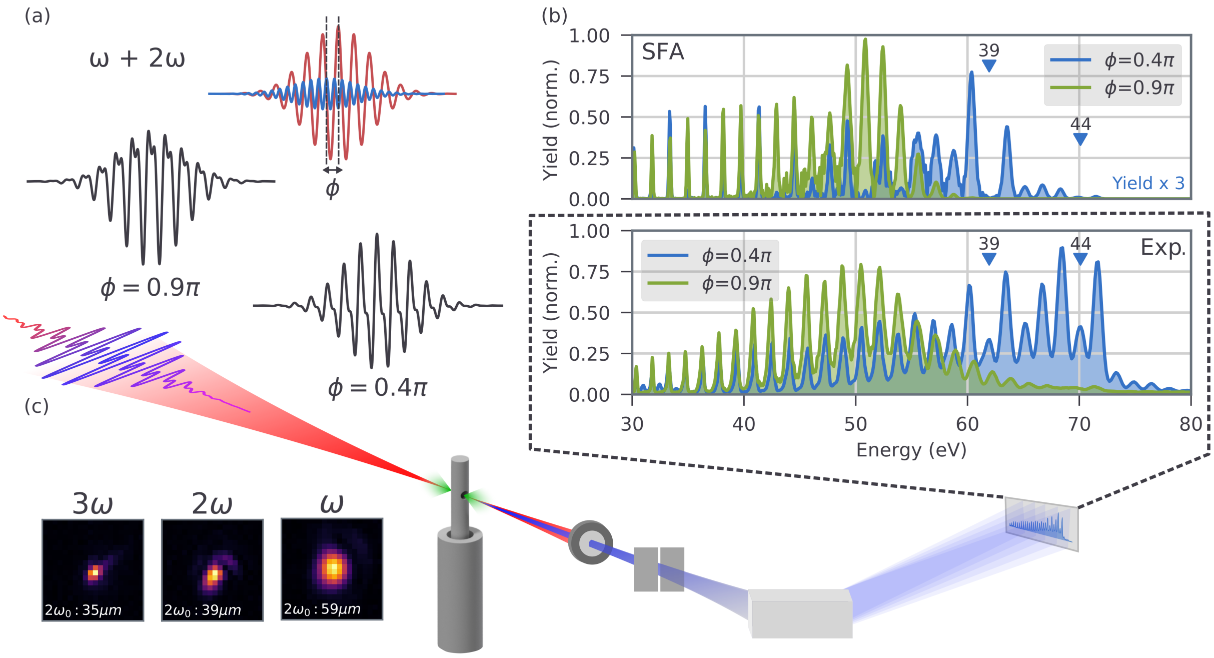

Figure 3.5: Phase-dependent single harmonic modulation in the HHG spectra generated by a two-color driving field. (a) Illustration of waveforms resulting from an ω-2ω field at a phase-delay of 0.4π and 0.9π. (b) The respective HHG spectra were obtained experimentally and from macroscopic SFA calculations. The spectrum obtained from simulations for $\phi = 0.4\pi$ has been magnified in yield by a factor of 3 for better visibility and comparison. The solid arrow markers indicate two examples of harmonic suppression occurring for an even and odd harmonic simultaneously. (c) A schematic overview of the experimental setup and beam profiles of each color at the focus. The HHG spectra for ω-3ω driving fields are generated in a similar fashion. This figure has been reproduced from [114].

BBO crystal in the multi-harmonic generator. Alternate techniques like using a continuous gradient neutral density filter or irises were avoided as they induce changes in the wavefront of the laser pulses leading to additional uncertainties in the experiment given that HHG is a highly non-linear process. The misalignment of a BBO does tend to slightly shift the central wavelength, but this is theoretically estimated to be maximally around 10 nm (for 2ω) and 5 nm (for 3ω) using the package Lab2 [12]. In addition, theoretical semi-classical calculations (described in the later sections) demonstrate the insignificance of this spectral shift on the overall reported results. Eventually, the HHG spectra are recorded for multiple parameter values of relative intensity and harmonic wavelength, all as a function of the time delay between the different color arms. Although the signal-to-noise ratio of the XUV spectrum is good enough, the spectrum is recorded while continuously scanning over 4 fs and averaged over a period of 5 min, beyond which instabilities in the interferometer start to wash out the delay-dependent features in the HHG spectrum.

3.2.4 Theoretical modelling

To understand the mechanisms responsible for the results obtained with the experimental techniques mentioned above, they were numerically reproduced using the description in this section. As outlined in the publication of this work, a generic tailored two-color pulse can be mathematically defined as [114]

$$E(t) = G_{env}(t) \cdot \frac{E_0}{1+R}(\cos(\omega t) + R\cos(N\omega + \phi)) \tag{3.1}$$

where $R = \frac{E_{N\omega}}{E_\omega}$ signifies the magnitude of the two-color mixture and thereby defines the degree of waveform modification. The variable $N = 2$ and 3 stands for an ω-2ω and ω-3ω configuration, respectively, ϕ is the time delay or phase delay introduced by the interferometer delay arms between the two colors or harmonics, G_{env} is the Gaussian pulse envelope, and E_0 is the peak field strength of the tailored pulse.

Macroscopic SFA simulation

As a first step, the experiments are theoretically reproduced with macroscopic SFA simulations, where the time-dependent dipole response of an atom is calculated from an analytic description, as described in section 2.2.2 [90]. The code is authored by Maximilian Högner, where a full macroscopic propagation (considering cylindrical symmetry) of the single-atom dipole radiation is calculated, including its far-field projection, as obtained in an experiment and has already been used in previous works [67, 138]. In addition to propagation effects, the saturation of the ground state is also taken into account [16]. More specifically, the infrared driving field (P_{IR}) and the generated XUV pulses (P_{XUV}) in the gas medium are propagated using a first-order propagation equation in co-moving coordinates at vacuum speed of light, having the form [67]

$$\partial_z E_{IR/XUV} = -\frac{ic}{2\omega}\Delta_\perp E_{IR/XUV} - \frac{i\omega}{2c\epsilon_0}P_{IR/XUV} \tag{3.2}$$

where z is the propagation direction [67, 31]. Here,

$$P_{IR} = P_{IR,\ lin} + P_{Kerr} + P_{plasma} \tag{3.3}$$

where P_{IR} includes linear effects, such as absorption and linear refraction, and nonlinear effects include spectral blue shifting, defocusing due to plasma formation [46] and lensing along with self-phase modulation due to the Kerr effect [10]. Similarly,

$$P_{XUV} = P_{XUV,\ lin} + P_{dipole} \tag{3.4}$$

comprising of the linear response and a dipole component from SFA calculations. After propagation through the gas-filled target, the XUV component or dipole response is numerically propagated to the far field until it reaches the spectrometer as illustrated in Figure 3.5(c). When passing through the spectrometer slit at the entrance of the spectrometer, the XUV beam is vertically cropped in the experiment and is also accounted for in the numerical results. This particularly becomes important as the two-color phase (ϕ) also alters the divergence of the XUV beam, eventually leading to a slightly modified spectral modulation with ϕ [60]. Also as used in the experiment, the transmission function of the aluminium filter[3] for blocking the driving laser pulses is taken into account to produce a more realistic spectrum for comparison with experimental data [63].

Semi-classical calculation

Although the SFA calculations produce results that can be quantitatively compared with the experimental results, the underlying physical mechanisms responsible for certain behavior are hard to pinpoint. Hence, to shed light on the underlying physics, additional semi-classical calculations were performed. Using the three-step model with a two-color driving pulse [29], the harmonic emissions from two subsequent half-cycles are individually computed in the time domain, analogous to the dipole response in the case of SFA calculations [90, 164]. The energy spectrum and spectral phase are similarly obtained by a Fourier transform, which is essential for obtaining the harmonic peaks and other modulations in spectra from the coherent addition of emission from multiple half-cycles, which is an essential aspect in understanding the results reported in this work [114].

The simplified temporal response for each half-cycle burst can be expressed as

$$d(t_R) = \sqrt{W(t_B)\frac{dt_B}{dt_R}}e^{j\frac{1}{\hbar}S(t_B,t_R)} \tag{3.5}$$

where t_B and t_R are the time of electron birth and time of electron recollision respectively. They are obtained by classical propagation of the electron trajectories (as point-charged particles) in the laser field. The trajectories acquire a classical phase as it propagates and eventually recollides, and the phase can be expressed as

$$S(t_B, t_R) = \int_{t_B}^{t_R} E_{KE}(t)dt + I_P(t_R - t_B). \tag{3.6}$$

Some of the other components in equation 3.5 are $W(t_r)$ which is the Ammosov-Delone-Krainov (ADK) tunneling rate [150, 171], I_P is the ionization potential of the atom species used in the gas target, and $E_{KE}(t)$ is the instantaneous kinetic energy of the electron. The semi-classical approach described here predominantly favors long-trajectories over the short, in contrast to the experiment where long-trajectories are more sensitive to intensity variations given the longer time they spend in the laser field and hence are suppressed due to intensity averaged dephasing in the focal volume leading to an inaccurate estimation of the correct HHG rate [129, 7]. However, their qualitative depiction of the spectral modification due to the contribution of each half-cycle remains unaffected [112, 73, 111].

---

[3] It is assumed that the filter is partially oxidized as is the case when being exposed to atmospheric conditions over time. Hence, a 50 nm thick layer of Al_2O_3 is considered along with 150 nm thick Al.

3.3 Results and discussion

3.3.1 Harmonic suppression in symmetry-broken fields (ω-2ω)

The suppression of individual harmonics in the two-color (ω-2ω) HHG XUV comb beyond 60 eV, as highlighted in Figure 3.5(b), is the focus of this work. Usually, in the single-color HHG spectrum, a plateau of harmonic combs is followed by an exponential drop-off in yield near the cut-off [30, 87]. The rising behavior of HHG with energy observed in Figure 3.5(b) is due to the XUV transmission function of a thin aluminium filter (used to block the driving laser), which is followed by a sharp cutoff near its absorption edge around 73 eV. Another characteristic feature is a significant difference in the spectral density of two complementary waveforms where $\phi = 0.4\pi$ and 0.9π. The variation in spectral density with ϕ simultaneously over multiple harmonics, causing a forked-like structure near the cutoff, has already been observed in earlier works [112, 111, 132], and has been attributed to the modification of recolliding electron trajectories and hence their kinetic energies as well. Sometimes this can also lead to significant enhancement in the spectrum well below the classical cutoff, resembling swallowtail caustics for R larger than 0.44 [132]. The global change of spectral density in two-colour HHG has also been discussed in [111], while a strong modulation of the harmonic cutoff energies has been discussed in [112]. The suppression of individual harmonics, however, remained unexplored in previous experimental works and is a novelty of this report and other recently published work [114].

A selection of $\phi = 0.4\pi$ in Figure 3.5 represents the waveform where the harmonic emission rate is similar to the subsequent half-cycles, leading to a strong peak suppression behaviour. The other choice of $\phi = 0.9\pi$ represents a waveform with a strongly suppressed harmonic emission rate from subsequent laser half-cycles, and corresponding to an experimental spectrum with minimal HHG peak suppression as shown in Figure 3.5(b). Usually, these conditions are intuitively expected to occur at $\phi = 0.5\pi$ (and π), where the ionization probability (ADK) is indeed equal (and alternating) in magnitude in the subsequent laser half-cycles, however, it also needs to be considered that the ionization probability density shifts in time as well. This phenomenon results in electrons with the same recollision kinetic energy in subsequent laser half-cycles and experiences different regions of the probability density function, leading to unequal (and not fully alternating) electron recollision rates, as shown in theory in the literature [42].

The observed harmonic suppression is investigated in greater detail by measuring the experimental HHG spectra over a set of phase-delays ($0 < \phi < 2\pi$), which covers all the unique waveform configurations of an ω-2ω field for a fixed value of R. The obtained spectra are illustrated by a 2D false-color plot (Figure 3.6(a)). The parameter scan over ϕ in Figure 3.6(a) also shows the transition between 0.4π and 0.9π, where a gradual increase or decrease in contrast of certain harmonics is visible beyond 60 eV. The supplementary information in Ref. [132] includes phase plots obtained under similar experimental conditions but their limited resolution makes it rather difficult to infer such features. The theoretically predicted two-color HHG rates in Ref. [42] strongly resemble the data presented here. A strong nontrivial interference pattern leading to suppression of individual harmonics is also

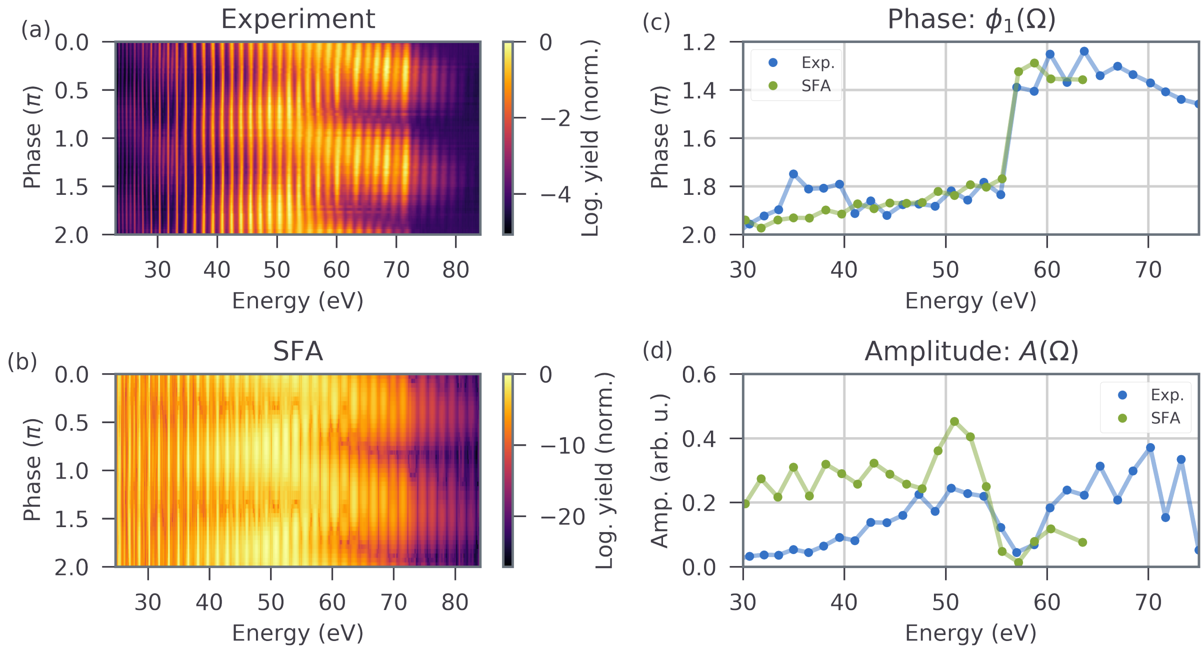

Figure 3.6: Modulation of HHG spectra as a function of relative phase-delay in symmetry-broken two-color laser fields (ω-2ω). (a) The experimentally measured HHG spectra as a function of phase delay and XUV energy. (b) Macroscopic SFA calculations for $R = 0.23$ and $I = 3 \times 10^{14}\,\mathrm{W\,cm^{-2}}$. The data in (a) and (b) are both normalized to their respective global maxima. (c) Comparison of harmonic-dependent HHG yield-modulation-phase (parameter $\phi_1(\Omega)$ from fit function as described in the text) in the experimental and calculated HHG spectra. (d) Comparison of the corresponding amplitude (parameter $A(\Omega)$), as generated by the fitting procedure from the normalized values in (a) and (b). The figure is reproduced from [114].

visible, however, the mechanisms responsible are not discussed in detail. The experimental observations are further reproduced using macroscopic SFA calculations as described in subsection 3.2.4 using close-to experimental parameters and are shown in Figure 3.6(b) for $R = 0.23$. The phase (ϕ) axis in the experimental plot has been readjusted to match the simulation. This assumption is justified due to the absence of any absolute waveform detection in the experiment. Here, a clear modulation in single harmonics appear at the same energies and relative phase (ϕ) as observed in the experiment.

The degree of correlation between the experiment (Figure 3.6(a)) and the macroscopic SFA calculations (Figure 3.6(b)) is quantitatively determined using a fitting procedure. The modulation in yield for each individual harmonic as a function of phase-delay (ϕ) between the colors is extracted and fit to a Fourier series of the following form [114]:

$$f_{fit}(\phi, \Omega) = A(\Omega)\cos(\phi + \phi_1(\Omega)) + B(\Omega)\cos(2\phi + \phi_2(\Omega)) + C(\Omega) \tag{3.7}$$

which captures the complete ϕ and Ω (harmonic frequency) dependent HHG spectra and converges well with negligible error. The first term in equation 3.7 maps the single prominent modulation below 55 eV and then continues further after a phase jump near higher energies. The second term in equation 3.7, with twice the periodicity, resolves the prominent forked structure, which appears beyond 55 eV as observed in Figure 3.6(a) and (b). Although it is necessary to use the two terms for a fit convergence, the coefficients of the first term are found sufficient for a quantitative comparison between experiment and theory. The term $A(\Omega)$ signifies the magnitude of the fundamental modulation component as extracted from the normalized spectra in Figure 3.6(a) and (b). Similarly, $B(\Omega)$ indicates the magnitude of the second oscillation component which plays a role in fitting the modulations around 55 eV, while $C(\Omega)$ is a DC offset to account for the non-modulating part of the signal. The coefficients $B(\Omega)$ and $C(\Omega)$ are non-zero and obtain approximate maximum values of 0.1 and 0.5, respectively, at harmonics around 54 eV. Although essential for the fit, one of the amplitude coefficients is found to be enough for a quantitative correlation between the experiment and SFA calculations. The phase offset terms $\phi_1(\Omega)$ and $\phi_2(\Omega)$ signify the phase drift of the respective oscillation components. In particular, $\phi_1(\Omega)$ is found to be a useful parameter, which accurately maps the gradual phase shift of the fundamental oscillation component in the experiment and calculated data (see Figure 3.6(c)). A small change in the peak intensity or parameter R of the calculated HHG spectra results in large observable shifts in $\phi_1(\Omega)$, thereby serving as a sensitive marker for correlation.

A direct comparison with their coefficients in Figure 3.6(c) and (d) quantitatively exhibit good correlation. As compared to $\phi_1(\Omega)$, a larger deviation is observed in $A(\Omega)$. Given the complex balance of phase-matching parameters playing a role in the macroscopic build-up of HHG in the gas medium, small errors in the theoretical modeling can lead to large differences in the calculated spectral density [129]. The slight difference observed in $\phi_1(\Omega)$ near 35 eV can be attributed to the second-order diffraction of the same spectrum from the spectrometer grating overlapping onto the first. A peak detection algorithm is used to restrict the fitting only to the harmonics for the correct unwrapping[4] of the phases ($\phi_1(\Omega)$) extracted from each. Beyond 65 eV, the peak detection scheme for the simulated spectra fails to obtain a fit given the low signal in this region. The increasing deviation in yield (also evident in $A(\Omega)$) between the experiment and calculations near the cutoff energy remains an open question. The exact pressure at the gas target is hard to determine accurately in the experiment, which could result in inaccurate phase-matching conditions in the simulations for a certain spectral region.

The good quantitative correlation between experiment and theory lets us accurately fix critical parameters like intensity, the relative field strength of the two color configuration (R), and absolute phase ϕ. These parameters are further used in semi-classical calculations to intuitively understand the mechanisms responsible for the rich interference features observed at certain values of ϕ (see Figure 3.7). They also provide an insight into the general structure of the pattern intuitively, where re-colliding electrons form two distinct

---

[4] Discrete jumps larger than 2π or its multiples are subtracted or added to minimize its difference with the previous value

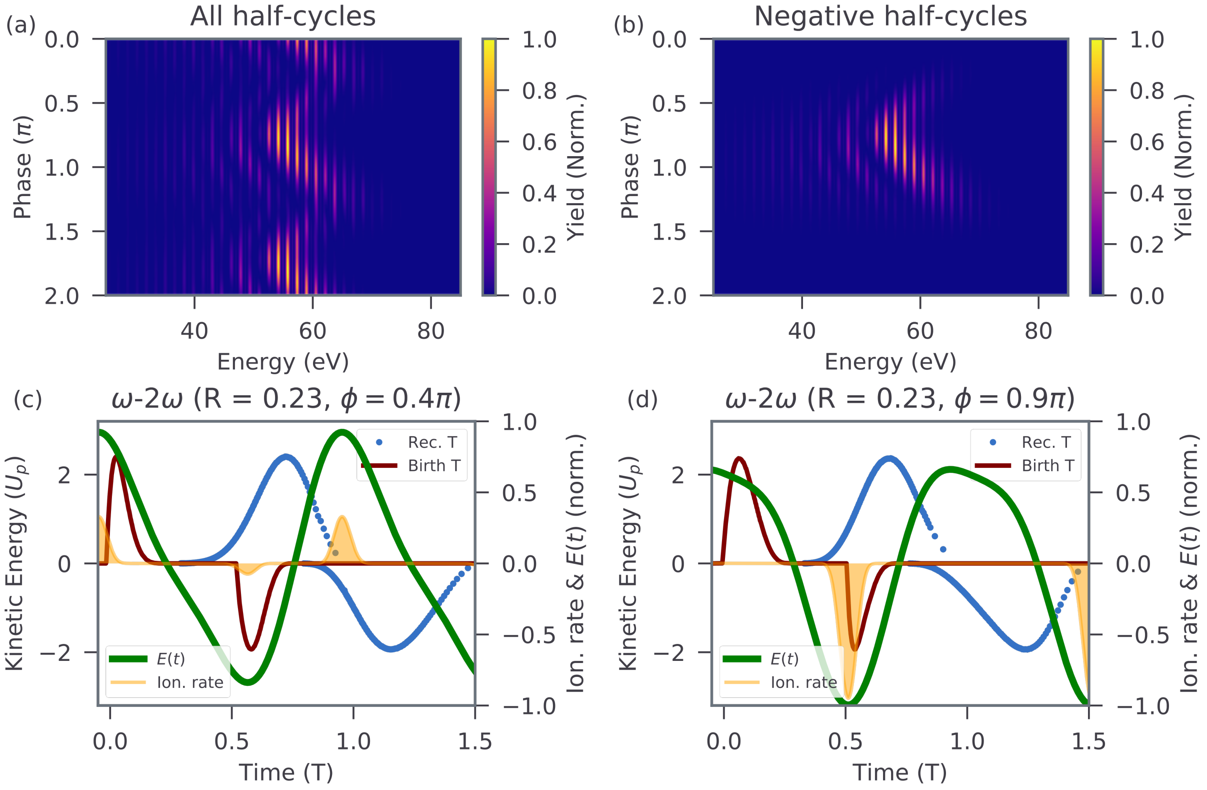

Figure 3.7: Semi-classical HHG rate for two-colour symmetry-breaking fields (ω-2ω). (a) Harmonic emission is calculated from classically recolliding electrons as a function of ϕ from two subsequent half-cycles, coherently added over three complete laser cycles. (b) Harmonic emission exclusively from negative half-cycles, coherently added over three complete laser cycles. (c), (d) Analytically calculated time-dependent electron recollision energies as a function of their time of birth (Birth T) and their time of recollision (Rec. T) in 1.5 laser cycles. Also shown are the respective ionization rate (ADK) and electric field shape for a phase-delay of $\phi = 0.4\pi$ (c) and $\phi = 0.9\pi$ (d). The energy axis has been normalized to the ponderomotive energy (U_p), while the ionization rate has been normalized to the highest among all values of ϕ. The negative values on the y-axis have been used only to decouple the emission directions. The figure is reproduced from [114].

plateaus and two cutoff structures arising from two subsequent half-cycles of the laser field as shown in Figure 3.7(a) and (b) as a fork shaped structure. However, close to $\phi = 0.4\pi$ and 1.4π, the additional modulation pattern disappears in Figure 3.7(b), which shows calculations for only emission from negative half-cycles. This hints at an inter-half-cycle interference at play. The time-energy structure of the classical electron recollisions for two complementary phase-delays (ϕ) are shown in Figure 3.7(c) and (d), which in case of $\phi = 0.4$ highlights the comparable ionization rate of harmonic emission (recolliding electrons) from subsequent half-cycles. However, the time-energy structure of the recolliding electrons, including the cutoff, is significantly different. In comparison, at $\phi = 0.9$, the harmonic emission is largely restricted to a single half-cycle.

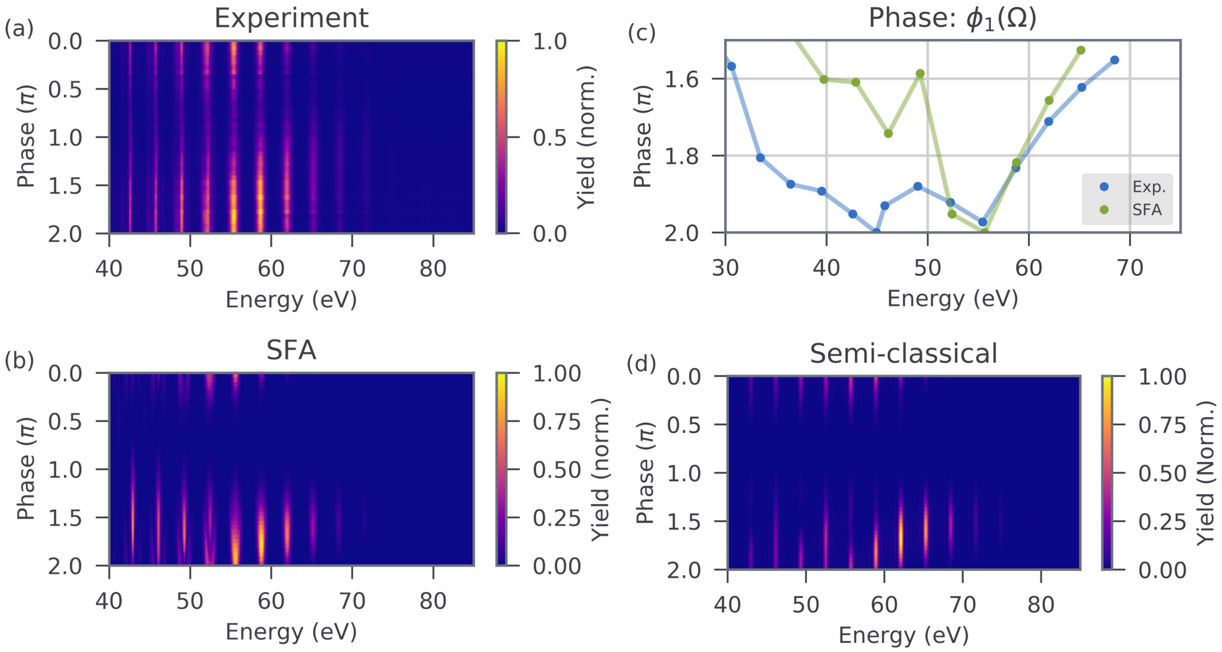

Figure 3.8: Phase-dependent HHG spectra in symmetry-preserving ω-3ω driving fields. (a) Experimentally obtained spectra. (b) Macroscopic SFA calculations for $R = 0.23$ and $I = 3 \times 10^{14}\,\mathrm{W\,cm^{-2}}$. (c) Comparison of $\phi_1(\Omega)$ between experiment and macroscopic SFA calculations. (d) Semi-classical calculations including harmonic emission from two subsequent half-cycles coherently added over three complete laser cycles. Unlike in Figure 3.6, the HHG yields in (a) and (b) are plotted on a linear scale as they produce better visibility of phase-dependent features. The figure is reproduced from [114].

3.3.2 Harmonic suppression in symmetry-preserving fields (ω-3ω)

To further investigate the role of interference from two subsequent half-cycles, the experiment and calculations were repeated for half-cycle symmetry-preserving (ω-3ω) driving fields for similar intensity and R values. The resulting spectra, shown in Figure 3.8(a), exhibit far fewer features as compared to the symmetry broken ω-2ω case. The macroscopic SFA calculations shown in Figure 3.8(b) reveal a similar pattern. The reduced contrast between Figure 3.8(a) and (b) can be attributed to larger interferometer-related noise given the smaller wavelength of 3ω. As discussed earlier, the fitting procedure is also deployed here to judge the degree of correlation between experiment and theory (see Figure 3.8(c)). The phase coefficients ($\phi_1(\Omega)$) are well reproduced beyond 50 eV. In contrast to ω-2ω fields, here, the recolliding electron trajectories and their respective ionization rates vary identically with ϕ in the subsequent half-cycles. It leads to a strong suppression of HHG over large values of ϕ (in between π and $\pi/2$ as seen in Figure 3.8(a), (b) and (d)). In the case of other values of ϕ, the identical contributions constructively add up to having a higher ionization rate without any visible individual harmonic suppression. The semi-classical calculation in Figure 3.8(d), however, shows strong periodic modulation and harmonic suppression between 40 eV and 60 eV around $\phi = 1.5\pi$, which are absent in the experimental and SFA spectra. This modulation resembles intra-cycle, long-short trajectory interference as shown later quantitatively. The intra-cycle interference features observed for ω-2ω fields in Figure 3.7(a) and (b)) are also absent in the respective experimental and SFA spectra in Figure 3.6 for ω-2ω fields. This can be attributed to stronger dephasing of long-trajectories as compared to the short ones when averaged over varying intensities in the focal volume [129, 7]. The absence of additional intricate interference features in the semi-classical spectra from symmetric fields in Figure 3.8(d), as compared to the ones observed at $\phi = 0.4\pi, 1.4\pi$ from asymmetric fields, further hints at inter-half-cycle interference at play.

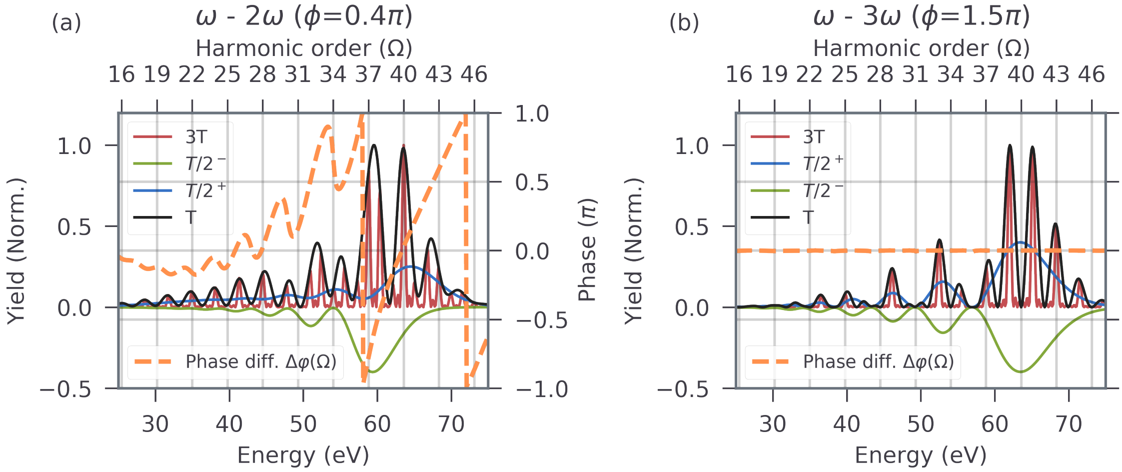

Figure 3.9: Semi-classical analysis of subsequent half-cycle contributions to spectral modulation in two-colour HHG. The spectra and spectral phase differences are obtained for (a) asymmetric half-cycles (ω-2ω), where $\phi = 0.4\pi$ and (b) symmetric half-cycles (ω-3ω), where $\phi = 1.5\pi$. The calculations here use the same intensity and R values as in Figure 3.7 and 3.8. The spectra shown here arise from the coherent addition of all recombining electron trajectories within the positive half-cycle ($T/2^{+}$), negative half-cycle ($T/2^{-}$), one cycle (T), and three cycles ($3T$) where T represents a cycle of the fundamental field (ω). $3T$ and T are normalized to their own respective maxima, while the other two are normalized to $T/2^{-}$ (and scaled by a factor 0.5) to maintain their relative yield. The spectral phase difference ($\Delta\varphi(\Omega)$) is calculated between $T/2^{-}$ and $T/2^{+}$. A negative yield is used to decouple the emission directions. The figure is reproduced from [114].

3.3.3 Semi-classical interpretation of harmonic suppression

Apart from the realistic harmonic spectra shown in figures 3.7 and 3.8(d), the semi-classical calculations provide deeper insight into the source of harmonic peak suppression. The modulations in harmonic spectra are investigated by selectively choosing the spectrum generated by each half-cycle followed by their coherent addition. In Figure 3.9(a), the different half-cycle spectra from an ω-2ω combination are shown for $\phi = 0.4\pi$. This ϕ corresponds to the spectrum where strong harmonic peak suppression is observed in the experiment and macroscopic SFA calculations (see Figure 3.5(b)). The subsequent half-cycles of the resulting ω-2ω waveform exhibit similar electron recombination rates, as evident from the height of the curves labeled $T/2^+$ and $T/2^-$, where T corresponds to one laser cycle of the IR (ω). The modulations in the curves arise from long-short trajectory interference within each respective half-cycle. A difference in periodicity is observed in $T/2^+$ as compared to $T/2^-$ arising from different electric field shapes (see Figure 3.7), which result in altered energy and phase of the recombining electron trajectories in the subsequent half-cycles (see Figure 3.9(a)). The spectrum T is obtained from a coherent sum of $T/2^+$ and $T/2^-$ (with a significant spectral phase difference), the subsequent half-cycles, resulting in strong spectral modulation and suppression of odd and even order harmonics. Finally, the realistic photon-energy spaced harmonic spectrum $3T$ is produced by the coherent addition of spectrum T over three laser cycles. Looking back at spectrum T again, this curve defines an envelope governing the suppression of harmonic order in spectrum $3T$. This appears from the spectral phase difference ($\Delta\varphi(\Omega)$) of $T/2^+$ and $T/2^-$ (also shown in Figure 3.9(a)), which leads to a suppression of odd harmonics when $\Delta\varphi(\Omega) = 0$ and suppression of even harmonics when $\Delta\varphi(\Omega) = \pi$. These conditions can also be derived from the frequency comb expression of the spectra in question. The envelope or low-frequency modulation of spectrum T arises from the amplitude modulations in $T/2^+$ and $T/2^-$. This highlights the role of intra-half-cycle and inter-half-cycle interference as the source of strong individual harmonic suppression. However, as discussed earlier, the experiments and realistic SFA calculations, involving intensity averaging over the laser focal volume suppress long-trajectory contributions [129, 7]. This reduces the contribution of intra-half-cycle interference. Thus, inter-half-cycle interference is considered responsible for the prominent peak suppression and seemingly aperiodic modulation near $\phi = 0.4\pi, 1.4\pi$ for an ω-2ω driver. The spectra for all values of ϕ (see Figure 3.7) are in good qualitative agreement with experimental observations. Given the simplicity of our semi-classical calculations, a quantitative agreement with the experiment is not expected. This is primarily due to a large deviation in the proportion of long and short trajectories within each half-cycle.

Similarly, Figure 3.9(b) illustrates the semi-classically calculated half-cycle spectra, driven by ω-3ω at $\phi = 1.5$. This particular value of ϕ has been chosen as it corresponds to the appearance of strong modulation in the harmonic spectrum as observed in Figure 3.8(d). Given the symmetry of subsequent half-cycles, the spectra $T/2^+$ and $T/2^-$ have exactly identical yield and intra-cycle interference patterns arising from long and short trajectory contributions. The coherent addition of $T/2^+$ and $T/2^-$ results in spectrum T, which exhibits an envelope with the same periodicity as observed from each half-cycle.

Given the identical energy and constant spectral phase difference ($\Delta\varphi(\Omega) = \pi$) of recombining electron trajectories in the two half-cycles, their coherent addition only leads to suppression of even harmonics, unlike in ω-2ω fields. The realistic sharp harmonic peaks are produced by the coherent addition of three full cycles and are represented by $3T$ (in red). The low-frequency modulation of T arises from the modulating amplitudes of $T/2^+$ and $T/2^-$. Thus, intra-half-cycle interference is responsible for the modulation observed in Figure 3.8(d) at $\phi = 1.5\pi$. As a consequence, the absence of this modulation in the intensity (in the focal volume) averaged experiment and realistic SFA spectra are expected as discussed earlier. The disappearance of the intra-half-cycle modulation is also observed in Figure 3.8(d), where ϕ is close to 0 or 2π. This occurs due to a strong suppression of short, and enhancement of long trajectories by the window of ionization rate (ADK) in time, which shifts to earlier electron birth times. Thus, a symmetric two-color field (as shown here for ω-3ω fields) is unable to support the nontrivial interference pattern obtained in a symmetry-broken field (as shown for ω-2ω fields).

3.4 Summary and outlook

In conclusion, the suppression of individual harmonics of both orders (odd and even) in the HHG spectra generated by two-colour symmetry-broken (ω-2ω) laser fields (in neon) was observed, and precise control over this peak-suppression contrast through a phase-delay (ϕ) between the driving colors was demonstrated. The complete phase (ϕ) dependent behaviour was well reproduced using macroscopic SFA calculations including propagation effects, and an intuitive semi-classical analysis of emission bursts from each half-cycle. The investigations revealed a nontrivial interference pattern to be responsible for the peak suppression at certain energies, which arise from strong spectral phase mismatch between bursts from subsequent half-cycles for symmetry-broken laser fields (ω-2ω). The symmetry requirement was further verified using symmetry-preserving (ω-3ω) fields where the interference pattern leading to harmonic peak suppression was absent.

This study highlights the role of symmetry, and inter-half-cycle interference in two-colour HHG, where the ratio of their central wavelengths turns out to be an important parameter in addition to intensity, R, and ϕ. Other schemes using non-commensurate combinations in this regime would be an interesting extension of this study. Additionally, a stronger value of R leads to the coalescence of more than two trajectories within a single half-cycle [132] and their subsequent interference with neighboring half-cycles is another interesting exploration direction. Given its contribution to the harmonic phase, a change in the parent atom could also lead to a largely modified interference envelope as already seen in theoretical predictions [42].

The demonstrated additional control parameter of half-cycle asymmetry will eventually be useful in optimizing waveforms to generate a desired spectral modulation as has been performed for optimizing yield and cutoff energies [73, 25, 77]. It is expected to greatly benefit applications demanding further tunability of HHG, like in molecular spectroscopy or measurement of atomic transition lines with XUV frequency combs [43, 125].

Chapter 4

Soft-X-ray pulses from polarization-gated mid-infrared laser fields

4.1 Introduction

High-harmonic generation (HHG) is a process that inherently converts high-intensity, infrared, or mid-infrared laser pulses into light with higher photon energies [30, 87]. Further, the spectral bandwidth of the generated high-harmonic pulses is often large enough to support ultra-short pulses with temporal durations down to a few attoseconds at their Fourier limit. The shortest attosecond pulses currently achieved in the laboratory were clocked at 43 as in the XUV (Extreme Ultraviolet) spectral region and 53 as in the soft-X-ray spectral region [44, 94]. However, their time-bandwidth product indicates a far lower achievable pulse duration, reaching down to $\approx$ 20 as [94], which is around the atomic unit of time of 24 as. The quest to experimentally obtain even shorter pulses remains an ongoing challenge and an interplay between optimal driving fields, retrieval techniques, and dispersion compensation of the attosecond pulses.

In this chapter, the temporal properties of isolated soft-X-ray attosecond pulses generated by polarization-gated MIR laser pulses are numerically explored. These pulses are often used due to their relaxed requirement of the driving pulse duration for the generation of isolated XUV and X-ray pulses [93, 94]. The code used in these simulations has already been successfully used to model HHG in the XUV to soft-X-ray regime [67, 138, 114]. While the exact macroscopic propagation conditions are challenging to reproduce, a qualitative theoretical estimation of the atto-chirp and temporal profile of the soft-X-ray pulses is insightful and hence is included in the simulations. This chapter aims to bridge the gap between previous numerical studies that have explored this topic either at the single-atom level [22] or with macroscopic propagation using linearly polarized single-cycle pulses [86]. Here, the focus is on simulating HHG by polarization-gated MIR laser fields as they co-propagate in the macroscopic generation medium. Further, the advancement of tabletop long-wavelength laser sources is gradually pushing the spectrum of isolated attosecond pulses toward higher photon energies along with larger bandwidths. As a consequence, traditional pulse retrieval techniques like FROG-CRAB have become error-prone [105] and have led to the development of new pulse retreival algorithms [24, 126]. Thus, theoretical HHG estimations based on realistic propagation scenarios provide additional insights into the attainable temporal structure of these isolated attosecond pulses.

4.2 Numerical modelling

4.2.1 Driving pulse

Amplitude gated HHG

To achieve such short isolated pulses in time, the laser-field interaction must be modified such that only one laser-field cycle contributes to the emission of the harmonics, unlike multi-cycle emission which leads to a harmonic comb in the spectra and bursts of short pulses in time (as explored in chapter 3). Traditionally, such isolation or gating has been achieved by making the driving MIR/IR pulses short in time, such that only one laser cycle is strong enough to produce the highly energetic harmonic emission, aptly referred to as amplitude gating [65], and have also been applied to gating harmonics in the soft-X-ray regime [71, 32, 149, 72]. A drawback of this method is that it is often challenging to routinely produce ultrashort few-cycle (near single-cycle) MIR/IR laser pulses with high contrast between the central and satellite laser cycles. Additionally, this usually leads to isolated attosecond pulses only for the most energetic part of the harmonic spectrum while the lower energy components still exhibit beating in the spectrum due to interference from neighboring attosecond bursts [87]. A carefully chosen metallic filter is necessary in such a scenario to block the lower energy components where multiple bursts are expected, thereby shrinking the total bandwidth of the HHG spectrum.

Polarization gated HHG

The other established method for isolating attosecond pulses is through polarization-gating and is also the technique focused upon in this chapter. Here, the harmonic emission from neighboring laser cycles is blocked by suppressing the electron re-scattering (as described in the three-step-model) by the use of elliptically polarized laser fields. The Coulomb force incident on the electron displaces it in the XY plane (perpendicular to propagation) in a way that makes the electron-recollision-trajectory miss the parent ion [29, 19]. Such a laser field is realized by splitting the driving laser pulse into two equal parts and making them circularly polarized but with opposing helicities. After which, interferometrically combining them with a time delay in between them leads to a pulse that is circularly polarized except in the center of the combined pulses, where the laser field strengths are highest as graphically illustrated in Figure 4.1. The field structure of a polarization-gated (PG) pulse is realized using the following formalism where two circularly polarized

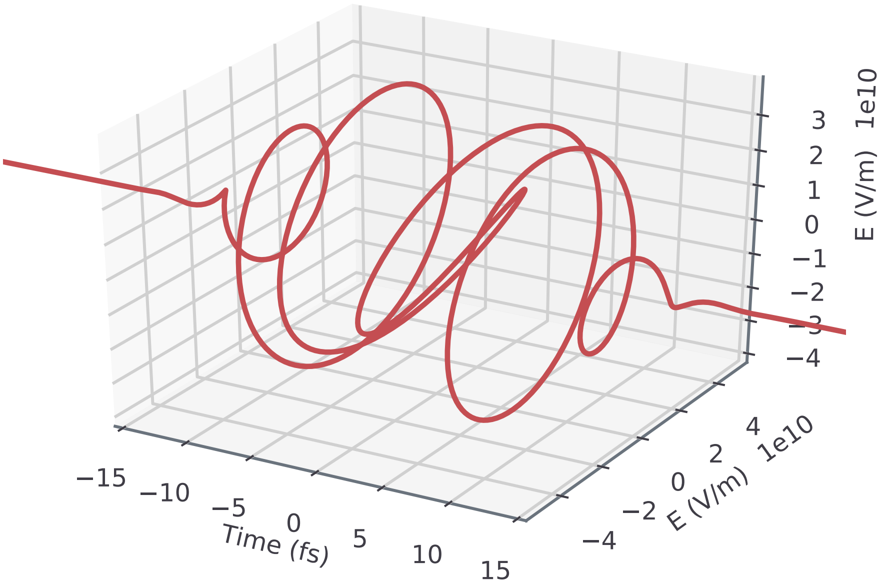

Figure 4.1: Polarization gated laser E-field structure (in the XY polarization and time axes) used in the numerical simulation.

components are

$$\begin{bmatrix} E_{x1}(t_1) \\ E_{y1}(t_1) \end{bmatrix} = \begin{bmatrix} \sqrt{\frac{2I}{c\epsilon_0}} e^{-2\ln(2)\left(\frac{t_1}{\tau}\right)^2} e^{i2\pi\frac{c}{\lambda}t_1} \\ E_{x1}(t_1)e^{i\frac{\pi}{2}} \end{bmatrix} \tag{4.1}$$

and

$$\begin{bmatrix} E_{x2}(t_2) \\ E_{y2}(t_2) \end{bmatrix} = \begin{bmatrix} \sqrt{\frac{2I}{c\epsilon_0}} e^{-2\ln(2)\left(\frac{t_2}{\tau}\right)^2} e^{i2\pi\frac{c}{\lambda}t_2} \\ E_{x2}(t_2)e^{i-\frac{\pi}{2}} \end{bmatrix}, \tag{4.2}$$

where I is the peak intensity, c is the vacuum speed of light, ϵ_0 is the dielectric constant, τ is the pulse duration (FWHM) of the Gaussian envelope, λ is the central wavelength and $t_1 = t - \Delta/2$ ($t_2 = t + \Delta/2$) are the separate time axes where $\Delta = t_2 - t_1$ is the time delay between the two pulses. The combined PG pulse can then be expressed as

$$\begin{bmatrix} E_x(t) \\ E_y(t) \end{bmatrix} = \mathrm{Re} \begin{bmatrix} (E_{x1}(t_1) + E_{x2}(t_2)) \cdot e^{i\Phi_{cep}} \\ (E_{y1}(t_1) + E_{y2}(t_2)) \cdot e^{i\Phi_{cep}} \end{bmatrix} \tag{4.3}$$

where an additional phase term Φ_{cep} is added to account for the modification of HHG spectra due to a changing carrier-envelope-phase (CEP), as the pulses used in this numerical study are short enough to see strong CEP-dependent effects.

The pulse used in the simulation is shown in Figure 4.1, which is based on realistic parameters that have been experimentally realized. The parameters closely follow experiments performed by Jie Li and coworkers, who used PG MIR pulses to produce soft-X-ray harmonics along with their CEP dependence [93]. The carrier wavelength is fixed at 1.7 µm with a pulse duration of 12 fs (Gaussian envelope) and a delay of 11.3 fs between the two circularly polarized pulses to produce the desired HHG gate width. The gate width (δ) is expressed as [19]

$$\delta = \frac{\epsilon_t}{\ln(2)} \frac{\tau^2}{\Delta} \tag{4.4}$$

where $\epsilon_t = 0.1$ is an ellipticity threshold of the laser pulse, where 90 % of the harmonic yield drops[1]. The value of ϵ_t is taken from the literature where the authors estimate the HHG yield drop using a numerical semi-classical model [93]. The other parameters in equation 4.4 follow the convention as already defined earlier and δ turns out to be 1.8 fs. The value of δ being less than the laser half-cycle (2.8 fs), ensures a single burst of HHG [19, 20, 93]. In this configuration, the PG pulse (shown in Figure 4.1) varies strongly with the CEP, and hence for most of the discussions in this chapter, a static CEP of 0.27π is chosen, corresponding to the HHG spectrum with the highest cutoff energies.

4.2.2 High-harmonic generation medium

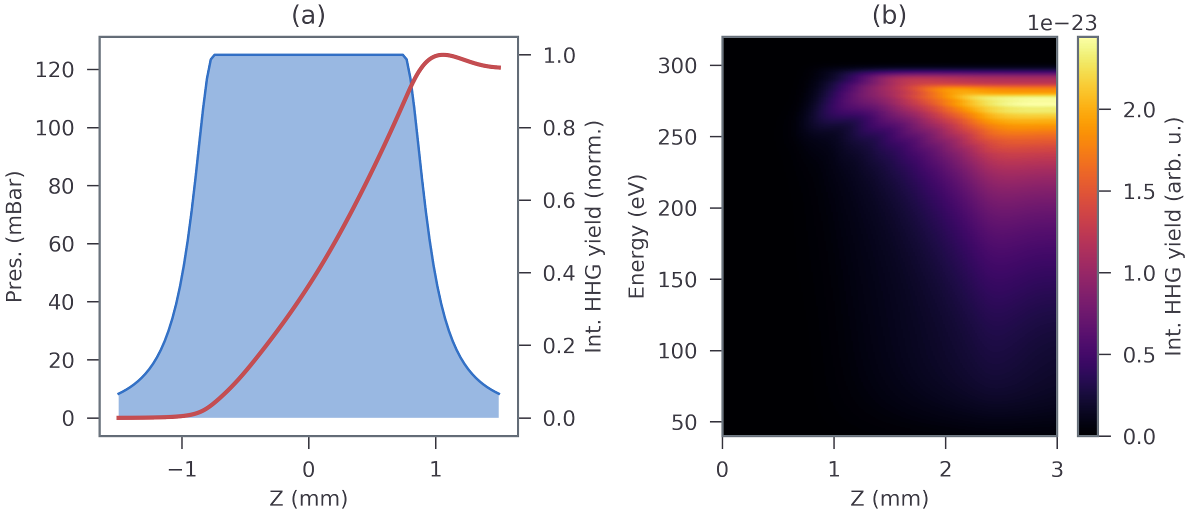

Figure 4.2: Phase matching of high harmonics in a neon gas cell with polarization gated MIR driving pulses. a) The Lorentzian gas pressure profile (shaded in blue) used in the simulation along with the HH yield (red curve) as a function of the propagation distance z, integrated along the frequency and radial axes. b) HH yield integrated along the radial axis as a function of frequency and propagation length in the gas medium.

Hypothetically in an experiment, the polarization-gated driving laser pulses are focused into a gas medium, similar to the arrangement described in chapter 3. Likewise, here too, this is theoretically modeled by first defining a Gaussian focal profile with a beam waist $w_0 = 85\,\mu\text{m}$. Further, a Neon gas-filled target cell is defined as the generating medium

---

[1] In comparison with the linearly polarized case.

with a thickness of 1.5 mm and a hole size twice that of the Gaussian beam waist. The 3D space is modeled in 2D given the cylindrical symmetry of such a target, as described in section 3.2.4. Originally, the gas medium was modeled using a rectangular gas-density profile through the target, as designed by the author of the propagation code, Maximilian Högner [67]. Later, including in this chapter, the calculations were updated with a more realistic, Lorentzian function to account for the gradual decrease in pressure due to gas flowing out of the cell into the vacuum chamber surrounding it. This modification was implemented by Johannes Schötz and coworkers, who obtained quantitative agreement between experiments and the numerical model in cases where the harmonics were driven with even higher intensities, leading to very high degrees of ionization (over $30-40\,\%$) of the ground state in the target [138]. Here too, given the higher degree of ionization in polarization-gated pulses as compared to amplitude-gated driving pulses, the Lorentzian gas distribution is retained for more accurate numerical modeling.

Figure 4.2 (a) illustrates the phase matching and build-up of the harmonics, integrated over space and frequency as it propagates through the neon target experiencing the pressure gradient of the target. The Gaussian focus of the driving laser is placed 2 mm before the target (measured from the center of the target). The observed smooth buildup of harmonics along z justifies the macroscopic parameters chosen in the calculation. Additionally, Figure 4.2 (b) illustrates the same HHG buildup along z for each frequency or photon energy, highlighting a stronger phase-matching in the soft-X-ray region, close to the spectral cutoff ($\approx 300\,\mathrm{eV}$). The gas pressure was scanned in the simulation and finally set at 125 mbar, which produced optimal phase-matching conditions in the target. Higher pressures resulted in a substantial modification of the MIR driving field and significantly affected the harmonic buildup in the target. Experimentally, similar configurations have used target gas pressures in the range of 700 mbar − 1 bar and this discrepancy can possibly be attributed to overestimation in measuring the pressure right at the target, which in practise can be lower due to strong effusion of the gas into the vacuum chamber [93, 94].

Compared to amplitude-gated HHG, an important difference in polarization-gated HHG is the additional ionization, and thereby plasma generation before and after the HHG 'gate'. This occurs as the polarization-gated driving pulses are significantly longer as compared to their amplitude-gated counterpart with the same effective gate width. Looking at the numerical results, this is evident in Figure 4.3 where the ionization fraction is observed to significantly increase around the 'gate'. The underlying reason for this is the E-field vector, which, despite being elliptically polarized around the 'gate', does not suppress ionization as highlighted by the dotted red curve in Figure 4.3 and has not been accounted for in previous numerical studies in the literature [86].

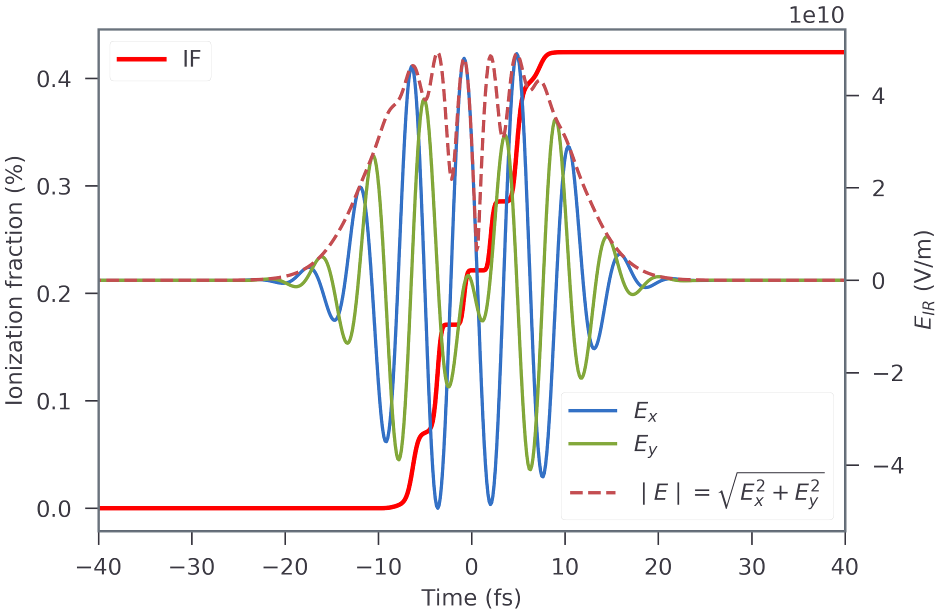

Figure 4.3: Ionization fraction at the beginning of the gas target as a function of the time axis of the polarization-gated driving laser field. The E-field in the X and Y polarization directions exhibits the ellipticity within the pulse which disappears close to the central ‘gate’ due to a vanishing Y component. Additionally, an ellipticity-independent absolute magnitude of the E-field is also included to understand the origin of strong ionization around the ‘gate’.

4.3 Results and discussion

4.3.1 Soft-X-ray attosecond pulse

Using the same simulations as described in section 3.2.4, but with the above-mentioned modification to the driving laser field and generating medium, the effective macroscopic dipole response in the near-field was propagated over 2 m in vacuum. After this propagation step, only the central part[2] of the beam was used to select the low-divergence short trajectory induced HHG [134]. Additionally, including a larger portion of the spatial profile led to strong distortion of the termporal profile of the harmonics, and hence was avoided. Figure 4.4 (a) illustrates a part of the HH beam profile in the far field. Given the limitations of the code in terms of computation time the HHG cutoff photon-energy was set at 300 eV. The set intensity of the driving laser pulse was adjusted accordingly.

---

[2] The transmission diameter is 8.4 mm which roughly corresponds to where the signal drops to 40 % of the central maxima

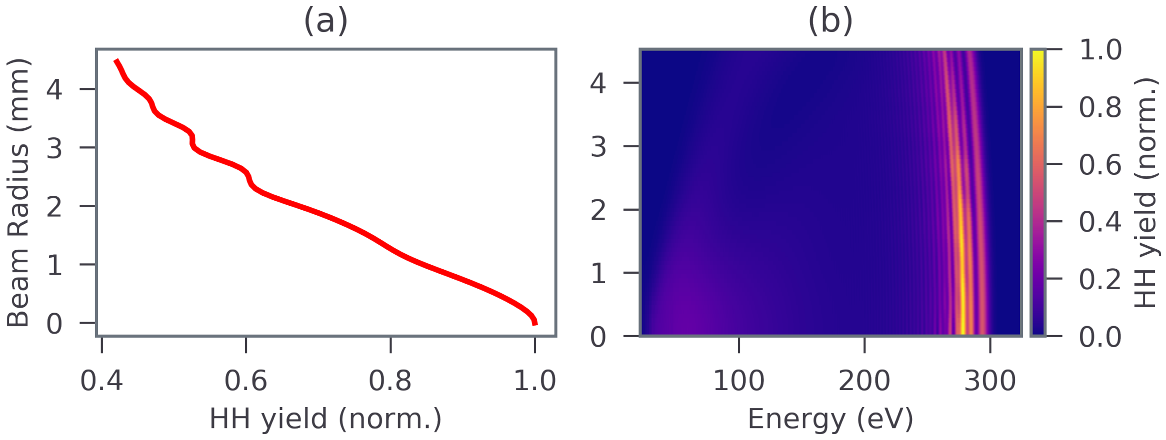

Figure 4.4: Radial profile of polarization gated HHG. (a) Spectrally integrated HHG yield distribution over the radial direction in the far-field after propagation of 2 m. (b) Spectrally resolved radial profile showing gradual spectral-cutoff energy and yield reduction on moving away from the central axis.

Spectral profile

The resulting spectrum is shown in Figure 4.5 (b) along with its spectral phase highlighting a strong second-order positive chirp. In the experiments [93], a thin metallic filter is usually used to block the driving laser field, and here too, a 100 nm thick tin (Sn) filter transmission profile is used for a more accurate estimation of the pulse duration. Hence the spectral distribution below 80 eV is also omitted in the figure as it is fully blocked by the filter [63]. It should be noted that the linearly polarized section (gate) of the polarization-gated laser field (as illustrated in Figure 4.1) can rotate in the plane of polarization, leading to the polarization of harmonic emission to experience the same rotation as well, depending on the delay between the two counter-rotating laser pulses. Thus, only the harmonic emission along the polarization axis of the 'gate' of the driving laser pulse is considered for further analysis. Finally, the obtained spectral density after applying the above-mentioned considerations is highest around 280 eV while the cutoff energy extends beyond the 300 eV mark, well within the soft-X-ray region.

Temporal profile

A Fourier transform of the spectrum including the phase and coupled with a Hilbert transform produces the temporal profile (envelope) of the soft-X-ray pulse as shown by the green curve in Figure 4.5 (a). The curve has been time shifted to around 0 fs for easier representation and comparison[3]. As expected, the temporal structure appears heavily chirped and extends over 500 as, while its transform limit (with a flat/constant spectral-phase)

---

[3] Here,0 fs corresponds to the center of the driving laser pulse

produces a pulse as short as 31 as (FWHM) and is represented by the red curve in the same figure.

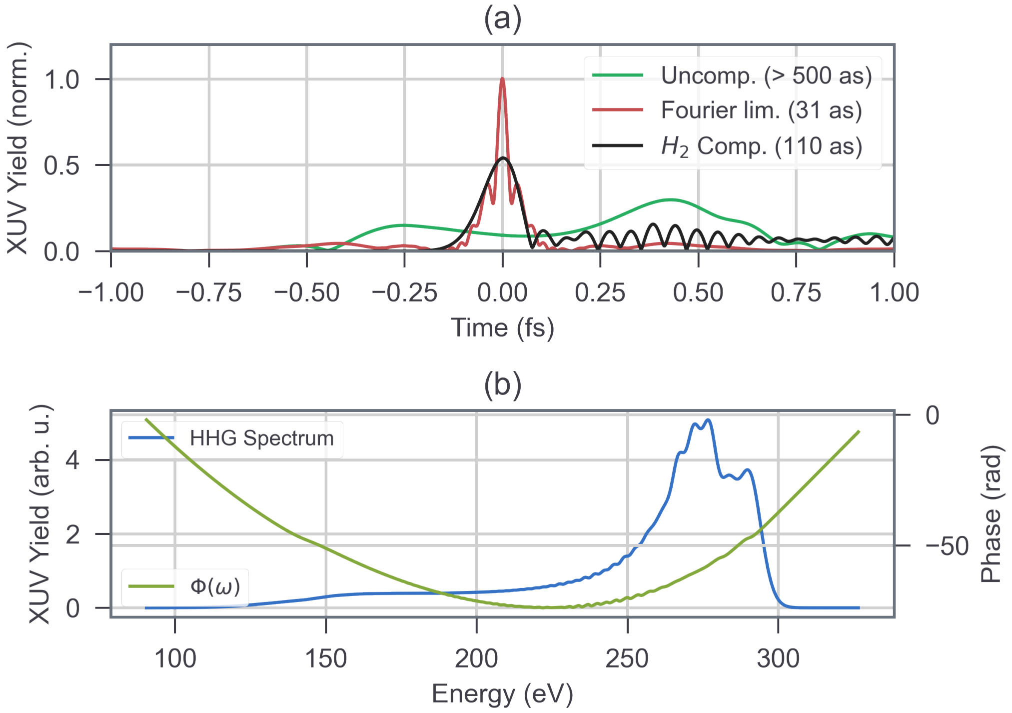

Figure 4.5: Simulated temporal and spectral profile of the soft-X-ray attosecond pulses generated by a polarization gated MIR laser pulses in the far-field, after macroscopic propagation through a Neon gas cell. (a) A comparison of the temporal structure of the harmonic radiation at its Fourier limit, in its original form and when compressed using H_2 plasma column. (b) The far-field radially integrated numerically obtained dipole spectrum, which is also used to produce the temporal profile of the pulse in (a).

4.3.2 CEP dependence

Given the short pulse duration of the driving pulse, even for polarization-gated driving fields, there is a dependence of the HHG spectrum on the CEP which has been demonstrated experimentally for similar parameters as used here [93]. In the experiments, the CEP dependence is often used as an indicator of isolated attosecond pulse generation where the spectrum exhibits a strong contrast between a CEP with a strong laser half-cycle as compared to multiple weaker half-cycles at other CEPs. In the simulations, the CEP dependence has been used to optimize the gas pressure of the generation medium. Higher than optimal gas pressures led to a strong reshaping of the driving laser field and has been discussed in a previous work [86]. In the scenario presented here, high gas pressures lead to laser field reshaping, with its magnitude strongly correlated to the CEP. This results in reduced contrast in the CEP-dependent HHG modulation over the whole spectrum. To prevent field-reshaping, the numerically set gas pressure was gradually reduced until the CEP dependence showed a strong contrast over the whole spectrum (see Figure 4.6), and in qualitative agreement with experimental observations [93].

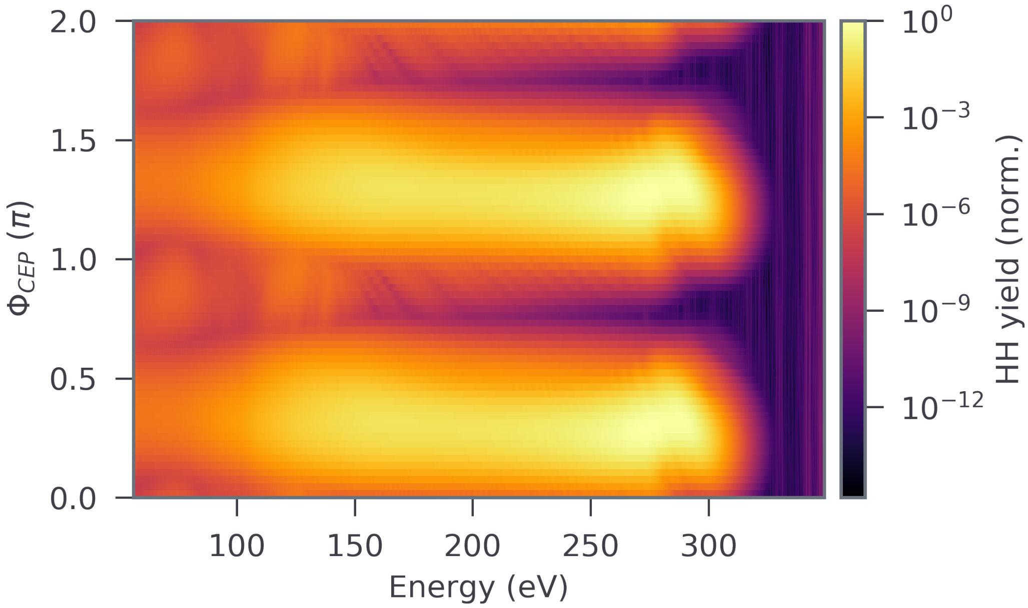

Figure 4.6: CEP dependence of polarization gated HHG in the far-field after macroscopic propagation and radial integration. The spectral distribution also includes the transmission function of a 100 nm thick Sn filter. Unlike other figures, a log scale has been used to represent the HHG yield to highlight the sharp drop for certain CEPs, signifying isolated soft-X-ray pulse generation.

The CEP dependence of the harmonics also provides a clearer picture of the harmonic cutoff energy. The approximate CEP (0.27π) for the spectrum with the highest cutoff energy is thus determined and used in all the other analyses presented in this chapter.

4.3.3 Atto-chirp

In addition to obtaining the optimal yield in the desired energy region by optimizing the phase-matching parameters, one also needs to optimize the temporal duration of the attosecond pulse. In scenarios where soft-X-ray harmonics are generated using long wavelength drivers, the attosecond bursts are positively chirped due to stronger phase-matching of the short-trajectories and are commonly referred to as atto-chirp [79, 22]. The simulations performed here also illustrate this positive chirp and are shown in Figure 4.5 (b) in terms of the spectral phase along with the spectrum obtained in the far-field after propagation. The origin of chirp in these calculations can be better identified using time-frequency analysis where the different energy components of the harmonic emission can be mapped to when it was emitted on the time axis. The time-frequency map is generated by integrating the harmonic emission over space (radial axis) in the far-field and performing a Short Time Fourier Transform (STFT) with a Hann window [52]. The results are shown in Figure 4.7 where a characteristic harmonic emission curve is observable within a cycle of the driving laser. The strength of the color map indicates the relative yield in the time-frequency axis and indicates that the short trajectories (indicated by the rising curve and positive chirp) are better phase-matched as compared to the long-trajectories (usually present on the falling edge with a negative chirp, after the frequency cutoff). As assumed for the spectrum and temporal profile calculation, the integration over the radial axis here in the far-field also assumes an iris[4] only letting through the central part of the harmonic beam.

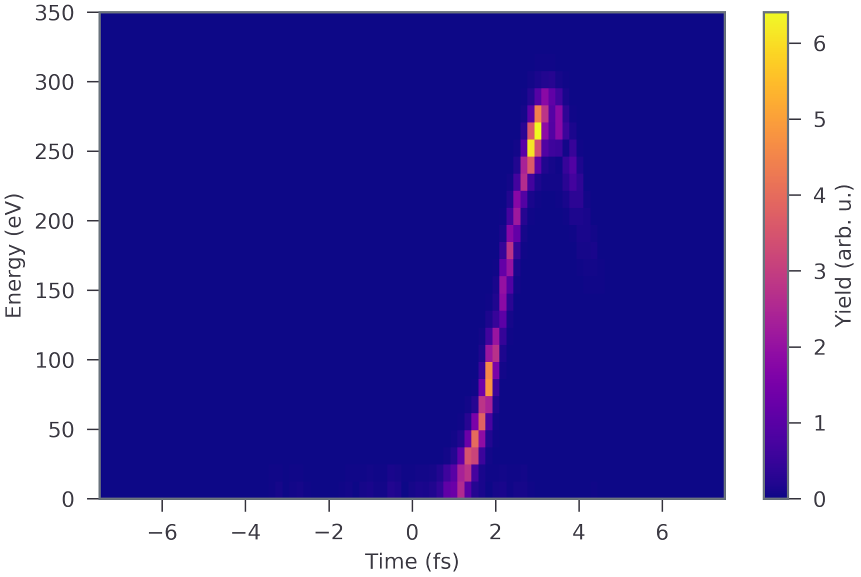

Figure 4.7: Time-frequency representation of PG harmonics obtained in the far-field integrated over the radial components. The time axis corresponds to that of the PG MIR laser pulse centered around 0 fs.

The wavelength and intensity dependence of atto-chirp (group delay dispersion) can be derived from a semi-classical three-step model and the approximate estimate near the center of the spectrum is expressed as [21, 22]

$$GDD_{\text{atto}} = 1.63 \times 10^{18} \frac{1}{I_0 \lambda_0} \tag{4.5}$$

where I_0 and λ_0 are the peak intensity (in W/cm^2) and carrier wavelength (in μm) of the driving pulse respectively. Although this relationship highlights that the atto-chirp

---

[4] The diameter is 8.4 mm, corresponding to where the integrated HHG yield falls to 40 % of the maxima.

decreases with an increase in wavelength and intensity [36], and hence smaller for MIR wavelengths[5] in comparison to the more commonly available NIR (≈ 800 nm) wavelength, the chirp becomes significantly less compressible for photon energies close to 300 eV and above.

Experiments with a spectral density weighted towards lower photon energies (peaking around 150 eV) have been able to use a 400 nm thick tin (Sn) filter to compress the atto-chirp to obtain pulses as short as 53 as [94], characterized using the photo-electron streaking technique [75]. The usability of Sn as a compression material has been found to be limited to below 200 eV [83, 94], and thus has not been effective in these simulation results given the spectral range. The compression has been independently tested here for thicknesses up to 1 µm where the transmission is additionally very low. The compressibility of HHG filters was tested using the following formalism [151]

$$E_{\mathrm{out}}(\omega) = E_{\mathrm{in}}(\omega) \cdot H(\omega) e^{-i\Phi(\omega)} \tag{4.6}$$

where $E_{\mathrm{in}}(\omega)$ is the numerically simulated spectrum, $H(\omega)$ is the amplitude transmission function of the filter and $\Phi(\omega)$ is the applied spectral phase which is defined as

$$\Phi(\omega) = \frac{\omega}{c_0} n(\omega) d \tag{4.7}$$

where d is the thickness of the material and $n(\omega)$ is the frequency dependent refractive index. The transmission function and the refractive index for X-rays propagating through solids can be readily derived from the atomic scattering factor databases [64, 63].

In the literature, other works have theoretically proposed that a long column of hydrogen plasma can effectively compress atto-chirp in the range of 300 eV to 1000 eV while still maintaining a relatively high transmission [22]. Following this proposal, the new frequency-dependent refractive index can be expressed as [22]

$$n_{\mathrm{H_2}}(\omega) = \sqrt{1 - \frac{\omega_{\mathrm{p}}^2}{\omega^2}} \tag{4.8}$$

where ω_{p} is the plasma frequency and is expressed as

$$\omega_{\mathrm{p}} = \sqrt{\frac{e^2 N_{\mathrm{e}}}{\epsilon_0 m_{\mathrm{e}}}} \tag{4.9}$$

where m_{e} and e are the mass and charge of an electron, ϵ_0 is the vacuum permittivity, and N_{e} is the electron density in the plasma, which is approximated to a value of $5 \times 10^{19}\,\mathrm{cm}^{-3}$ for fully ionized H_2 gas at standard room temperature and pressure [22]. Using equations 4.6 and 4.7 with equation 4.8, the possibility to compress the spectrum obtained is explored by varying the thickness of the plasma medium d. The shortest temporal profile was obtained with a plasma length of 90 cm, which is close to the value obtained for macroscopic

---

[5] These wavelengths are a necessary prerequisite to produce significant yields of soft-X-ray or water-window harmonics

simulations with linearly polarized amplitude gated pulses in the literature [86]. The length can also be shortened if the gas pressure inside is increased as the product of the pressure and length determines the dispersion compensation in the medium [22]. Finally, a compressed pulse duration of 110 as (FWHM) is obtained and is represented by the black curve in Figure 4.5 (a). As evident, this is still significantly larger than the Fourier limit due to higher-order chirp as inferred from the asymmetry of the temporal profile. A similar distortion was also observed in the experimentally demonstrated compression using a Sn filter [94].

4.4 Summary and outlook

In conclusion, full 3D numerical simulations based on the SFA including macroscopic propagation were performed in both orthogonal polarization axes enabling realistic modeling of soft-X-ray HHG from a polarization-gated pulse. Such simulations have not yet been explored in the literature to the best of the author's knowledge. Additionally, the laser and HHG medium parameters are closely based on already performed experiments [93]. Comparable simulations in the literature have either used single-atom SFA calculations with polarization-gated pulses which ignore propagation effects [19, 20], or have explored macroscopic propagation effects with linearly polarized and amplitude-gated pulses [86]. The primary goal here in this thesis was to explore the temporal properties of the soft-X-ray attosecond pulses and how far they could be compressed after a realistic propagation through the generating medium and far-field propagation. Such theoretical estimation in the soft-X-ray regime is interesting for the community given the shortcomings of current experimental retrieval techniques of the temporal profile, where they span over a large bandwidth in the soft-X-ray region [105, 24, 126].

According to the results obtained from the simulations, the attosecond pulses could be compressed by a 90 cm long channel of H_2 plasma, as proposed earlier in the literature [22]. Although this may look challenging experimentally at a first glance, H_2 plasma capillaries have been demonstrated in the past [14, 49]. Despite this, as also observed in the single atom calculations [22], the pulse obtained is not fully compressible close to its Fourier limit due to the residual higher-order chirp remains an open problem for further investigation with alternate compression mechanisms.

Chapter 5

Valleytronics in strong tailored laser fields

5.1 Introduction

Strong infrared light fields tend to impart additional control parameters over light-matter interaction where highly non-linear processes such as electron tunnel ionization at attosecond timescales, their subsequent ponderomotive acceleration, and eventual re-scattering, have been heavily explored in systems such as atoms [114], molecules [74], liquids [101], nanotips [139], nanoparticles [172], and bulk semiconductors [47]. In parallel, right from the first isolation of an atomically thin layer of graphene in 2004, the research carried out on such hexagonal 2D materials has been experiencing exponential growth [122, 121, 170]. More recently, inversion symmetry broken 2D materials such as transition metal dichalcogenides (TMDCs) or hexagonal boron nitride (hBN) with two different alternating atoms instead of a uniform carbon chain is in the spotlight [107, 146]. As described earlier in subsection 2.3.3, these materials break inversion symmetry and open up gaps at the Dirac points otherwise observed in the bandstructure of graphene forming two unique valleys (see Figure 2.9). The valleys are degenerate in energy but remain unique in another quantum state, the valley pseudospin. This leads to a new degree of electronic freedom (analogous to electronics and spintronics) and hence defines a new field aptly referred to as 'valleytronics'. Currently, the exploration of valleytronics and 2D materials is primarily restricted to experiments relying on resonant or multi-photon excitation of electrons using circularly polarized light [23], while their detection is based on photo-luminescence of helical polarized light or deflection of induced electric current [108, 137].

This chapter of the thesis is dedicated to experiments that explore the overlap of valleytronics with strong tailored mid-infrared light fields. Among the existing works in this direction, only Langer and coworkers have demonstrated the switching of valley excitation from one valley to the other using linearly polarized terahertz light fields preceded by a resonant circularly polarized pump and interpreting the valley occupation through the polarization-resolved high harmonic spectra of the terahertz pulse [88]. In contrast, the work in this thesis closely follows the prescription theoretically proposed by Jiménez-Galán and coworkers, where selective valley excitation is achieved using light far below resonance by tailoring the polarization of the E-field of light in the shape of a trefoil (pump) and controlling its orientation (rotation) [76]. Further, the valley excitation is read out using a second linearly polarized laser pulse (probe) and observing the helicity (proportional to the valley selective excitation) imprinted in its harmonics (intra-band). Not only does this demonstrate a completely new mechanism of valley selection enabled by valley selective band-structure modification, but this method also allows the choice of material to be decoupled from the pump wavelength. The theory and experiment both use hBN as a model system given its large band-gap ($\approx 5.9\,\mathrm{eV}$) with respect to the available laser source and its robustness in handling and carrying out laser irradiation experiments in ambient conditions.

This chapter is organized in the following manner. First, the specially developed three-arm interferometer is described which generates the rotatable trefoil pump pulse followed by a time-delayed linearly polarized probe pulse. The microscope developed to focus all the laser pulses down to a single mono-crystalline patch of hBN is described next followed by a description of the novel technique developed to detect very small signals in the presence of large amounts of background signal from various sources. Next, a description of the laser source is presented before moving on to highlighting how the hBN monolayers are fabricated and characterized during the experiments. Finally, the most important results are presented and discussed in detail with a comparison to numerical calculations with experimentally relevant parameters.

5.2 Experimental background

Experimentally investigating light-matter interaction in 2D crystals using ultrashort laser pulses comes with its own set of challenges. Namely, the interaction region is limited to a single crystal grain with a well-defined orientation. Presently, in the case of mono-layer hBN, this is on the order of $10\,\mu\mathrm{m}$ [82]. On the other hand, tightly focused short laser pulses result in intensities very close to the damage threshold of these 2D mono-layers at weak average powers', leading to a significant drop in signal-to-noise ratio (SNR). This section highlights relevant technical details which have proven to be necessary for performing the far-off resonance valleytronics control and probing experiment.

5.2.1 Interferometer

A large part of this experiment constitutes a three-arm Mach–Zehnder interferometer, as shown in Figure 5.1. In the following subsections, various aspects of the interferometer are described in detail.

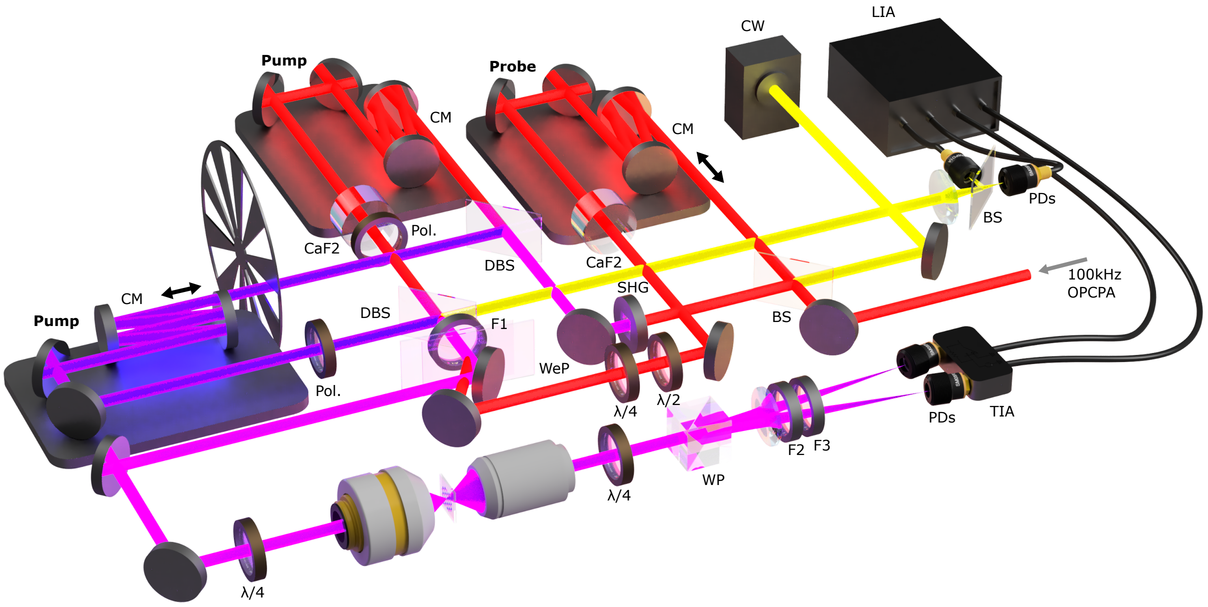

Figure 5.1: Setup for the valleytronic control and probing experiment. The acronyms have the following meaning: WP - Wollaston prism, F1 - Long pass filter (Thorlabs FELH0850), F2 - Short pass filter (Thorlabs FESH0750), F3 - Long pass filter (Thorlabs FELH0600), PD - Photodiode, TIA - trans-impedance amplifier, BS - Beam splitter, DBS - Dispersion controlled beam splitter, Pol. - Polarizer, WeP - Wedged pair, CM - Chirped mirrors, SHG - Second harmonic generation crystal ($LiNbO_3$), CW - Continuous wave laser, LIA - Lock-in amplifier. A detailed description of the setup is provided in the text.

Probe arm

The 2 µm (wavelength) laser pulses from the laser source are directly fed into the interferometer, which consists of three arms. First, the pulses are split in two by a 50-50 beamsplitter (Thorlabs) marked as BS (red beams) in Figure 5.1, where one proceeds to the pump- and the other to the probe arm. At the probe arm, the pulses go through a variable neutral density filter followed by a delay stage, which, along with a pair of silver retro-reflecting mirrors, hosts two customized chirped mirrors for positive dispersion and spectral filtering at the same time. Spectral filtering is crucial given the existence of weak optical signals at lower wavelengths arising from the parametric processes in various crystals in the laser system. The delay stage is mounted on a closed-loop stick-slip piezo rail (Smaract SLC-24 series) with a positioning resolution of 1 nm. Further down, the pulses go through a defined thickness of material (CaF_2) to compensate for excess positive dispersion. Additionally, another long-pass spectral filter (Thorlabs FELH1500) is placed in the beam path to further suppress the unwanted optical signals at lower wavelengths. Finally, the probe pulses go through a half- and quarter-waveplate (B.Halle Nachfl. GmbH), after which, they recombine with the other arms. The use of this waveplate combination is non-standard and a novel implementation in this setup. They are used for controlling the polarization state of the probe pulses and the mechanism is described in greater detail later in subsection 5.2.2.

Pump arms

The reflected component of the beamsplitter BS (red beams) is sent through a 1.5 mm thick Lithium Niobate ($LiNbO_3$) crystal (United Crystals Inc.) cut at 45.6°. This interaction produces a second pulse at half the wavelength of the fundamental by sum frequency generation [10]. Lithium Niobate is well suited for this in our experiment with a 2 µm fundamental wavelength, given its wide transparency range in the mid-infrared, up to 3.5 µm. The phase matching conditions (Type 1) lead to the second harmonic component being cross-polarized with respect to the fundamental pulse [10]. The co-propagating two-color pulses (ω and 2ω) are separated using a custom-designed dichroic splitter (BS2032) and marked in Figure 5.1 as DBS. The ω arm passes through a variable neutral density filter, a retro-reflection stage, and CaF_2 as used in the probe arm, but without the piezo motion rails as this arm's length is kept fixed with respect to the other arms. Additionally, a wire grid polarizer (Thorlabs) is placed in its path to clean its polarization state, before it combines with the 2ω arm at another dichroic splitter (BS2032). The 2ω arm is reflected off the beamsplitter at 90 degree and it traverses the exact same arrangement as the ω arm. The only difference is, a different pair of custom chirped mirrors for 2ω on the delay stage above a stick-slip piezo nano-positioning rail (Smaract SLC-24 series), different amount of dispersion compensating material and a perpendicular axis set on the polarizer. The pump arm (co-propagating ω and 2ω) is further sent through a long-pass spectral filter (Thorlabs FELH0850) to block the parametric optical signals generated at the harmonics of the two-color pump in the $LiNbO_3$ crystal. Finally, the two-color pump ($\omega - 2\omega$) and probe pulses pass through the fused silica wedged pair to recombine with the probe pulses (ω) which are reflected off it. This wedge pair arrangement not only acts as a beam recombination element but also as a power attenuator for the probe pulses as only 4 % of the power is reflected.

Trefoil pump rotation

When the bi-circular ω and 2ω arms of the pump are combined in the interferometer such that the E-field ratio at the focus is 2:1, the coherent sum of their E-field in the XY plane (plane perpendicular to propagation) is transformed to that of a trefoil. The effective field of the pump can be expressed as

$$\begin{bmatrix} E_x(t) \\ E_y(t) \end{bmatrix} = \Re \begin{bmatrix} E_\omega(t) + E_{2\omega}(t) \\ E_\omega(t) e^{-i\frac{\pi}{2}} + E_{2\omega}(t) e^{i\frac{\pi}{2}} \end{bmatrix} \tag{5.1}$$

where the exponent with $-\frac{\pi}{2}$ and $\frac{\pi}{2}$ represent the action of the cross-polarized linear components through a $\lambda/4$ plate. The linear field components can be expressed as

$$E_\omega(t) = \Re(E_0 e^{-2\log(2)\frac{t}{\tau}^2} e^{i\omega t} e^{i\varphi}) \tag{5.2}$$

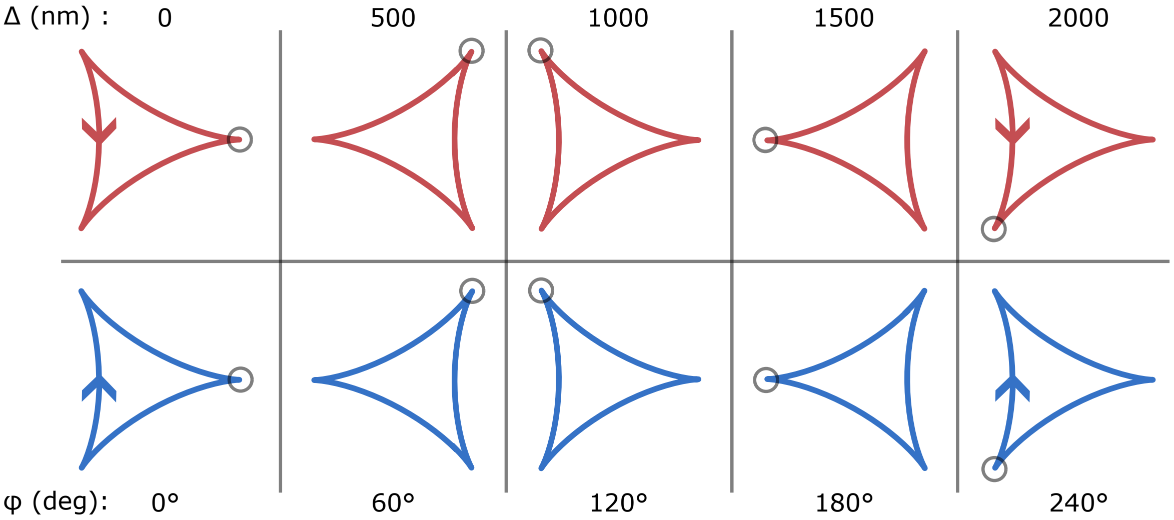

Figure 5.2: Calculated angular rotation of the trefoil generated by the pump arms. The respective delay (in nm) between the two pump arms is mentioned above while the angle they induce is labeled below. A grey round marker tracks the rotation by pointing to the same trefoil corner. Additionally, this calculation has been done for both the helicity configurations of the pump arms, represented in a different color. A central wavelength of $\lambda_0 = 2000\,\text{nm}$ is assumed for the calculation.

$$E_{2\omega}(t) = \Re(\frac{E_0}{2} e^{-2\log(2)\frac{t}{\tau}^2} e^{i2\omega t}) \tag{5.3}$$

where $\varphi = \frac{\Delta}{\lambda_0} 2\pi$, λ_0 being the central wavelength of the fundamental pump arm and Δ is the displacement between the ω and 2ω arms induced by the piezo delay stage. The Δ parameter is experimentally controlled to rotate the trefoil structure. When the central wavelength (λ_0) of the ω arm is 2000 nm, a rotation of 360° is induced by delaying the piezo stage by 3000 nm as illustrated in Figure 5.2. This information is used to convert the stage delay to angular rotation recorded with the experimental data. Additionally, the helicity of the trefoil is also a parameter that can be controlled in the experiment. This is achieved by rotating a $\lambda/4$ waveplate by 90°. In the current experiment, this corresponds to the $\lambda/4$ plate shown right before the reflective objective in Figure 5.1. Theoretically, this can be calculated by reversing the sign of the phase retardation in the 'Y' component of equation 5.1, which then reads as

$$\begin{bmatrix} E_x(t) \\ E_y(t) \end{bmatrix} = \begin{bmatrix} E_\omega(t) + E_{2\omega}(t) \\ E_\omega(t) e^{i\frac{\pi}{2}} + E_{2\omega}(t) e^{-i\frac{\pi}{2}} \end{bmatrix}. \tag{5.4}$$

This calculation is illustrated in Figure 5.2 and it is important to note that the flip in helicity does not change the angular orientation of the trefoil and is required to explain certain features discussed later with the experimental results.

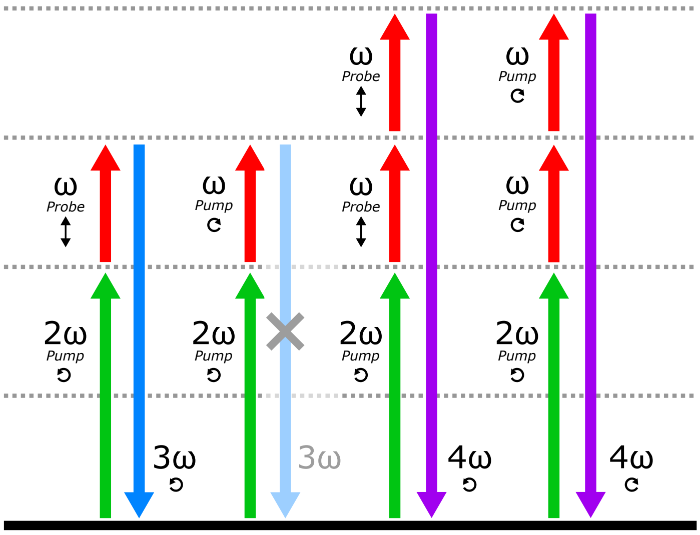

Figure 5.3: Energy level diagram of the parametric processes which are used to temporally and spatially overlap the three pump (ω, 2ω) and probe (ω) pulses in the interferometer.

Spatio-temporal overlap

As described earlier, the implementation of a three-arm interferometer leads to the laser pulses traveling through three different non-collinear optical paths. Upon recombination, they require careful alignment such that they are spatially and temporally overlapped in the interaction region. To ensure this, the second-order and third-order non-linearity in fused silica is utilized where a two- and three-photon transition of ω and 2ω leads to the production of 3ω and 4ω photons, respectively. To utilize this effect, the 2ω pump is chosen as a common reference and the other pulses are aligned onto this particular arm. An initial spatial alignment of all three arms using irises is enough to ensure a coarse spatial overlap between the pulses at the focus on the fused silica substrate. Soon after, the 2ω pump arm is delayed w.r.t. the ω pump arm while observing the 4ω with an appropriate band-pass filter before the photodiodes. The pump arms being bi-circular (counter-rotating) in their polarization state w.r.t. each other leads to the 3ω channel being disallowed. After the 2ω pump delay is fixed, its delay w.r.t. the probe arm is determined by scanning the probe delay stage and observing the 3ω or 4ω channels as both these transitions are allowed. This can be explained by considering that linearly polarized can be decomposed into equal parts of bi-circular components and the helicity matching with 2ω leads to the non-linear parametric response. An overview of this is presented graphically in the form of an energy level diagram in Figure 5.3. After the temporal alignment, the spatial overlap is checked and optimized based on the respective parametric signals.

Probe polarization control

As shown in Figure 5.1 and described later in sub-section 5.2.2, a $\lambda/4$ placed is the last optical element before the pulses enter the reflective objective. This leads to a major problem where the third arm or the linearly polarized probe as in this experiment cannot remain linear once passing through the $\lambda/4$ plate unless it is along the optical axis at 45°. Also, a linear polarization launched at 45° w.r.t. ‘s’ or ‘p’ polarization states loses its linear contrast as it becomes elliptic on acquiring a different phase-shift in the ‘s’ and ‘p’ components on every reflective optic in its beam path. To have full flexibility over the polarization state of the probe pulses after the $\lambda/4$ plate, a novel scheme was implemented where a combination of a $\lambda/2$ and $\lambda/4$ wave plates were placed additionally in the probe arm as also depicted in Figure 5.1. Intuitively, one can think of these additional plates as inducing perfectly opposing elliptical polarization which cancels out in the final $\lambda/4$ before the reflective objective to produce linearly polarized light with a high extinction ratio. This scheme was also numerically tested using a Jones matrix approach. It was observed that any arbitrary shifts in phase between the ‘s’ and ‘p’ components in the beam path in between the two $\lambda/4$ waveplates can be compensated. However, changes in magnitude between the ‘s’ and ‘p’ components lead to a deviation from linearity and cannot be compensated by this scheme.

A movable silver mirror at 45° is placed right before the reflective objective to intercept the probe pulses to optimize and characterize the polarization extinction ratio or linearity. They are then guided to an InGAs photodiode with a polarizer attached to it at a fixed angle. The fixed angle is kept such that the probe polarization is aligned along ‘s’ or ‘p’ to prevent any additional ellipticity induced by the intercepting mirror, which would not be present otherwise during the experiment.

Interferometric stability

During the experiment, it is critical that the angle of the three-leaf or trefoil pump remains stable as this is directly linked to the delay between the two colors in the pump arm. To characterize the delay stability, an additional temperature-stabilized continuous wave (CW) diode laser (Thorlabs L785P090 with LDMT9) was sent through the two pump arms to interferometrically measure its path difference over time. The interference experienced by such a monochromatic coherent light detected on a photodiode can be expressed in terms of amplitude modulation (D_1) as:

$$D_1(\Delta\varphi) = I_1 + I_2 + 2\sqrt{I_1 I_2}\sin(\Delta\varphi) \tag{5.5}$$

where I_1 and I_2 are the light amplitudes of the two interferometer arms and $\Delta\varphi$ is the phase difference between the two, induced by a delay stage or other undesired drift in optomechanical elements. However, just with a single diode detection, it is only possible to uniquely determine the absolute path-length difference within the interval of $-\pi/2$ and $\pi/2$. Larger drifts are no longer unique as they can imply a change in either direction.

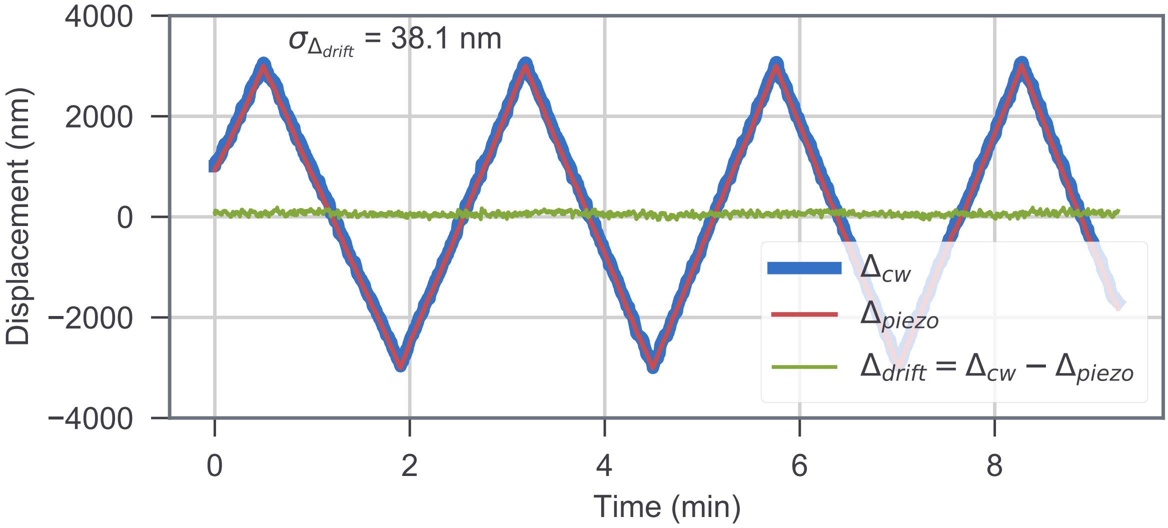

Figure 5.4: Interferometric stability of the pump arms. The relative displacement between the $\omega - 2\omega$ pump arms is recorded while a piezo closed-loop stage controlling the displacement is sweeped over a period of ten minutes. The position read out by the stage is compared to that extracted from the CW interferometer to estimate the error in displacement mapping.

This problem is solved by detecting the interference on a second diode with a $\pi/2$ phase shift. The modulation can then be expressed as:

$$D_2(\Delta\varphi) = I_1 + I_2 + 2\sqrt{I_1 I_2}\cos(\Delta\varphi). \tag{5.6}$$

The ratio D_1/D_2 between the two components is proportional to $\tan(\Delta\varphi)$. Ignoring the constant coefficients, the total phase difference can be extracted from $\Delta\varphi = \arctan(D_1/D_2)$, where the ambiguity of direction does not exist and the absolute path difference (Δ_{cw}) is given by:

$$\Delta_{cw} = \frac{\lambda_{cw}\Phi}{2\pi} \tag{5.7}$$

where Φ is the unwrapped form of $\Delta\varphi$, and λ_{cw} is the wavelength of the CW laser used (785 nm). Experimentally, the $\pi/2$ phase shift is implemented by introducing a small angle between the two arms, in such a way that it leads to fringes in space, all of which modulate with $\Delta\varphi$, but with a phase offset proportional to the spatial fringes. Using a beam-splitter these fringes are split onto two photodiodes (Thorlabs DET025A/M) and aligned such that one photodiode (D_1) detects a fringe that exhibits a phase delay of $\pi/2$ w.r.t. the fringe detected by the other photodiode (D_2).

Using the above-mentioned scheme, the interferometric stability was found to be highest around two hours after switching on the driving laser system. Additionally, tests were carried out to measure the stability when the laser was going through the interferometer and the piezo delay-stage being scanned, as is during the valleytronic control experiment, as illustrated in Figure 5.4. Over a period of ten minutes, the standard deviation of the position generated by the closed-loop piezo stages from the position extracted from the CW interferometer is found to be close to 38.1 nm, which roughly translates to about 4.6° in rotation error of the $\omega - 2\omega$ bi-circular trefoil structure.

However, during a valleytronic control experiment, two polarizers are placed in the two interferometer arms in a cross-polarized configuration as described in the earlier subsection. This enabled photons to be uniquely identified from each arm, leading to a disappearance of the interference pattern. To circumvent this, the CW laser is sent in at a polarization angle of 45° and at the exit, the partial components from each arm recombine orthogonally polarized to each other. A quarter-wave plate is subsequently used to transform the cross-polarized light into bi-circular, followed by a polarizer which revives the interference pattern. Due to a significant drop in the effective power of the CW beams passing through the interferometer, only one photodiode is used during the experiment, which restricts the detection to a limited range of displacement tracking.

5.2.2 Microscope

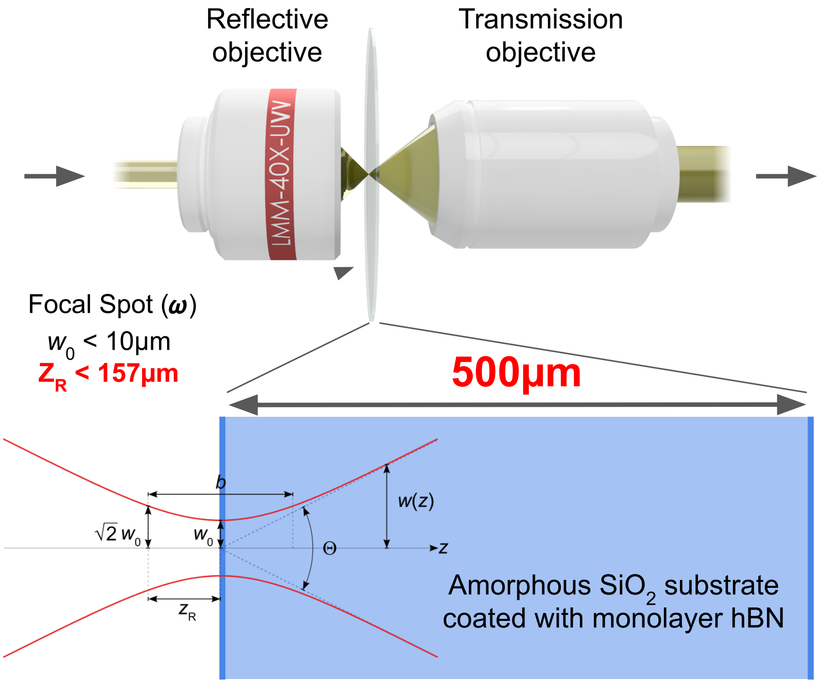

Figure 5.5: A schematic representation of the microscope arrangement used to expose tailored laser pulse on isolated hBN monolayer grains, and detect their harmonics for the valleytronic-control experiment.

After the three-arm interferometer, the laser pulses are magnified using a reflective telescope arrangement to roughly match the input diameter of the tight-focusing objective, and adjust the beam divergence. However, right before the focusing objective, a broadband quarter-wave plate (B.Halle Nachfl. GmbH) is placed with the optical axis at 45° with respect to the cross-polarized axis of the two-color pump. This wave plate arrangement transforms the linear cross-polarized pump pulses into circularly polarized counter-rotating pulses that look like a trefoil or a three-leaf pulse in the XY plane, as required in the experiment. This technique is well established and has been used in numerous experiments in labs around the world [62, 110, 135]. The quarter waveplate is intentionally placed right before the focusing element to prevent any changes in ellipticity due to a phase shift between the 's' and 'p' polarization components upon reflection, especially from beam folding mirrors and other coated optical elements. The core segment of the microscope involves tight focusing of laser pulses from all three interferometer arms, followed by a collection and collimation configuration before the light proceeds to the detection apparatus. In-between, a 500 µm thick fused silica substrate is placed to host the hBN monolayers on the front surface, as illustrated in Figure 5.5.

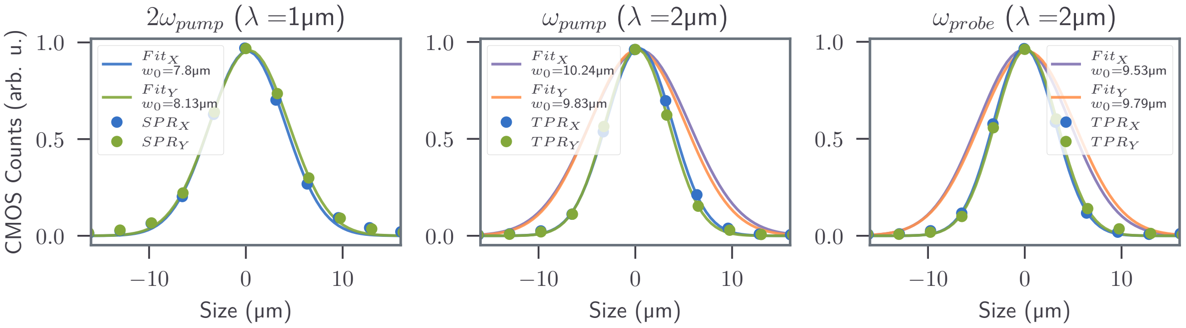

Figure 5.6: Beam profile cross-section of three interferometer arms at the focal plane of the objective on a CMOS detector. The wavelength of 2ω arm results in a single-photon response (SPR), whereas the other two arms produce a two-photon response (TPR) on the detector given the band gap of silicon.

The focusing was achieved without adding any dispersion or chromatic aberration, by using a reflective objective (Thorlabs LMM25X-P01) with a numerical aperture (NA) of 0.4. The beam profile in the interaction region is characterized by placing a CMOS sensor (DataRay WinCAM) in the focal plane and the cross-section of the resulting 2D signal on the sensor is shown in Figure 5.6, for all three interferometer arms. Since the focal spot sizes are comparable to the pixel size (3.2 µm), a fit function is used to extract the beam waist (w_0). The fit function can be expressed as follows:

$$I(r) = A \exp\left(\frac{-2r^2}{w_0^2}\right) + B$$

where w_0 is the beam waist, r is the radial position and A and B are constants to scale the amplitude and a DC offset due to sensor noise. The w_0 extracted from the fit are 8 µm, 10.04 µm, and 9.66 µm for the 2ω pump, ω pump, and ω probe arms, respectively. The beam is largely circular at focus and the residual ellipticity is found to be below 5 % for all the arms, as determined from the ratio of $w_{0\mathrm{x}}/w_{0\mathrm{y}}$. The ω arms only produce a two-photon response on the CMOS detector due to its lower photon energy (≈ 0.6 eV) compared to the band gap of silicon (≈ 1.12 eV). Hence, the w_0 is extracted from a fit which is $\propto \sqrt{I(r)}$. These w_0 spot sizes not only allow spatially restricting the laser interaction to a single hBN mono-crystalline grain, but also a Rayleigh length (201 µm for 2ω and 157 µm for ω) which is significantly smaller than the thickness of the fused silica substrate below hBN. This allows individually optimizing the substrate position (back or front/hBN coated surfaces) in the focus, by observing the surface-enhanced perturbative harmonics.

After the fused silica substrate is in the focus, the diverging beam along with other nonlinear signals is re-collimated using a long-working-distance transmissive objective (Olympus LUCPLFLN20X) with an NA of 0.45. A closely matched NA allows the complete divergent beams to be collected. Further down, the laser pulses are polarization resolved using a quartz Wollaston prism (B.Halle Nachfl. GmbH). The prism introduces an angular separation of 10° between the 'p' and 's' polarization components, which are then loosely focused by a CaF_2 lens (f=40 cm) onto the two separate large area photodiodes (Thorlabs SM05PD1B). A $\lambda/4$ waveplate is placed between the transmission objective and Wollaston prism with its optical axis at 45° with respect to the prism to convert the photodiodes into helicity detectors.

5.2.3 Lock-in polarization detection

In this experiment, the signal of interest is the 3ω harmonic as described in the theoretical background. However, there are multiple sources of light co-propagating along with the signal and impinging on the diodes as illustrated in Figure 5.2.3. Hence, a simple amplified detection of the diode current is not enough to distinguish the relevant 3ω ($\lambda \approx 667$ nm) signal. Signals which are spectrally different are already filtered using high- or low-pass spectral filters (Thorlabs FELH0600, FESH0750) which block the fundamental 2ω, components above $\lambda = 750$ nm and other components below $\lambda = 600$ nm. However, the ω component is more of a problem, as no commercial filter could be found allowing a high transmission in the 3ω region while fully suppressing ω. Additionally, 3ω is also produced by the pump (ω) and probe (ω) by a three-photon process on the silica substrate, thereby further polluting the experimental signal.

This major problem is overcome by a novel technique in which, the 2ω arm of the interferometer is modulated using a mechanical chopper wheel (Thorlabs MC2000B) with a 50 % duty-cycle at a known frequency. This forces the pump to oscillate between a purely circular ω or a bi-circular $\omega - 2\omega$ configuration. Hence, the 3ω signal of interest, which is probed by a modulated bi-circular pump is also modulated at the chopping frequency, while the 3ω remaining in the background due to the ω arms are not. This modulated signal along with the background impinging on the photodiodes is amplified by two low-

ω	2ω	3ω	4ω	5ω
Pump$_\omega$	SHG Pump$_\omega$ (χ^2)	THG† Pump$_\omega$ (χ^3)	Pump$_\omega$ (χ^4)	Pump$_\omega$ (χ^5)
Probe$_\omega$	SHG Probe$_\omega$ (χ^2)	THG† Probe$_\omega$ (χ^3)	Probe$_\omega$ (χ^4)	Probe$_\omega$ (χ^5)
	Pump$_{2\omega}$	**Valley-Hall** $\omega, \omega, 2\omega$	SFG Probe$_\omega$ Pump$_{\omega,\,2\omega}$ (χ^3)	SFG Pump $\omega, \omega, \omega, 2\omega$ (χ^4)
	Leak	SFG‡ Pump $\omega, 2\omega$ (χ^2)	Leak	SFG Pump (χ^4) Probe$_{\omega,\,\omega,\,\omega,\,2\omega}$
		SFG* Probe$_\omega$ Pump$_{2\omega}$ (χ^2)		SFG Pump $\omega, 2\omega, 2\omega$ (χ^3)
		Leak†		SFG Probe $\omega, 2\omega, 2\omega$ (χ^3)
		FWM** (χ^3) $2\omega, 2\omega, -\omega$		

Table 5.1: List of signals picked up by the photo-detector, sorted by their respective wavelength and non-linear processes involved in giving rise to it. Here, ω refers to $\lambda = 2\,\mu\text{m}$. The signals at frequencies other than 3ω are all rejected by high extinction ratio spectral filters. Other components are marked with a corresponding blocking method and they are as follows: † Rejected by lock-in amplifier ‡ Rejected based on selection rules of bi-circularly polarized light. * Rejected based on helicity filtering of light. ** Rejected based on modulation with trefoil pump rotation. Only the signal arising from the valley hall effect is let through.

noise trans-impedance amplifiers (Femto DLPCA-200) attached right behind the respective photodiodes, to minimize noise picked up by long cables. The amplified voltage signals are then fed into two time-synchronized lock-in amplifiers (Zurich Instruments MFLI).

To better understand how the signal is extracted, it's worthwhile to go over a brief overview of the basic principles behind lock-in detection. The time-dependent voltage signal being read by the lock-in device can be expressed as

$$V(t) = A_s(t)\sin(2\pi f_s t + \phi) + A_{n1}\sin(2\pi f_{n1} t) + A_{n2}\sin(2\pi f_{n2} t) + A_{n3}\sin(2\pi f_{n3} t) ... \quad (5.8)$$

where f_s and ϕ are the frequency and phase, respectively, corresponding to the chopping or modulation frequency, f_{ni} are the different noise frequency components including a DC background where $f_{DC} = 0$ and A_i are their respective amplitudes. The noise frequencies also have a phase term in reality, but they have been omitted here for simplicity due to their irrelevance in the signal extraction process. In the first step, $V(t)$ is mixed with a signal from a local oscillator $\sin(2\pi f_{lo})$ using a mixer circuit [68], which can be conceptually expressed as

$$M_X(t) = V(t) \cdot \sin(2\pi f_{\mathrm{lo}} t) \tag{5.9}$$

where M is the mixed signal output. Further, using the trigonometric identity

$$\sin(A)\sin(B) = \frac{\cos(A-B) - \cos(A+B)}{2} \tag{5.10}$$

equation 5.9 can be expanded as

$$\frac{A_s(t)A_{\mathrm{lo}}(\cos(2\pi t(f_s - f_{\mathrm{lo}}) + \phi) - \cos(2\pi t(f_s + f_{\mathrm{lo}}) + \phi))}{2} + \\ \frac{A_{n1}(t)A_{\mathrm{lo}}(\cos(2\pi t(f_{n1} - f_{\mathrm{lo}}) + \phi) - \cos(2\pi t(f_{n1} + f_{\mathrm{lo}}) + \phi))}{2} + ... \tag{5.11}$$

A similar term is present for each of the noise frequencies in equation 5.8. Lock-in amplifiers including the one used here are usually set to have $f_{\mathrm{lo}} = f_{\mathrm{s}}$, which is achieved by synchronizing the internal clock or local oscillator to the signal modulation frequency and is given by the optical chopper used in the experiment. This leads to the creation of a DC component in the mixed signal at $f_{\mathrm{lo}} - f_{\mathrm{s}} = 0$ and $f_{\mathrm{lo}} + f_{\mathrm{s}} = 2f_{\mathrm{lo}}$. Hence, $A_{\mathrm{s}}(t)$ can be extracted from the DC component by using a low-pass filter, with a cutoff frequency (f_{c}) which removes the high-frequency oscillation leaving the DC component behind. The cutoff frequency is determined by the time constant τ as $\tau \propto \frac{1}{f_{\mathrm{c}}}$. The time constant is chosen such that $0 < f_{\mathrm{c}} < (f_{\mathrm{lo}} + f_{\mathrm{s}})$. The longer the time constant is, the smaller f_{c} is, rejecting the highest amount of noise frequencies. As the time constant is shortened, the demodulation picks up more and more noise as expressed in equation 5.11.

Even after the low-pass filtering of equation 5.11, a $\cos(\phi)$ term still remains where ϕ is more specifically the phase difference between the modulation signal and internal clock signal which can always be quite different depending on the experimental setup. This could lead to situations where they are completely out of phase, leading to a minimal demodulated signal. To overcome this problem, the raw signal is mixed a second time with a replica of the internal local oscillator but with a phase difference of $\pi/2$ and can be expressed as

$$M_Y(t) = V(t) \cdot \sin(2\pi f_{\mathrm{lo}} t + \pi/2). \tag{5.12}$$

Now the phase (ϕ) independent lock-in filtered signal can be obtained as

$$R = \sqrt{M_X^2 + M_Y^2} \tag{5.13}$$

while the phase in itself is extracted by[1]

$$\phi = \mathrm{atan2}(M_Y, M_X). \tag{5.14}$$

---

[1] atan2 is used instead to atan to obtain a mapping on the full quadrant between [$-\pi$,π] instead of [$-\pi/2$,$\pi/2$].

All the measurements in this chapter are based on the phase independent R signal.

5.2.4 Laser source

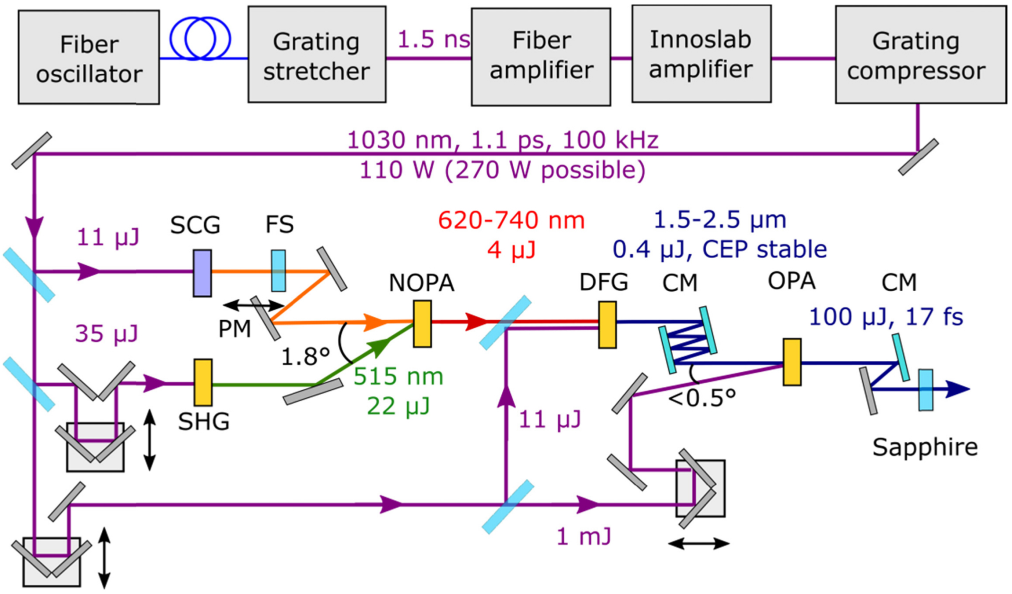

Figure 5.7: A schematic representation of the 100 kHz mid-IR laser source. The figure has been reused from its original publication by M. Neuhaus et al. [119].

The laser pulses used for the experiments described in this chapter originate from a mid-IR laser system based on the Optical Parametric Chirped Pulsed Amplification (OPCPA) design, which was developed within the group [119]. The system is seeded with a fiber oscillator (Active Fiber Systems) which produces pulses at a wavelength of 1 µm, which are temporally stretched and directed into a fiber pre-amplifier (Active Fiber Systems). In the final amplification stage, the pulses are sent through an InnoSlab amplifier after which they are temporally compressed before entering the OPCPA. The amplified laser pulses are split into three arms. One is used to create white light by supercontinuum generation, the second for sum harmonic generation (SHG) and the third is carried forward as a pump for the next stage. A non-collinear optical parametric amplification (NOPA) stage is tuned such that it produces pulses centered around 680 nm from the white light and SHG of the pump. This output, along with the third part of the 1 µm pump undergoes difference frequency generation (DFG) to produce pulses centered around 2 µm. Finally, the weak 2 µm pulses produced by DFG are amplified by the third major part of the 1 µm pump, which is then fed into the experiment. Further details of this scheme are illustrated in Figure 5.7 and can be found in the originally published manuscript [119].

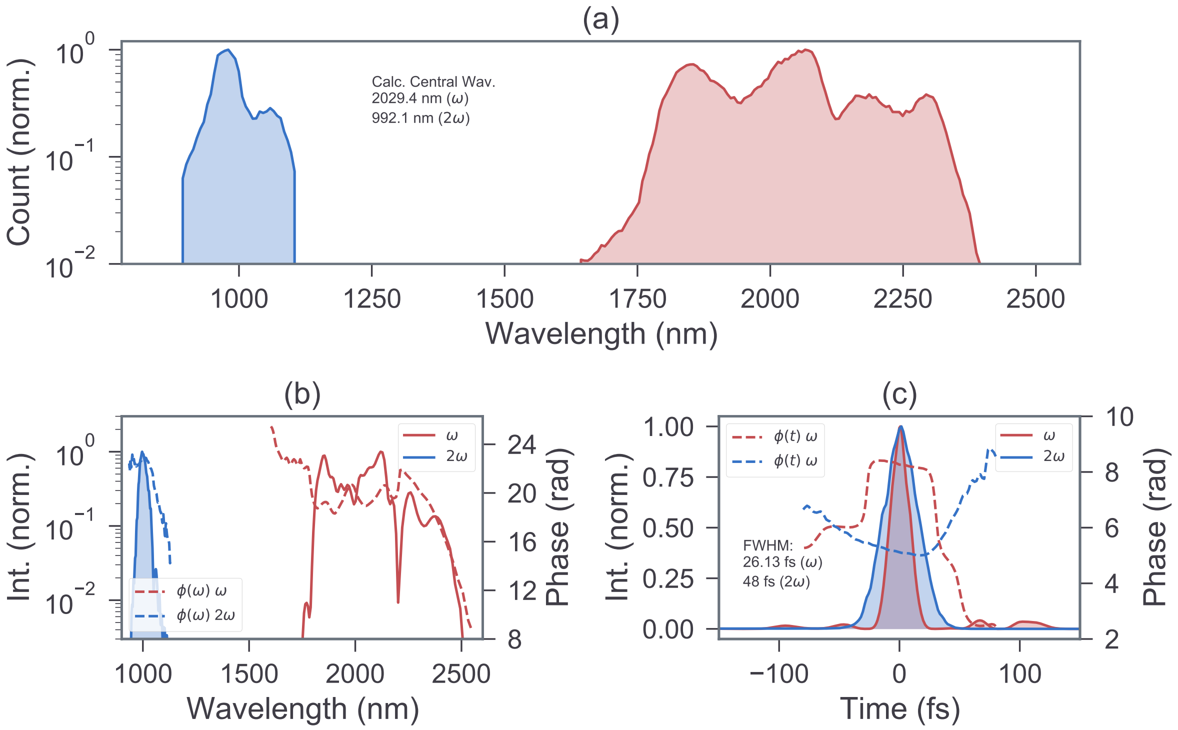

Figure 5.8: Spectral and temporal properties of the ω - 2ω trefoil pump pulses. Subplot (a) shows the measured laser spectra recorded after the interferometer, right before the focusing objective to give an accurate representation of the laser pulses used. The laser pulses are picked off from the same region for FROG retrieval. The retrieved spectra and temporal profile along with their phases are shown in subplots (b) and (c), respectively.

During the experiment, the average power obtained was between 5.5 W to 6 W, with a pulse duration of $\approx$ 25 fs at a repetition rate of 100 kHz. The typical spectrum obtained can be seen in Figure 5.8, with a central wavelength $\approx$ 2030 nm. The pulse duration was carefully characterized using the frequency-resolved optical gating (FROG) technique [152, 151], with a setup developed in-house. The characterization of the laser pulses is performed after they pass through the interferometer. They are picked up right before entering the reflective objective of the microscope arrangement to accurately determine the temporal character of the pulses used in the experiment. An SHG FROG was performed to characterize the 1 µm pulses in a Beta-Barium Borate (BBO) crystal, while the 2 µm pulses were characterized by surface third harmonic generation (THG) FROG on glass (NBK7), both in a non-collinear geometry. Surface-enhanced THG was used instead of bulk to decouple macroscopic propagation effects and hence relax the phase matching requirements for the 2 µm pulses, which otherwise require a BBO crystal cut at a different angle. The retrieved spectrum and temporal structure of the pulses along with their relative phase profiles are illustrated in Figure 5.8. The characterization process was repeated multiple times to optimize the thickness of the dispersion compensating CaF_2 windows which lead to an optimum temporal compression of the pulses.

5.2.5 Fabrication and characterization of monolayer hBN

In this experimental project, it is essential to use high-quality hBN monolayers, and hence a short review of how they are fabricated is described. Furthermore, as the hBN monolayers used in this experiment are obtained commercially, the results from in-house characterization schemes are also presented.

Fabrication techniques

Owing to its flat atomic structure with no bonds protruding out of the plane and a wide band gap of $\approx 5.9\,\text{eV}$ as a monolayer [8, 154], hBN has already found wide applicability as an ideal substrate or capping material for other transition metal dichalcogenide (TMDC) 2D materials or graphene, which are more prone to environmental degradation [38, 124, 123]. This requirement has already resulted in the development of multiple techniques for fabricating and isolating hBN monolayers. Namely, they can be classified into two broad categories. One is a top-down process where bulk hBN is obtained using processes like liquid or mechanical exfoliation, or two, where bottom-up processes like chemical vapor deposition (CVD) or molecular beam epitaxy (MBE) are implemented [99, 6]. Given the rapid development in the field and the experience necessary in developing these hBN samples, the ones used in this thesis are obtained directly from a commercial supplier (ACS Materials) who uses a CVD-based method. The hBN layers are then transferred to a fused silica substrate owing to its transparency in the near- or mid-infrared wavelength region, and hence supporting experiments in a transmission geometry as performed in this thesis. Although the exact details of the fabrication process used by the commercial supplier are not available in the public domain, a general description of the CVD process is presented in the following text.

As reported extensively in the literature, the growth mechanism of hBN by the CVD method is primarily assigned to three steps [81]. In the first step, the parent compound borazane (H_3BNH_3) or borazine ($B_3N_3H_6$) is decomposed into B and N at high temperatures. This is followed by the deposition and nucleation of nitrogen and boron on a metallic surface in the form of clusters. Finally, in the third step, the clusters grow into hBN islands and finally arrange to form continuous films on metal surfaces such as Cu or Ni. Finally, the hBN mono-layers are stamped from Cu onto a substrate of choice by using a copper etchant and a polymer [142]. The most important parameters for the experiment here are the grain size of a mono-crystalline hBN patch and the number of layers. As shown in the literature, the grain size is often controlled using the nucleation density, which has been found to be inversely proportional to the grain size [99]. The nucleation density is controlled by different mechanisms such as pre-oxidation of the Cu surface or foil, applying nano-particles on the copper surface, or altering the annealing conditions [18, 95]. In addition, the usage of dual temperature exposure, separately to the parent compound and the Cu foil furnace in a low-pressure environment has been shown to obtain large area monolayers of hBN [82].

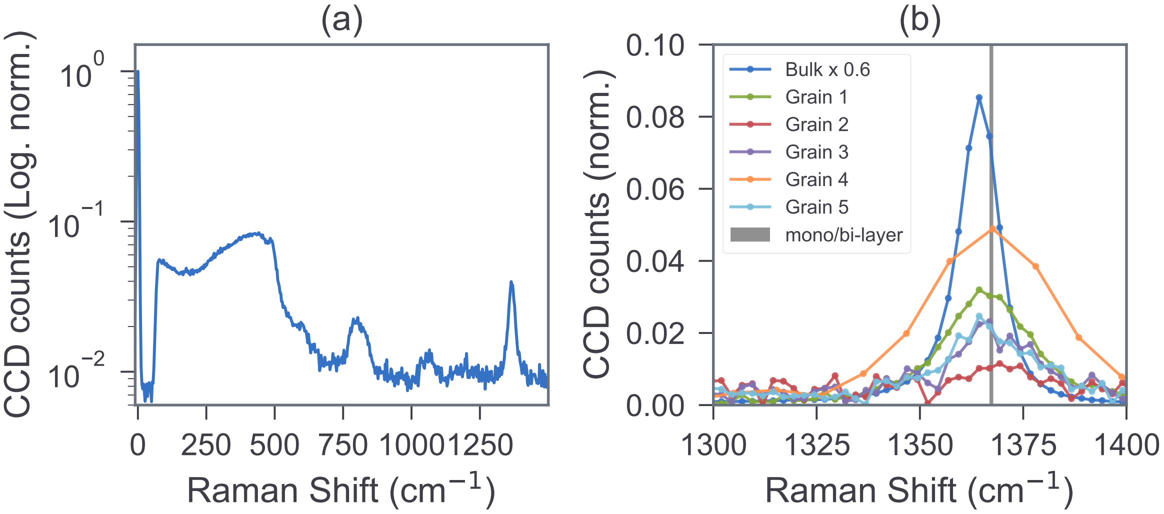

Figure 5.9: Raman spectra of hBN sample used in the experiment. Subplot (a) displays the full spectrum of the first grain measured by a Raman microscope on excitation with a CW pump (532 nm) showing an elastic peak at 0 cm^{-1}. A prominent Raman shift from hBN can be observed around 1365 cm^{-1}. Subplot (b) shows the Raman peaks (normalized to the pump peak at 0 cm^{-1}) for bulk hBN and different sites on the silica substrate with hBN monolayers. The shaded vertical line shows the region in which the Raman peak should lie for mono- or bi-layer hBN with respect to the bulk peak as reported in the literature [15].

Characterization technique: Raman microscopy

The gold standard for identifying the molecular structure of an unknown compound is through Raman spectroscopy. When light far below the material resonance impinges on an unknown molecular structure in question, it undergoes elastic or Rayleigh scattering by which a photon is absorbed by an electron raising its energy to a virtual state and then re-radiated at the same energy. Additionally, an inelastic scattering also occurs where light with slightly lower or higher energies is emitted and commonly referred to as a Stokes or anti-Stokes Raman scattering, respectively. This primarily occurs due to vibrational excitation or de-excitation [131]. Molecules exhibit unique vibrational energy states and measuring this shift in the photon energy with respect to the impinging pump photons provides a robust fingerprint of the investigated sample.

The samples used in this experiment were characterized using a commercial Raman imaging microscope (WITec, Oxford Instruments) with support from the group of Prof. Stefan Maier at LMU Munich. The results are illustrated in Figure 5.9. A CW pump laser centered at 532 nm with an average power of 62 mW was used to produce the Raman scattering, while a sensitive spectrometer recorded the Stokes-shifted Raman spectrum. The results not only confirm the existence of hBN on the fused silica substrate with a peak around 1365 cm^{-1}, but also exhibit a small downshift in the peak when compared to the bulk state hBN as also reported in the literature [50, 15]. In Figure 5.9, the total shift observed between the bulk and the grains lies within the range of the shifts observed by Cai et al. for mono- or bi-layer hBN on a substrate with respect to the peak observed for the bulk case. The figure also shows the Raman shift observed at different grain sites (randomly selected) where the majority appear to be either mono- or bi-layer hBN grains. Although this is a time-tested, robust technique, in this particular case, it is unable to reveal a clear distinction between mono- and bi-layers along with no information about the orientation of the crystal structure in question.

Characterization technique: SHG-polarization resolved microscopy

As a next step, to overcome the limitations of Raman spectroscopy, SHG-polarziation resolved microscopy is performed on the hBN-coated substrates. Here, below-resonant light is sent through the same microscope as shown in Figure 5.5 with the known polarization state and it leads to the generation of perturbative harmonics. Among them, the second harmonic is detected by a photodiode or spectrometer after being collected by the transmission objective with bandpass filters and eventually through a polarizer. The SHG is not only the strongest component but being an even harmonic, is a pure indicator of broken inversion symmetry in a crystal. Hence, the emission is also fully absent from the fused silica surface, leaving only odd layers of hBN (1L, 3L, 5L,...(2n+1)L), which break inversion symmetry to produce SHG. As 'n' increases, the magnitude of SHG drops [133]. Hence, a spatial scan over the substrate with the SHG strength as an optimization parameter leads to locating thinner odd layers of hBN. The Raman spectroscopy hints at primarily mono- or bilayer and hence the SHG technique is sensitive only to the mono-layers.

Another important advantage of this technique lies in the fact that it can be performed in situ during the final valleytronic experiment to make sure that all three probe and bi-circular pump pulses also excite the same hBN grain as independently observed given the above technique. This is performed by replacing the $\lambda/4$-wave plate right before the reflective objective as shown in Figure 5.1 with a $\lambda/2$-wave plate and only use the 2ω pump arm. The SHG produced by this 1 µm wavelength light is then easily picked up by the existing photodiodes and lock-in assembly with the appropriate filters.

Further, this technique not only allows the determination of inversion-symmetry breaking but also the orientation of the hBN crystals by observing the polarization response of the material. As described in section 2.3.3, the two unique light-induced oscillation directions (armchair and zigzag) make the outgoing SHG polarization rotate in the opposite direction and at twice the rate, as a function of the rotation of the incoming/pump light polarization. This has been also widely investigated and demonstrated in recent works [97, 133]. Two results from the hBN samples used are displayed in figure5.10. The characteristic four-lobe polarization-dependent signal implies that the interaction region of

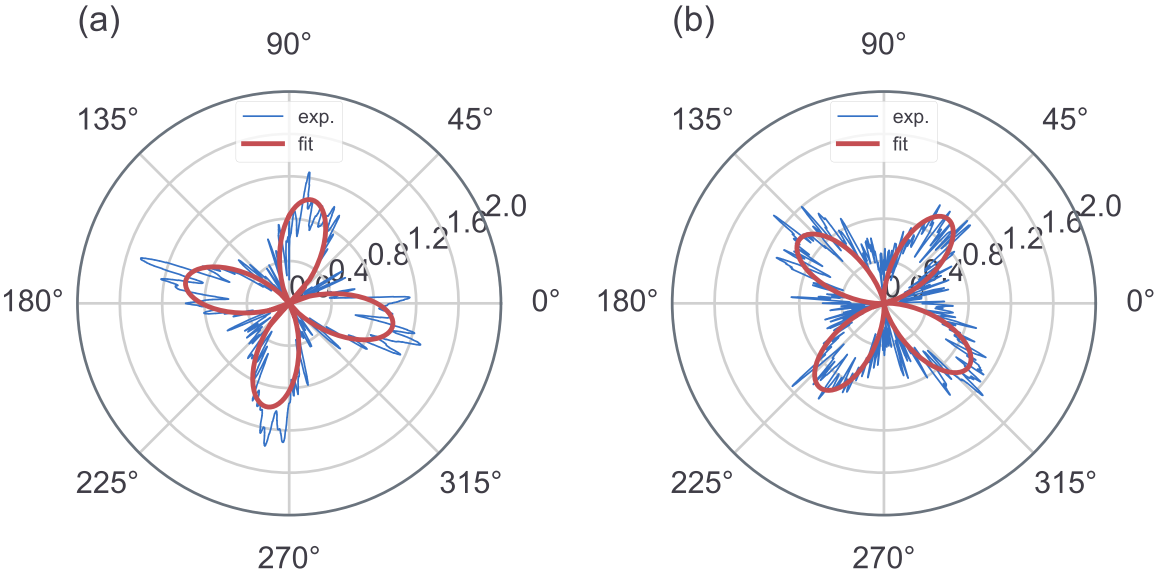

Figure 5.10: Polarization resolved SHG from few-odd-layer hBN. The rotation of SHG as a function of the polarization rotation of a linearly polarized pump pulse is illustrated here. The intensity of the SHG (normalized) is mapped after passing through a polarizer/Wollaston prism for few-odd-layer hBN patch site 1 in subplot (a) and patch site 2 in subplot (b) on a fused silica substrate. The fit function used is $Y_{fit} = A\cos\left(-2\theta + \varphi\right)^2$, where A is the amplitude of the oscillation and θ is the angle of the incoming pump polarization.

the laser irradiation is small enough (for the reflective objective used in the experiments). This way, the single crystalline orientation is dominant and does not get averaged out over multiple grains with different crystalline orientations. Further, one can observe that the four-lobe structure exhibits an angular offset with the four-lobe structure obtained from a neighboring hBN patch as shown in subplots (a) and (b) in Figure 5.10. This manifests from the hBN crystalline patches, themselves being oriented in arbitrary angles at different laser excitation sites. Usually, a six-lobe feature in the SHG signals can be used to indicate the orientation of hBN [97]. However, this requires either the whole sample to be rotated or the experiment to be carried out in the reflection geometry. A theoretical background to explain the four and six lobe structures is presented earlier in Section 2.3.1. Here, circularly polarized light is made linear and rotated at the same time by a polarizer right before the excitation, which subsequently also acts as an analyzer for the reflected SHG. Not only is it impossible to rotate the sample around one specific hBN patch axis but also to perform this experiment in reflection geometry. Instead, the crystalline angle can also be indirectly determined from a four-lobe structure [174]. In this thesis, it is not critical to obtain the angular offset of a particular hBN patch in question and hence further discussions are omitted.

The sensitivity of this technique to the presence of hBN on the fused silica substrate allows it to be used as a marker for laser-induced damage. Working with higher laser powers does not result in a higher signal-to-noise ratio, but a much stronger valleytronic effect and hence a helicity modulation as predicted theoretically in the literature [76]. However, the laser powers or intensities that can be used are primarily capped by the laser-induced damage threshold of hBN, which along with other 2D monolayers such as graphene occur at rather moderate values $\approx 1 \times 10^{12}\,\mathrm{W\,cm^{-2}}$.

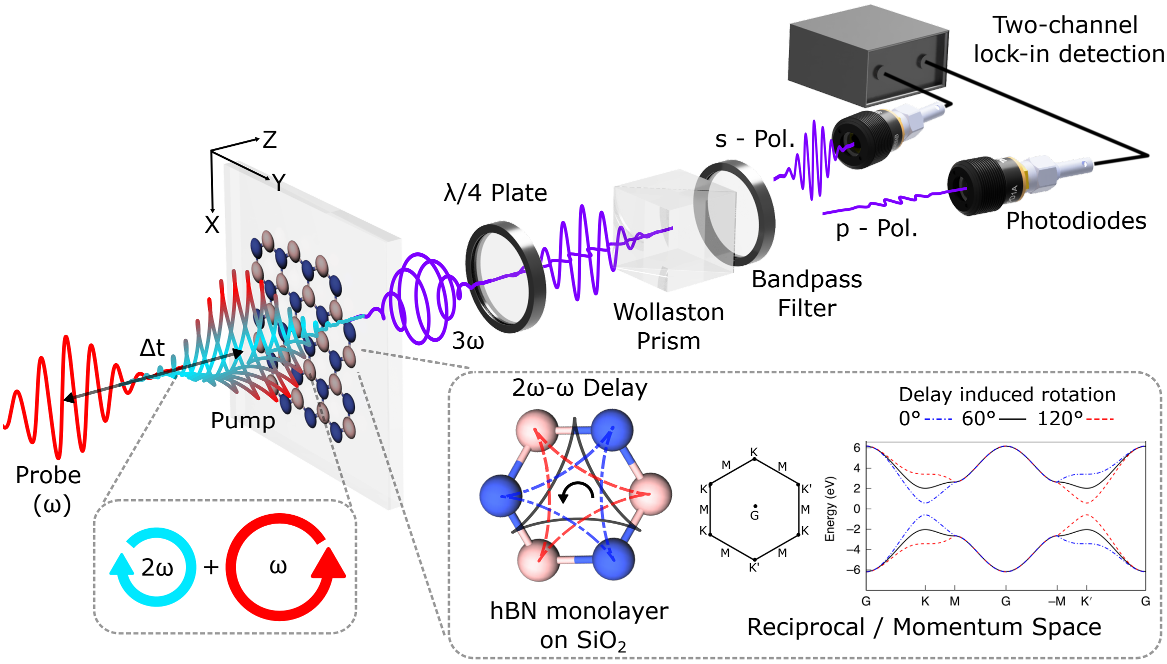

Figure 5.11: A schematic representation of the experimental scheme used to obtain the results is discussed in this section. The reflective objective indicates a tight focusing geometry which is essential in restricting the light-matter interaction down to a mono-crystalline hBN grain. The laser is exclusively represented in terms of its electric field structure in real space which interacts with hBN monolayers on a fused silica substrate. The reflective objective and recollimating optics before and after the sample, respectively are omitted for a clearer illustration of the helicity induced in the third harmonic of the probe pulse and its detection. Further details are elucidated in the text.

5.3 Results and discussion

After an overview of the theoretical and experimental background, the important results are highlighted and discussed in this section along with other measurements, supporting the claims and interpretations. An overview of the valleytronic control experiment is illustrated in Figure 5.11 and can be broken down into three segments. i) A below resonance selective excitation of the valleys in hBN, ii) Control or switching of the excitation from one valley to the other (K to K' or vice versa), and iii) Probing and detection of the valley that is excited. Additionally, numerically simulated results with the experimental parameters are presented to verify the results and interpretations obtained from the experiment.

5.3.1 Inducing valley-polarization (VP)

As a first step, a suitable monolayer hBN patch is located. This is done by blocking the ω pump and probe arms and using bandpass filters which allow the second harmonic of 2ω to pass through to the photodiodes as shown in Figure 5.11. A circularly polarized 2ω leads to circularly polarized 4ω, irrespective of the orientation of hBN, unlike linearly polarized excitation, and thereby evenly illuminates both the diodes after the Wollaston prism (see section 5.2.5). This allows the SHG intensity on any of the two photodiodes to be inversely mapped to the presence of the number of odd hBN layers. Thus, maximizing the SHG signal results in a mono or low odd layer hBN to be aligned in the focal spot of the 2ω pump arm. Given that the other pulses are already spatially and temporally overlapped, they are also automatically aligned on the same hBN patch. The detection scheme continues to operate as normal as the 2ω arm is modulated by a chopper and hence its modulated SHG is also picked up by the lock-in amplifier.

Subsequently, the ω-pump arm is unblocked and together with the 2ω arm, forms the bi-circular pump when they are perfectly temporally overlapped. The bandpass filter arrangement before the photodiodes are changed back to only allow 3ω to pass through. Any 3ω detected in this configuration is suppressed by optimizing the polarizer angle and the $\lambda/4$ plate right before the reflective objective which also optimizes the bicircularity of both the pump fields, as 3ω is forbidden by the selection rules with this combination. The 2ω arm is then set to a scanning mode where it is continuously shifted in time with a triangular function around the fully overlapped position, as also highlighted in Figure 5.4. This keeps rotating the trefoil shape of the effective electric field forth and back, exciting one particular valley as it orients itself along one sub-lattice of hBN in the real space as shown in the inset of Figure 5.11.

5.3.2 Helicity resolved harmonics - VP detection

As a next step, the probe (ω) pulses are exposed to the sample after being temporally delayed by $\approx 100\,\mathrm{fs}$ [2]. The polarization for this pulse is kept linear, as proposed in the theoretical section. The third harmonic of the probe pulse, which is induced by the pump field is then detected by the photodiodes and lock-in apparatus as any other source of the third harmonic (3ω) is not modulated, and hence not detected. As proposed in theory, a large contribution to these harmonics is the intraband oscillations of the electron population in the conduction band by the pump [76]. These intraband currents are influenced by the opposing pseudo magnetic field or berry curvatures of a particular valley, given by the

---

[2] The choice of this delay was found to be optimal experimentally and the dependence is further discussed in a later section.

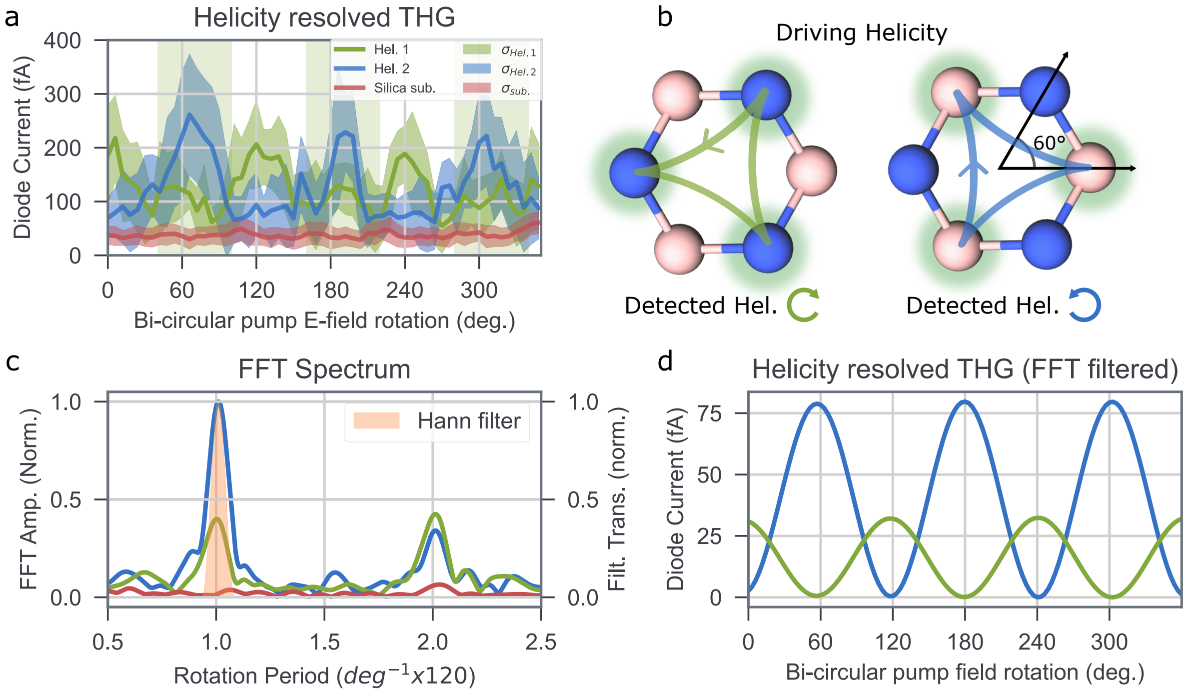

Figure 5.12: Experimentally obtained helicity-resolved third harmonic (HRTH) from hBN as a function of the pump laser-field rotation. a) Raw-experimental data of HRTH from hBN for both helicities of a bi-circular pump and that from fused silica. b) A schematic representation of the experiment, where one helicity of the third harmonic is enhanced by one helicity of the pump configuration, at the illustrated orientations. c) FFT spectrum of the raw experimental data over 2.5 full rotations of the pump showing a distinct and pre-dominant peak at $1\,{}^{\circ -1} \times 120$, corresponding to a peak every 120° rotation, which is absent from the underlying substrate. d) The inverse FFT of subplot c) after applying a Hann bandpass filter on the predominant spectral peak, clearly resolving an out-of-phase oscillation between the two different helicities (pump and detector) configurations.

anomalous hall conductivity (AHC) over the whole Brillouin zone (see equation 2.45). This in turn induces a helicity in the third harmonic signal of the probe, depending on the strength and sign of the AHC.

To resolve this, right after the emission is collected by the transmission objective, it passes through the $\lambda/4$ plate designed to work at a 3ω wavelength with its optical axis at 45° with respect to the Wollaston prism as shown in Figure 5.11. This arrangement maps the purely helical components of the harmonic to a unique ‘s’ or ‘p’ polarization, which is then spatially (angular) separated by the Wollaston prism and eventually picked up by two separate photodiodes. There still exists a linearly polarized component of the probe-THG which is made circular by the $\lambda/4$ plate and equally distributed onto the two photodiodes by the Wollaston prism. However, since the lock-in amplifier is only sensitive to changes induced by the pump, or more specifically a trefoil field structure, it is invisible to any linearly polarized signal generated by a perturbative third harmonic from hBN or fused silica substrate.

The results are captured in Figure 5.12, where subplot ‘a’ shows the third harmonic signal recorded on the diodes as a function of the trefoil pump rotation. Here, the data from the two diodes are from two different measurements, taken back to back having only the helicity of the trefoil pump being reversed in between. During a single measurement, it is impossible to obtain the third harmonic signal of the probe on both diodes at the same time, due to a large background signal on one of the diodes. Even around a delay of 100 fs, there still exists a small temporal overlap between the pump (2ω) and probe (ω) pulses. The linearly polarized probe pulse can be considered as having two equal components of right- and left-circularly polarized light and hence a two-photon response is allowed with the same helicity components of the pump and probe also leading to the generation of 3ω as also shown in Figure 5.3. The 3ω generated in this case is also circularly polarized and hence the $\lambda/4$ plate and Wollaston prism force it to fall only on a single photodiode, resulting in the strong background far above the SNR of the probe-induced THG from hBN and making one photodiode unusable for a single measurement.

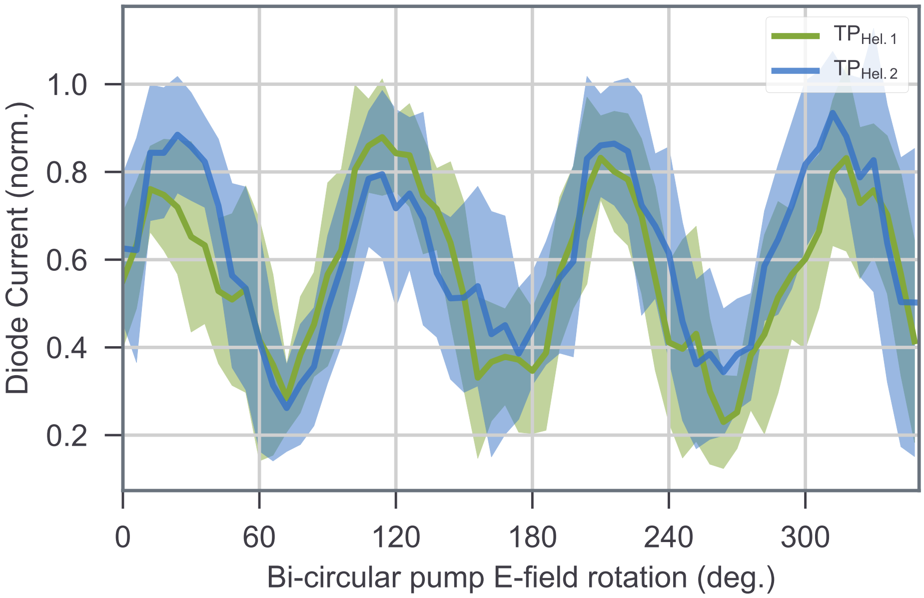

Figure 5.13: Interferometric modulation of a CW laser through the two pump arms recorded for both pump helicities. The data is recorded in parallel on an additional lock-in amplifier channel, along with the data recorded in Figure 5.12. The standard deviation in the data is represented in the shaded region. The interferometer drift, represented by an offset in the displayed oscillation, is corrected by applying an offset on the X-axis to one of the pump helicities. The same offset is applied to the data shown in Figure 5.12 (a).

To overcome this problem, the helicity of the pump is reversed which leads to a background or two-photon induced 3ω with the opposite helicity. An opposing helicity now falls on the other photodiode enabling the detection of the other helicity of the probe's third harmonic from hBN. The two helicity components of the third harmonic from hBN are represented in subplot 'a' of Figure 5.12. The two respective pump helicities used are depicted in subplot 'b'. As shown in Figure 5.2, a change in helicity does not change the angle of the trefoil, and hence the X axis of subplot 'a' is consistent for both the helicity plots. Although the helicities are reversed back to back within an interval of five minutes, drifts in the interferometer of the pump arm show up as drifts in the angle of the trefoil. This drift is monitored by sending an external CW laser through this interferometer as discussed earlier and later corrected during data processing. The modulation of this interferometer is shown in Figure 5.13.

Although the HRTH is only shown for a pump rotation of 360°, the data is recorded for a larger pump rotation of over $4 \times 360°$. Since the SNR of this observable is so low, better statistics are collected by rotating the pump back and forth over this angular interval, as also shown in Figure 5.4 for a smaller scanning interval. The solid line in Figure 5.12 (a) is produced by taking the statistical mean of all the photodiode-current data points recorded within a bin size of 3°, while the shaded region depicts their respective standard deviation. Although the statistical mean exhibits a clear modulation with a periodicity of 120°, the data is still too noisy to carry out systematic measurements where small changes in the strength of the modulation can be used.

Fourier analysis

Hence, an additional Fourier analysis is carried out for a more sensitive extraction of the modulation strength. Figure 5.12 c, displays the Fourier spectrum obtained upon performing a Fast Fourier transform (FFT) on the HRTH data as a function of pump rotation over the fully recorded $4 \times 360°$ rotation. A better resolution is obtained in Fourier space by first zero padding the data to artificially create a long angle rotation axis. Further, given the abrupt change to zero signal on the X axis due to a limited pump rotation recorded, a Tukey window is applied to smoothly suppress the edges in order to avoid high-frequency ripples due to the sharp edges [57]. The window can be expressed as

$$W_{tukey}(x) = \begin{cases} 0.5(1+\cos(\frac{\pi(|x-M|-\alpha M)}{(1-\alpha)M})), \ |x-M| \geq \alpha M \\ 1, \ |x-M| < \alpha M \end{cases} \tag{5.15}$$

where N is the length of the X axis of our data set and $M = (N-1)/2$, $x = 0, 1, 2..., N-1$ and α is a constant between zero and one and it determines the smoothness of the edges where $\alpha = 1$ corresponds to a rectangular window. In the data analyzed here, the value of α is set to 0.5.

A clear peak is observed in the Fourier spectrum in Figure 5.12 (c) corresponding to a modulation periodicity of 120°. This is expected from a single helicity of the HRTH as it is only sensitive to a single valley polarization and hence, appears only when the pump trefoil orients itself to either the boron or nitrogen sublattices which are separated by 120°. Similarly, the opposite helicity corresponds to the pump trefoil orienting itself to the nitrogen or boron sublattices also exhibiting a periodicity of 120°. However, given the angular separation of 60° between boron and nitrogen, the two opposing HRTH oscillations also exhibit a phase difference of 60°. Finally, an inverse FFT is performed by applying a bandpass filter on the relevant FFT peak. As shown in Figure 5.12 (d), the extracted components from the two different helicities are at an offset of 60°.

5.3.3 Intensity dependence of resolved helicity

Once the FFT peaks are extracted from the recorded datasets, their maxima can be used to identify the strength of HRTH and hence easily represented as a function of an additional scanned parameter. Intensity scans can reveal the physics of materials as their scaling uncovers the typical non-linearities involved. Here too, an intensity dependence experiment was performed where the scaling of HRTH was recorded as a function of the pump intensity[3] and secondly the probe intensity. As shown in Figure 5.14, the strength of helicity modulation was recorded as a function of the pump and probe intensity. The actual scaling value is determined through a fit of the form

$$F_{\text{fit}}(I) = AI^n \tag{5.16}$$

where 'n' is the extracted scaling and 'A' is a prefactor. The HRTH is found to scale with power $n = 2.6, 3.1$ with the pump and probe, respectively. The intensities were varied by controlling a neutral density filter wheel placed in the pump arm through which the ω and 2ω beams both passed through and another separately in the probe arm. Their input power was recorded for each data set to estimate the intensity. During the experiment where the pump power was varied, the input power was recorded using a Si photodiode, sensitive to the 2ω component. This power was continuously recorded during the experiment by the lock-in amplifier and the error bars in the upper left subplot of Figure 5.14 represent the statistical standard deviation as obtained in the case of the raw helicity data. Similarly, the power was also recorded for the probe scan shown in the upper right subplot of Figure 5.14. However, in the case of the probe scan, its power was recorded using a thermal power sensor and only once before each dataset was stored. A constant standard deviation of 10 % of the measured power is assumed as was independently determined from a data set over a period of 5 min. The absolute intensities used for the X axes are determined using an additional experiment where a thin Quartz (0001) substrate was damaged using the 2 µm circularly polarized pump pulses. The power at which damage occurred was recorded by increasing the power until filamentation and visible harmonics were observed. The reference intensity for damage is obtained from the literature [165]. Given that the damage threshold is reported for a wavelength of 800 nm and the more accurate threshold is unknown for the wavelengths used in the experiment, it should be assumed that there could be a large error in the absolute scale. However, the intensity scaling, which is the primary focus here should remain unaltered.

---

[3] Both ω and 2ω components are varied at the same time keeping their relative intensity constant.

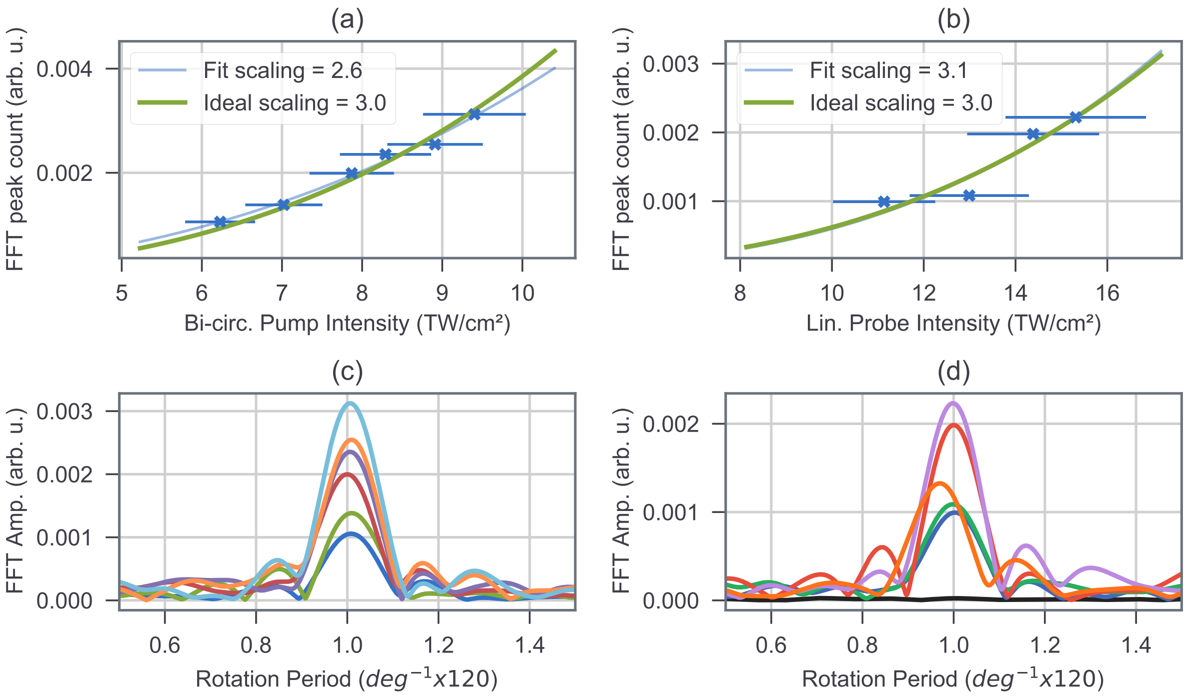

Figure 5.14: HRTH strength from FFT peaks as a function of the bicircular pump ($\omega - 2\omega$) and linearly polarized probe (ω) intensity on hBN. Plots (a) and (b) display the strength of the FFT peak for the 120° modulation recorded as a function of the pump and probe intensity, respectively. The transparent blue line represents a fit of the data points and the green line represents an ideal scaling with the third power of the input intensity. Plots (c) and (d) display the FFT spectrum of the recorded data sets (corresponding to plot (a) and (b), respectively) from where the peak values were used for the intensity scaling and fitting.

The harmonics generated by the probe pulse are considered to be emanating from induced intraband currents by the probe [153, 76, 51], while the bands are already valley selectively populated by the pump pulse [76]. Thus, if the power of the pump pulse is exclusively varied, the harmonic (3ω) yield is expected to scale with $n = 3$ which is within the error bar of the experimentally obtained scaling of $n = 3.1$ as shown in Figure 5.14. However, one could argue that all of the 3ω components arising from the ω probe pulse, especially of that from the substrate would also scale with the same power. This argument is countered by the lock-in scheme used here (Ref. subsection 5.2.3) where the recorded scaling is not only invisible to all the components which are not correlated with the pump (2ω pump modulation by the chopper), but also components which exhibit no modulation with the trefoil pump rotation as the Y axis (Figure 5.14) exclusively maps the amplitude of this modulation. Additionally, any 3ω component arising exclusively from the pump pulses is already minimized by optimizing their bicircularity (counter-rotating).

5.3.4 Pump-probe delay dependence of resolved helicity

The pump-induced valley polarization or valley selective excitation eventually decays in time and hence makes it necessary to probe this event with a laser pulse that is even shorter. Previously, using photo-luminescence measurements the valley polarization decay time of WSe_2 was estimated to be of the order of a few picoseconds [156]. More recent improved measurement techniques have estimated the valley lifetime and valley coherence decay times to be ≈ 200 fs and 100 fs, respectively [56, 144].

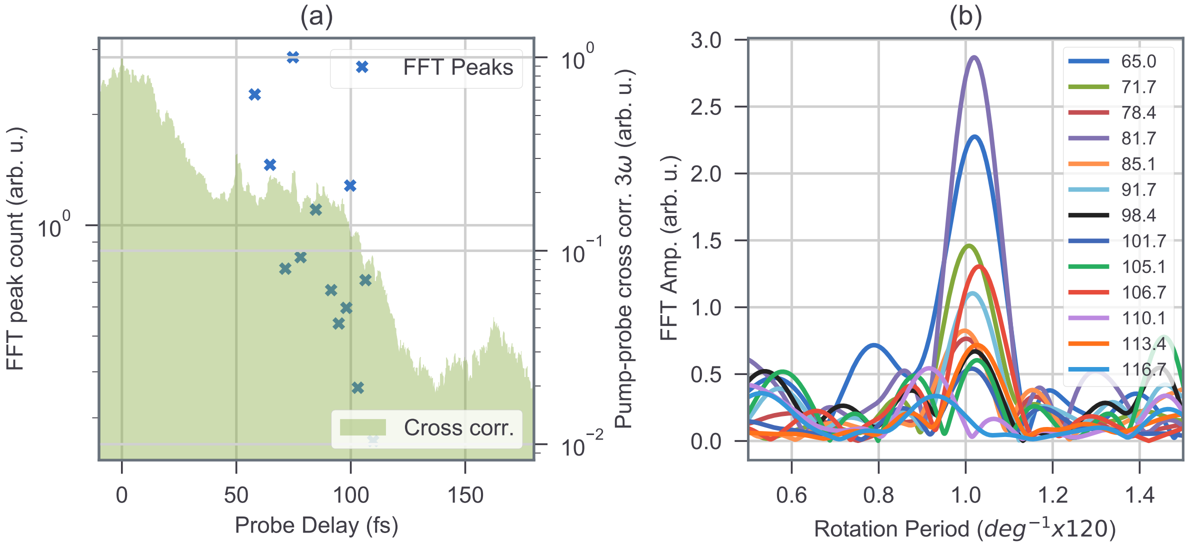

Figure 5.15: Pump-probe delay dependence of resolved helicity of third harmonic. (a) Helicity change plotted against the probe pulse delay showing a cross-correlation measurement (shaded green) where the observable is the two-photon response of the ω probe pulse and 2ω pump pulse on the fused silica substrate. The blue crosses represent the HRTH magnitude extracted from an FFT of the angle-dependent data as a function of the pump-probe delay. (b) The raw FFT spectrum around the modulation period which corresponds to 120° is displayed for various probe delay points marked as a legend in units of fs.

Given the lack of any experimental or theoretical data in this regard for hBN, the linearly polarized probe pulse was scanned to find the optimum position to perform the experiments. As mentioned in section 5.3.2, a pump rotation scan was carried out to extract the respective Fourier peak (HRTH) for a fixed pump-probe delay ranging from picoseconds to temporal overlap with the pump. Such a large range could not be scanned during a single experimental session given the amount of time a single delay point took due to the trefoil rotation scan, and hence, different ranges were recorded in different experimental sessions. Thus, Figure 5.15 only contains the largest data set captured during a single experimental session in the most relevant region where the strongest HRTH signals (proportional to the valley polarization) were observed. Combining different data sets are misleading as they contain HRTH signal from different hBN grain sites and other experimental conditions leading to altered overall signal strength. The HRTH signal beyond $\approx$ 120 fs pump-probe delay falls below the noise floor of the system and remains unresolved. In the other direction, although the signal steadily increases the signals appear quite abrupt and the error appears too high to fit a decay curve with confidence. However, from this data, we can place a lower bound on the valley polarization decay time to be $\geq$ 100 fs. Below delays of $\approx 50 - 60$ fs, the signal starts dropping significantly which may be an indication of damage to the hBN grain in question or significant perturbation of the pump field leading to a deviation from the trefoil structure. Numerical simulations by Alvaro Jiménez-Galán for similar experimental parameters where the probe starts to overlap with the pump show the same trend where the HRTH trefoil angle dependence disappears.

5.3.5 Numerical results

The results from the numerical simulations presented in section 2.3.3 from the work of Jiménez-Galán and co-workers were performed using different parameters as compared to the experiments reported in this chapter. First, a longer wavelength of 3 µm was used as the fundamental wavelength (ω) while the experiments here use 2 µm, given the availability of a suitable laser system operating at this wavelength. Secondly, a pulse duration of 200 fs was used for all the pulses while the experimentally used pulse durations here lie between 26 fs and 48 fs. Thus, the numerical simulations were repeated using the experimentally relevant parameters in a two-band model by the theory collaborators on this project led by Alvaro Jiménez-Galán, and hence using the same numerical methods [145, 76]. The change in pulse duration does not play a critical role here as it still is a multi-cycle pulse and a decay of the valley polarization is not accounted for in the calculation. However, the wavelength has already been shown to have a strong dependence on valley polarization. The valley polarization is directly proportional to the wavelength and hence it is critical to estimate the effect at smaller wavelengths as applicable in the experiments.

Role of probe polarization direction on AHC and HRTH

The results of the calculations are concisely presented in Figure 5.16, where the primary observable is the two different HRTH corresponding to two possible helicities of light polarization as a function of the rotation of the pump trefoil structure. The modulation in this function is directly linked to the AHC and thereby valley polarization as described in section 2.3.3, Figure 2.11, and in the literature [76]. However, in contrast to previous representations, here, instead of a derived asymmetry parameter between two helicities, both HRTH components are individually extracted. This configuration is very close to what is obtained and plotted from the experiment. The only difference is that one diode or helicity component is usable as the other is overpowered by a strong background signal.

The results shown in the subplot (a) of Figure 5.16 display this HRTH and at a first glance appear a bit counterintuitive in comparison to Figure 2.11. The asymmetry plot

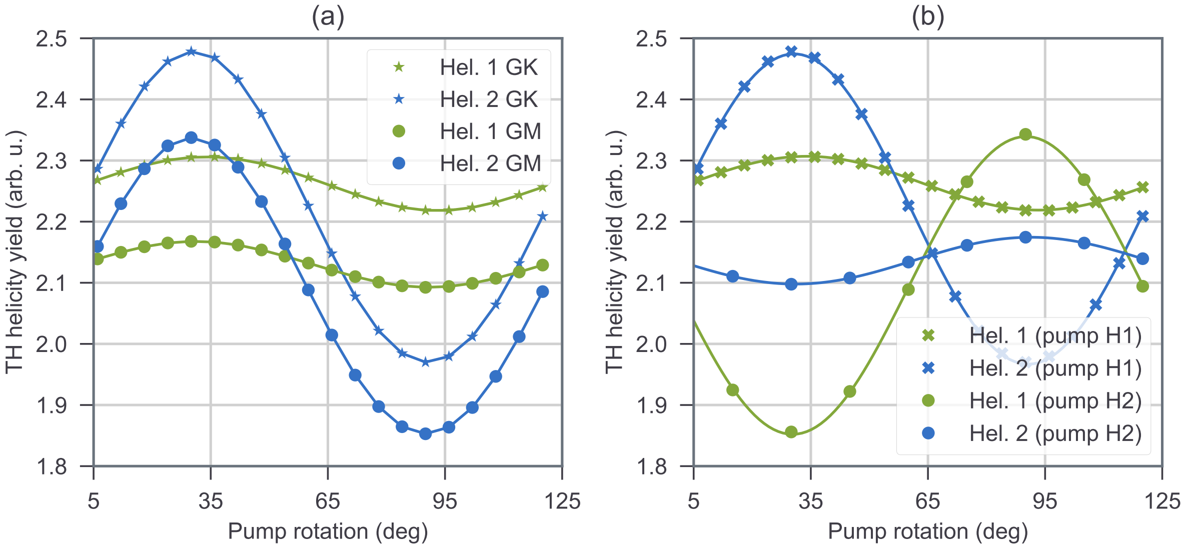

Figure 5.16: Simulated HRTH using experimentally relevant parameters as a function of the pump trefoil rotation where two unique helicities are labeled as 'Hel. 1' and 'Hel. 2'. Subplot (a) compares this behavior when the linearly polarized probe pulse is aligned along the G-K direction vs. when it is aligned along the G-M direction in the Brillouin zone. Subplot (b) illustrates the same behaviour but for different pump trefoil helicities ('H1' and 'H2'), as performed in the experiment. The points represent real data while the lines connecting them are constructed using a sinusoidal fit. The data has been provided by Alvaro Jiménez-Galán.

usually implies that the raw helicity values oscillate out of phase with each other w.r.t. the pump rotation, but as seen from the calculations here, the asymmetry can also be from a difference in the strength of the two helicity modulations which are in phase. Here, one of the oscillations corresponds to what is observed in the experiment and is shown in Figure 5.12 (a) and (d). In comparison, the periodicity of modulation of 120° extracted from the delay of the 2ω arm in the experimental plot perfectly matches the calculation. A comparison in strength with the second helicity is unfortunately not obtainable from the experiment. In the experiment, the polarization direction of the probe pulse was not varied with each hBN grain orientation as it was challenging to do that while preserving the linear polarization contrast at the same time. Hence, the probe polarization direction w.r.t. the Brillouin zone was arbitrary in the experiments. Further, no significant differences were observed when the experiment was repeated on multiple hBN grains implying different probe polarization directions. This observation is in agreement with theory as shown in Figure 5.16 (a), where the HRTH is compared between the two orthogonal directions in the Brillouin zone (G-M versus G-K). The only difference observed is a slightly reduced (DC shift) helicity strength while the modulation strength, period, and phase of modulation remain the same.

Role of trefoil pump helicity

As discussed earlier, since one of the helicities of the HRTH cannot be extracted from the experiment due to a strong background, the experiments were repeated where a reversal of the helicity of the bicircular field, the background (circularly polarized) also switches to the other diode. This was achieved by rotating the final $\lambda/4$ plate by 90 deg and given the nature of the laser field (see section 5.2.1), it does not affect the orientation of the trefoil and hence also the valley polarization. Experiments in this reversed pump helicity configuration led to an oscillation of the HRTH of the opposite helicity component with the same periodicity but out of phase with the oscillation from the pump with the original helicity and is illustrated in Figure 5.12 (d). Similarly, the numerical simulations also reproduce the exact behavior as illustrated in Figure 5.16 (b) for both the cases in the probe polarization in the G-K direction. This correlation between the numerical results and the experiment further confirms the origin of this modulation to arise from a modulating AHC induced by valley polarization, controlled by the rotation angle of the trefoil-shaped pump field.

5.4 Summary and outlook

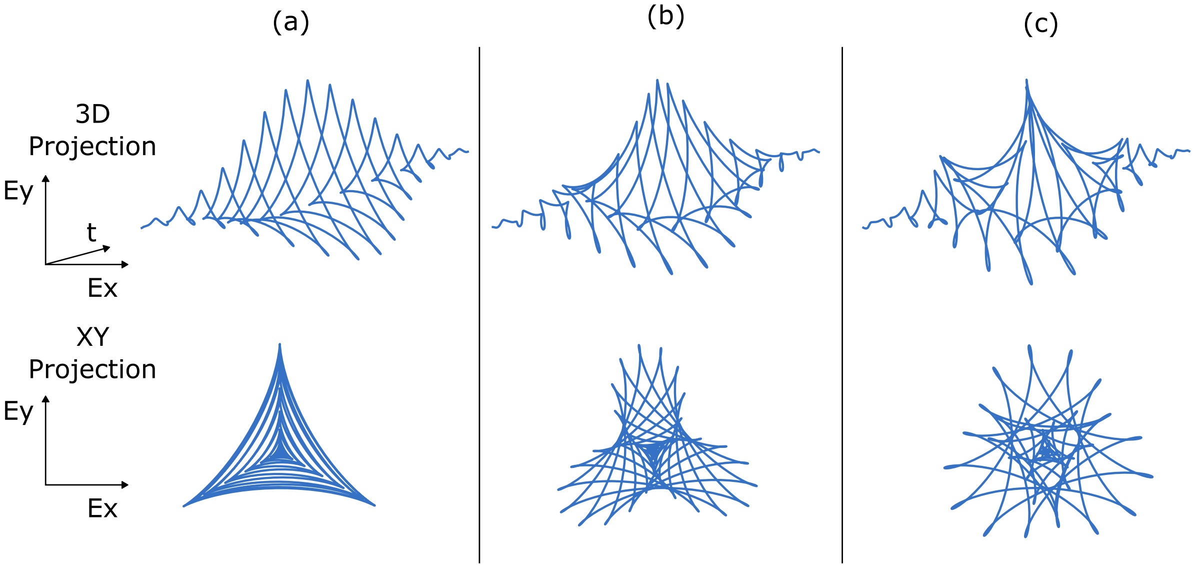

Figure 5.17: Calculated laser pulse shapes for trefoil pump pulses generated with counter-rotating bicircular fields with incommensurate harmonics to induce single-cycle trefoil field rotation. Here the combination used is $\omega + n\omega$ where $n = 2, 2.1, 2.2$ in (a), (b), and (c) respectively.

In conclusion, an experimental scheme was designed and developed to observe the effect of strongly tailored off-resonant light fields with a 2D inversion symmetry broken material, as theoretically proposed by Alvaro Jiménez-Galán and coworkers for longer wavelengths [76]. The experiments used CVD-grown hBN and the results reveal a clear change in the helicity of the third harmonic (3ω)[4] as a function of an off-resonant trefoil shaped pump rotation with a periodicity of 120°, exactly matching numerical simulations demonstrating all optical and off-resonant valleytronic control and read out. The signal is independently verified to be originating from hBN with the help of reference measurements only from the fused silica substrate and only in the presence of all three pulses (ω, 2ω, ω). A separate experiment is carried out in parallel to find mono- or odd-layer hBN grains in situ by probing inversion-symmetry-breaking induced surface second harmonic generation[97].

Although light-field valleytronic control is demonstrated by rotating the trefoil structure, the speed of rotation in the current scenario is still relatively slow and can get only as fast as the piezo-based delay stage, delaying one pump arm. To overcome this limit and truly test how this control can be imparted on a single-cycle or even sub-cycle level, inducing a delay using a piezo stage will not work. Such rotation within the pump is induced either by introducing a certain amount of chirp through dispersion or by slightly varying the central wavelength of the second harmonic or the fundamental. Figure 5.17 highlights such pulse engineering where the second harmonic component of the pump is slightly tuned. As observable in the figure, the difference in rotation between each full cycle is proportional to the deviation of the harmonics from 2. Experimentally this could be induced by altering the angle of the $LiNbO_3$, but the intensity ratio and temporal and spatial overlap would also need to be kept constant. Theoretically, it would also be worth questioning what is the effect and strength of the AHC within a trefoil laser cycle as all previous calculations show results that are averaged over one full cycle.

The works by our theory collaborators additionally highlight that using the tailored pump pulses as realized in this thesis, could result in even stronger band structure modification. The implication is that it could lead to a scenario where a full band-gap closure at one of the valleys K or K', thereby driving a phase transition [145, 76]. Given the clear signature of helicity changes that can be observed with the setup developed here, one could expect to clearly observe this effect which emanates in the form of a sign reversal of the helicity as demonstrated in the theoretical works [145]. However, a possible phase transition in hBN could not be explored as the damage threshold was reached before reaching sufficient intensities as predicted in the literature. Given the advancement of laser technology in terms of ultrashort high power, long wavelength laser sources [98, 120, 147], this scheme could be well-tested at longer wavelengths using the same experimental scheme, which relaxes the intensity requirements [76]. Although recent experiments in the literature have already observed a phase transition by high harmonic generation in a 3D topological insulator, the process was induced through a slow and permanent chemical alteration of the material [61]. Thus, the prospects of light-induced ultrafast phase transitions in topological materials remain something to look forward to.

---

[4] Third harmonic of a linearly polarized off-resonant pulse

Appendix A

Data Archiving

All the raw data, which has been used to produce the content of this thesis, along with its usage guideline, can be found archived on the Data Archival Server of the Laboratory for Attosecond Physics at the Max-Planck-Institute of Quantum Optics under the following location:

```
/afs/rzg/mpq/lap/publication_archive/
```

Bibliography

[1] S. Adachi, M. Sato und T. Suzuki, *The Journal of Physical Chemistry Letters* **6** (2015), 343.

[2] C. Altucci, T. Starczewski, E. Mevel, C.G. Wahlström, B. Carré und A. L'Huillier, *Journal of the Optical Society of America B* **13** (1996), 148.

[3] M.V. Ammosov, N.B. Delone und V.P. Krainov, *Journal of Experimental and Theoretical Physics* **64** (1986), 1191.

[4] A.R. Attar, A. Bhattacherjee, C.D. Pemmaraju, K. Schnorr, K.D. Closser, D. Prendergast und S.R. Leone, *Science* **356** (2017), 54.

[5] A. Autere, H. Jussila, Y. Dai, Y. Wang, H. Lipsanen und Z. Sun, *Advanced Materials* **30** (2018), 1705963.

[6] W. Auwärter, *Surface Science Reports* **74** (2019), 1.

[7] M. Bellini, C. Lyngå, A. Tozzi, M.B. Gaarde, T.W. Hänsch, A. L'Huillier und C.G. Wahlström, *Physical Review Letters* **81** (1998), 297.

[8] G. Bhimanapati, N. Glavin und J. Robinson. *Chapter Three - 2D Boron Nitride: Synthesis and Applications*, Band 95 von *Semiconductors and Semimetals.* Elsevier, 2016. Seiten 101–147.

[9] V.A. Birulia und V.V. Strelkov, *Physical Review A* **99** (2019), 043413.

[10] R. Boyd und D. Prato: *Nonlinear Optics.* Elsevier Science, 2008.

[11] F. Brizuela, C.M. Heyl, P. Rudawski, D. Kroon, L. Rading, J.M. Dahlström, J. Mauritsson, P. Johnsson, C.L. Arnold und A. L'Huillier, *Scientific Reports* **3** (2013), 01410.

[12] B.Schmidt, M.Hacker, G.Stobrawa und T.Feurer. *LAB2-A virtual femtosecond laser lab.*

[13] C. Burger, W.F. Frisch, T.M. Kardaś, M. Trubetskov, V. Pervak, R. Moshammer, B. Bergues, M.F. Kling und P. Wnuk, *Optics Express* **25** (2017), 31130.

[14] A. Butler, D.J. Spence und S.M. Hooker, *Physical Review Letters* **89** (2002), 185003.

[15] Q. Cai, D. Scullion, A. Falin, K. Watanabe, T. Taniguchi, Y. Chen, E.J.G. Santos und L.H. Li, *Nanoscale* **9** (2017), 3059.

[16] W. Cao, P. Lu, P. Lan, X. Wang und G. Yang, *Physical Review A* **74** (2006), 063821.

[17] Y. Cao, V. Fatemi, S. Fang, K. Watanabe, T. Taniguchi, E. Kaxiras und P. Jarillo-Herrero, *Nature* **556** (2018), 43.

[18] R.J. Chang, X. Wang, S. Wang, Y. Sheng, B. Porter, H. Bhaskaran und J.H. Warner, *Chemistry of Materials* **29** (2017), 6252.

[19] Z. Chang, *Physical Review A* **70** (2004), 043802.

[20] Z. Chang, *Physical Review A* **71** (2005), 023813.

[21] Z. Chang: *Fundamentals of Attosecond Optics.* CRC Press, 2016.

[22] Z. Chang, *Optics Express* **26** (2018), 33238.

[23] J. Cheng, D. Huang, T. Jiang, Y. Shan, Y. Li, S. Wu und W.T. Liu, *Optics Letters* **44** (2019), 2141.

[24] M. Chini, S. Gilbertson, S.D. Khan und Z. Chang, *Optics Express* **18** (2010), 13006.

[25] L.E. Chipperfield, J.S. Robinson, J.W.G. Tisch und J.P. Marangos, *Physical Review Letters* **102** (2009), 063003.

[26] A. Ciriolo, M. Negro, M. Devetta, E. Cinquanta, D. Faccialà, A. Pusala, S.D. Silvestri, S. Stagira und C. Vozzi, *Applied Sciences* **7** (2017), 265.

[27] E. Constant, D. Garzella, P. Breger, E. Mével, C. Dorrer, C. Le Blanc, F. Salin und P. Agostini, *Physical Review Letters* **82** (1999), 1668.

[28] P.B. Corkum, *Physical Review Letters* **71** (1993), 1994.

[29] P.B. Corkum, N.H. Burnett und M.Y. Ivanov, *Optics Letters* **19** (1994), 1870.

[30] P.B. Corkum und F. Krausz, *Nature Physics* **3** (2007), 381.

[31] A. Couairon, E. Brambilla, T. Corti, D. Majus, O. de J. Ramírez-Góngora und M. Kolesik, *The European Physical Journal Special Topics* **199** (2011), 5.

[32] S.L. Cousin, N. Di Palo, B. Buades, S.M. Teichmann, M. Reduzzi, M. Devetta, A. Kheifets, G. Sansone und J. Biegert, *Physical Review X* **7** (2017), 041030.

[33] J.M. Dahlström, A. L'Huillier und J. Mauritsson, *Journal of Physics B: Atomic, Molecular and Optical Physics* **44** (2011), 095602.

[34] Y. Deng, Y. Yu, M.Z. Shi, Z. Guo, Z. Xu, J. Wang, X.H. Chen und Y. Zhang, *Science* **367** (2020), 895.

[35] T. Diskin und O. Cohen, *Optics Express* **22** (2014), 7145.

[36] G. Doumy, J. Wheeler, C. Roedig, R. Chirla, P. Agostini und L.F. DiMauro, *Physical Review Letters* **102** (2009), 093002.

[37] N. Dudovich, O. Smirnova, J. Levesque, Y. Mairesse, M.Y. Ivanov, D.M. Villeneuve und P.B. Corkum, *Nature Physics* **2** (2006), 781.

[38] C. Elias, P. Valvin, T. Pelini, A. Summerfield, C.J. Mellor, T.S. Cheng, L. Eaves, C.T. Foxon, P.H. Beton, S.V. Novikov, B. Gil und G. Cassabois, *Nature Communications* **10** (2019).

[39] D. Faccialà, S. Pabst, B.D. Bruner, A.G. Ciriolo, S. De Silvestri, M. Devetta, M. Negro, H. Soifer, S. Stagira, N. Dudovich und C. Vozzi, *Physical Review Letters* **117** (2016), 093902.

[40] D. Faccialà, S. Pabst, B.D. Bruner, A.G. Ciriolo, M. Devetta, M. Negro, P.P. Geetha, A. Pusala, H. Soifer, N. Dudovich, S. Stagira und C. Vozzi, *Journal of Physics B: Atomic, Molecular and Optical Physics* **51** (2018), 134002.

[41] P.A. Franken, A.E. Hill, C.W. Peters und G. Weinreich, *Physical Review Letters* **7** (1961), 118.

[42] M.V. Frolov, N.L. Manakov, A.A. Silaev und N.V. Vvedenskii, *Physical Review A* **81** (2010), 063407.

[43] M. Fushitani und A. Hishikawa, *Structural Dynamics* **3** (2016), 062602.

[44] T. Gaumnitz, A. Jain, Y. Pertot, M. Huppert, I. Jordan, F. Ardana-Lamas und H.J. Wörner, *Optics Express* **25** (2017), 27506.

[45] A.K. Geim und K.S. Novoselov, *Nature Materials* **6** (2007), 183.

[46] M. Geissler, G. Tempea, A. Scrinzi, M. Schnürer, F. Krausz und T. Brabec, *Physical Review Letters* **83** (1999), 2930.

[47] S. Ghimire und D.A. Reis, *Nature Physics* **15** (2018), 10.

[48] S. Gilbertson, Y. Wu, S.D. Khan, M. Chini, K. Zhao, X. Feng und Z. Chang, *Physical Review A* **81** (2010), 043810.

[49] A.J. Gonsalves, F. Liu, N.A. Bobrova, P.V. Sasorov, C. Pieronek, J. Daniels, S. Antipov, J.E. Butler, S.S. Bulanov, W.L. Waldron, D.E. Mittelberger und W.P. Leemans, *Journal of Applied Physics* **119** (2016), 033302.

[50] R.V. Gorbachev, I. Riaz, R.R. Nair, R. Jalil, L. Britnell, B.D. Belle, E.W. Hill, K.S. Novoselov, K. Watanabe, T. Taniguchi, A.K. Geim und P. Blake, *Small* **7** (2011), 465.

[51] E. Goulielmakis und T. Brabec, *Nature Photonics* **16** (2022), 411.

[52] D. Griffin und J. Lim, *IEEE Transactions on Acoustics, Speech, and Signal Processing* **32** (1984), 236.

[53] D. Griffiths: *Introduction to Electrodynamics.* Pearson Education, 2014.

[54] F.D.M. Haldane, *Physical Review Letters* **61** (1988), 2015.

[55] K.R. Hamilton, H.W. van der Hart und A.C. Brown, *Physical Review A* **95** (2017), 013408.

[56] K. Hao, G. Moody, F. Wu, C.K. Dass, L. Xu, C.H. Chen, L. Sun, M.Y. Li, L.J. Li, A.H. MacDonald und X. Li, *Nature Physics* **12** (2016), 677.

[57] F. Harris, *Proceedings of the IEEE* **66** (1978), 51.

[58] M. Hatayama, S. Ichimaru, T. Ohcni, E.J. Takahashi, K. Midorikawa und S. Oku, *Optics Express* **24** (2016), 14546.

[59] H.A. Haus. *Short pulse generation.* Cambridge Studies in Modern Optics. Cambridge University Press, 1995. Seite 1–56.

[60] X. He, J.M. Dahlström, R. Rakowski, C.M. Heyl, A. Persson, J. Mauritsson und A. L'Huillier, *Physical Review A* **82** (2010), 033410.

[61] C. Heide, Y. Kobayashi, D.R. Baykusheva, D. Jain, J.A. Sobota, M. Hashimoto, P.S. Kirchmann, S. Oh, T.F. Heinz, D.A. Reis und S. Ghimire, *Nature Photonics* **16** (2022), 620.

[62] T. Heinrich, M. Taucer, O. Kfir, P.B. Corkum, A. Staudte, C. Ropers und M. Sivis, *Nature Communications* **12** (2021).

[63] B. Henke, E. Gullikson und J. Davis, *Atomic Data and Nuclear Data Tables* **54** (1993), 181 .

[64] B.L. Henke, J.A. Smith und D.T. Attwood, *Journal of Applied Physics* **48** (1977), 1852.

[65] M. Hentschel, R. Kienberger, C. Spielmann, G.A. Reider, N. Milosevic, T. Brabec, P. Corkum, U. Heinzmann, M. Drescher und F. Krausz, *Nature* **414** (2001), 509.

[66] C.M. Heyl, C.L. Arnold, A. Couairon und A. L'Huillier, *Journal of Physics B: Atomic, Molecular and Optical Physics* **50** (2016), 013001.

[67] M. Högner, V. Tosa und I. Pupeza, *New Journal of Physics* **19** (2017), 033040.

[68] P. Horowitz und W. Hill: *The Art of Electronics.* Cambridge University Press, USA, 1989.

[69] H. Ibrahim, B. Wales, S. Beaulieu, B.E. Schmidt, N. Thiré, E.P. Fowe, É. Bisson, C.T. Hebeisen, V. Wanie, M. Giguére, J.C. Kieffer, M. Spanner, A.D. Bandrauk, J. Sanderson, M.S. Schuurman und F. Légaré, *Nature Communications* **5** (2014), 4422.

[70] R. Iikubo, T. Fujiwara, T. Sekikawa, Y. Harabuchi, S. Satoh, T. Taketsugu und Y. Kayanuma, *The Journal of Physical Chemistry Letters* **6** (2015), 2463.

[71] N. Ishii, K. Kaneshima, K. Kitano, T. Kanai, S. Watanabe und J. Itatani, *Optics Letters* **37** (2012), 4182.

[72] N. Ishii, K. Kaneshima, K. Kitano, T. Kanai, S. Watanabe und J. Itatani, *Nature Communications* **5** (2014), 3331.

[73] N. Ishii, A. Kosuge, T. Hayashi, T. Kanai, J. Itatani, S. Adachi und S. Watanabe, *Optics Express* **16** (2008), 20876.

[74] J. Itatani, J. Levesque, D. Zeidler, H. Niikura, H. Pépin, J.C. Kieffer, P.B. Corkum und D.M. Villeneuve, *Nature* **432** (2004), 867.

[75] J. Itatani, F. Quéré, G.L. Yudin, M.Y. Ivanov, F. Krausz und P.B. Corkum, *Physical Review Letters* **88** (2002), 173903.

[76] Á. Jiménez-Galán, R.E.F. Silva, O. Smirnova und M. Ivanov, *Nature Photonics* **14** (2020), 728.

[77] C. Jin, G. Wang, H. Wei, A.T. Le und C.D. Lin, *Nature Communications* **5** (2014), 4003.

[78] T.M. Kardaś, M. Nejbauer, P. Wnuk, B. Resan, C. Radzewicz und P. Wasylczyk, *Scientific Reports* **7** (2017), 42889.

[79] S. Kazamias und P. Balcou, *Physical Review A* **69** (2004), 063416.

[80] L.V. Keldysh, *Journal of Experimental and Theoretical Physics* **20** (1965), 1307.

[81] P.R. Kidambi, R. Blume, J. Kling, J.B. Wagner, C. Baehtz, R.S. Weatherup, R. Schloegl, B.C. Bayer und S. Hofmann, *Chemistry of Materials* **26** (2014), 6380.

[82] K.K. Kim, A. Hsu, X. Jia, S.M. Kim, Y. Shi, M. Hofmann, D. Nezich, J.F. Rodriguez-Nieva, M. Dresselhaus, T. Palacios und J. Kong, *Nano Letters* **12** (2011), 161.

[83] K.T. Kim, C.M. Kim, M.G. Baik, G. Umesh und C.H. Nam, *Physical Review A* **69** (2004), 051805.

[84] C. Kittel: *Introduction to Solid State Physics.* Wiley, 2004.

[85] K. Kondo, Y. Kobayashi, A. Sagisaka, Y. Nabekawa und S. Watanabe, *Journal of the Optical Society of America B* **13** (1996), 424.

[86] K. Kovács und V. Tosa, *Optics Express* **27** (2019), 21872.

[87] F. Krausz und M. Ivanov, *Reviews of Modern Physics* **81** (2009), 163.

[88] F. Langer, C.P. Schmid, S. Schlauderer, M. Gmitra, J. Fabian, P. Nagler, C. Schüller, T. Korn, P.G. Hawkins, J.T. Steiner, U. Huttner, S.W. Koch, M. Kira und R. Huber, *Nature* **557** (2018), 76.

[89] A.T. Le, H. Wei, C. Jin und C.D. Lin, *Journal of Physics B: Atomic, Molecular and Optical Physics* **49** (2016), 053001.

[90] M. Lewenstein, P. Balcou, M.Y. Ivanov, A. L'Huillier und P.B. Corkum, *Physical Review A* **49** (1994), 2117.

[91] A. L'Huillier, X.F. Li und L.A. Lompré, *Journal of the Optical Society of America B* **7** (1990), 527.

[92] J. Li, J. Lu, A. Chew, S. Han, J. Li, Y. Wu, H. Wang, S. Ghimire und Z. Chang, *Nature Communications* **11** (2020), 2748.

[93] J. Li, X. Ren, Y. Yin, Y. Cheng, E. Cunningham, Y. Wu und Z. Chang, *Applied Physics Letters* **108** (2016), 231102.

[94] J. Li, X. Ren, Y. Yin, K. Zhao, A. Chew, Y. Cheng, E. Cunningham, Y. Wang, S. Hu, Y. Wu, M. Chini und Z. Chang, *Nature Communications* **8** (2017), 186.

[95] M. Li, S. Zhou, R. Wang, Y. Yu, H. Wong, Z. Luo, H. Li, L. Gan und T. Zhai, *Nanoscale* **10** (2018), 17865.

[96] X.F. Li, A. L'Huillier, M. Ferray, L.A. Lompré und G. Mainfray, *Physical Review A* **39** (1989), 5751.

[97] Y. Li, Y. Rao, K.F. Mak, Y. You, S. Wang, C.R. Dean und T.F. Heinz, *Nano Letters* **13** (2013), 3329. PMID: 23718906.

[98] H. Liang, P. Krogen, Z. Wang, H. Park, T. Kroh, K. Zawilski, P. Schunemann, J. Moses, L.F. DiMauro, F.X. Kärtner und K.H. Hong, *Nature Communications* **8** (2017), 141.

[99] H. Liu, C.Y. You, J. Li, P.R. Galligan, J. You, Z. Liu, Y. Cai und Z. Luo, *Nano Materials Science* **3** (2021), 291.

[100] J.M. Lu, O. Zheliuk, I. Leermakers, N.F.Q. Yuan, U. Zeitler, K.T. Law und J.T. Ye, *Science* **350** (2015), 1353.

[101] T.T. Luu, Z. Yin, A. Jain, T. Gaumnitz, Y. Pertot, J. Ma und H.J. Wörner, *Nature Communications* **9** (2018).

[102] F. Lücking, A. Assion, A. Apolonski, F. Krausz und G. Steinmeyer, *Optics Letters* **37** (2012), 2076.

[103] Q. Ma, S.Y. Xu, H. Shen, D. MacNeill, V. Fatemi, T.R. Chang, A.M.M. Valdivia, S. Wu, Z. Du, C.H. Hsu, S. Fang, Q.D. Gibson, K. Watanabe, T. Taniguchi, R.J. Cava, E. Kaxiras, H.Z. Lu, H. Lin, L. Fu, N. Gedik und P. Jarillo-Herrero, *Nature* **565** (2018), 337.

[104] T.H. Maiman, *Nature* **187** (1960), 493.

[105] Y. Mairesse und F. Quéré, *Physical Review A* **71** (2005), 011401.

[106] K.F. Mak, K. He, J. Shan und T.F. Heinz, *Nature Nanotechnology* **7** (2012), 494.

[107] K.F. Mak, C. Lee, J. Hone, J. Shan und T.F. Heinz, *Physical Review Letters* **105** (2010).

[108] K.F. Mak, K.L. McGill, J. Park und P.L. McEuen, *Science* **344** (2014), 1489.

[109] K.F. Mak, D. Xiao und J. Shan, *Nature Photonics* **12** (2018), 451.

[110] C.A. Mancuso, D.D. Hickstein, P. Grychtol, R. Knut, O. Kfir, X.M. Tong, F. Dollar, D. Zusin, M. Gopalakrishnan, C. Gentry, E. Turgut, J.L. Ellis, M.C. Chen, A. Fleischer, O. Cohen, H.C. Kapteyn und M.M. Murnane, *Physical Review A* **91** (2015).

[111] E. Mansten, J.M. Dahlström, P. Johnsson, M. Swoboda, A. L'Huillier und J. Mauritsson, *New Journal of Physics* **10** (2008), 083041.

[112] J. Mauritsson, P. Johnsson, E. Gustafsson, A. L'Huillier, K.J. Schafer und M.B. Gaarde, *Physical Review Letters* **97** (2006), 013001.

[113] A. McPherson, G. Gibson, H. Jara, U. Johann, T.S. Luk, I.A. McIntyre, K. Boyer und C.K. Rhodes, *Journal of the Optical Society of America B* **4** (1987), 595.

[114] S. Mitra, S. Biswas, J. Schötz, E. Pisanty, B. Förg, G.A. Kavuri, C. Burger, W. Okell, M. Högner, I. Pupeza, V. Pervak, M. Lewenstein, P. Wnuk und M.F. Kling, *Journal of Physics B: Atomic, Molecular and Optical Physics* **53** (2020), 134004.

[115] F. Mooshammer: *Twist-induced tuning of interlayer coupling in MoS2/WSe2 heterostructures.* University of Regensburg, Master's thesis, 2015.

[116] C. Figueira de Morisson Faria, D.B. Milošević und G.G. Paulus, *Physical Review A* **61** (2000), 063415.

[117] P.F. Moulton, *Journal of the Optical Society of America B* **3** (1986), 125.

[118] N. Nagaosa, J. Sinova, S. Onoda, A.H. MacDonald und N.P. Ong, *Reviews of Modern Physics* **82** (2010), 1539.

[119] M. Neuhaus, H. Fuest, M. Seeger, J. Schötz, M. Trubetskov, P. Russbueldt, H. Hoffmann, E. Riedle, Z. Major, V. Pervak, M.F. Kling und P. Wnuk, *Optics Express* **26** (2018), 16074.

[120] O. Novák, P.R. Krogen, T. Kroh, T. Mocek, F.X. Kärtner und K.H. Hong, *Optics Letters* **43** (2018), 1335.

[121] K.S. Novoselov, A.K. Geim, S.V. Morozov, D. Jiang, M.I. Katsnelson, I.V. Grigorieva, S.V. Dubonos und A.A. Firsov, *Nature* **438** (2005), 197.

[122] K.S. Novoselov, A.K. Geim, S.V. Morozov, D. Jiang, Y. Zhang, S.V. Dubonos, I.V. Grigorieva und A.A. Firsov, *Science* **306** (2004), 666.

[123] M. Okada, A. Kutana, Y. Kureishi, Y. Kobayashi, Y. Saito, T. Saito, K. Watanabe, T. Taniguchi, S. Gupta, Y. Miyata, B.I. Yakobson, H. Shinohara und R. Kitaura, *ACS Nano* **12** (2018), 2498.

[124] M. Okada, T. Sawazaki, K. Watanabe, T. Taniguch, H. Hibino, H. Shinohara und R. Kitaura, *ACS Nano* **8** (2014), 8273.

[125] A. Ozawa, J. Rauschenberger, C. Gohle, M. Herrmann, D.R. Walker, V. Pervak, A. Fernandez, R. Graf, A. Apolonski, R. Holzwarth, F. Krausz, T.W. Hänsch und T. Udem, *Physical Review Letters* **100** (2008), 253901.

[126] S. Pabst und J.M. Dahlström, *Journal of Physics B: Atomic, Molecular and Optical Physics* **50** (2017), 104002.

[127] Y. Pertot, C. Schmidt, M. Matthews, A. Chauvet, M. Huppert, V. Svoboda, A. von Conta, A. Tehlar, D. Baykusheva, J.P. Wolf und H.J. Wörner, *Science* **355** (2017), 264.

[128] D. Popmintchev, B.R. Galloway, M.C. Chen, F. Dollar, C.A. Mancuso, A. Hankla, L. Miaja-Avila, G. O'Neil, J.M. Shaw, G. Fan, S. Ališauskas, G. Andriukaitis, T. Balčiunas, O.D. Mücke, A. Pugzlys, A. Baltuška, H.C. Kapteyn, T. Popmintchev und M.M. Murnane, *Physical Review Letters* **120** (2018), 093002.

[129] T. Popmintchev, M.C. Chen, P. Arpin, M.M. Murnane und H.C. Kapteyn, *Nature Photonics* **4** (2010), 822.

[130] T. Popmintchev, M.C. Chen, D. Popmintchev, P. Arpin, S. Brown, S. Ališauskas, G. Andriukaitis, T. Balčiunas, O.D. Mücke, A. Pugzlys, A. Baltuška, B. Shim, S.E. Schrauth, A. Gaeta, C. Hernández-García, L. Plaja, A. Becker, A. Jaron-Becker, M.M. Murnane und H.C. Kapteyn, *Science* **336** (2012), 1287.

[131] C.V. RAMAN und K.S. KRISHNAN, *Nature* **121** (1928), 501.

[132] O. Raz, O. Pedatzur, B.D. Bruner und N. Dudovich, *Nature Photonics* **6** (2012), 170.

[133] H.G. Rosa, Y.W. Ho, I. Verzhbitskiy, M.J.F.L. Rodrigues, T. Taniguchi, K. Watanabe, G. Eda, V.M. Pereira und J.C.V. Gomes, *Scientific Reports* **8** (2018).

[134] S. Roscam Abbing, F. Campi, F.S. Sajjadian, N. Lin, P. Smorenburg und P.M. Kraus, *Physical Review Applied* **13** (2020), 054029.

[135] B. Saleh und M. Teich: *Fundamentals of Photonics*. Wiley Series in Pure and Applied Optics. Wiley, 2007.

[136] P. Salières, A. L'Huillier und M. Lewenstein, *Physical Review Letters* **74** (1995), 3776.

[137] J.R. Schaibley, H. Yu, G. Clark, P. Rivera, J.S. Ross, K.L. Seyler, W. Yao und X. Xu, *Nature Reviews Materials* **1** (2016).

[138] J. Schötz, B. Förg, W. Schweinberger, I. Liontos, H.A. Masood, A.M. Kamal, C. Jakubeit, N.G. Kling, T. Paasch-Colberg, S. Biswas, M. Högner, I. Pupeza, M. Alharbi, A.M. Azzeer und M.F. Kling, *Physical Review X* **10** (2020), 041011.

[139] J. Schötz, S. Mitra, H. Fuest, M. Neuhaus, W.A. Okell, M. Förster, T. Paschen, M.F. Ciappina, H. Yanagisawa, P. Wnuk, P. Hommelhoff und M.F. Kling, *Physical Review A* **97** (2018).

[140] J. Seres, E. Seres, A.J. Verhoef, G. Tempea, C. Streli, P. Wobrauschek, V. Yakovlev, A. Scrinzi, C. Spielmann und F. Krausz, *Nature* **433** (2005), 596.

[141] K.L. Seyler, J.R. Schaibley, P. Gong, P. Rivera, A.M. Jones, S. Wu, J. Yan, D.G. Mandrus, W. Yao und X. Xu, *Nature Nanotechnology* **10** (2015), 407.

[142] Y. Shi, C. Hamsen, X. Jia, K.K. Kim, A. Reina, M. Hofmann, A.L. Hsu, K. Zhang, H. Li, Z.Y. Juang, M.S. Dresselhaus, L.J. Li und J. Kong, *Nano Letters* **10** (2010), 4134.

[143] Y. Shi, J. Kahn, B. Niu, Z. Fei, B. Sun, X. Cai, B.A. Francisco, D. Wu, Z.X. Shen, X. Xu, D.H. Cobden und Y.T. Cui, *Science Advances* **5** (2019), eaat8799.

[144] R.E.F. Silva, M. Ivanov und Álvaro Jiménez-Galán, *Optics Express* **30** (2022), 30347.

[145] R.E.F. Silva, F. Martín und M. Ivanov, *Physical Review B* **100** (2019), 195201.

[146] A. Splendiani, L. Sun, Y. Zhang, T. Li, J. Kim, C.Y. Chim, G. Galli und F. Wang, *Nano Letters* **10** (2010), 1271.

[147] P. Steinleitner, N. Nagl, M. Kowalczyk, J. Zhang, V. Pervak, C. Hofer, A. Hudzikowski, J. Sotor, A. Weigel, F. Krausz und K.F. Mak, *Nature Photonics* **16** (2022), 512.

[148] D. Strickland und G. Mourou, *Optics Communications* **56** (1985), 219.

[149] S.M. Teichmann, F. Silva, S.L. Cousin, M. Hemmer und J. Biegert, *Nature Communications* **7** (2016), 11493.

[150] X.M. Tong und C.D. Lin, *Journal of Physics B: Atomic, Molecular and Optical Physics* **38** (2005), 2593.

[151] R. Trebino: *Frequency-Resolved Optical Gating: The Measurement of Ultrashort Laser Pulses: The Measurement of Ultrashort Laser Pulses*. Springer US, 2000.

[152] R. Trebino, K.W. DeLong, D.N. Fittinghoff, J.N. Sweetser, M.A. Krumbügel, B.A. Richman und D.J. Kane, *Review of Scientific Instruments* **68** (1997), 3277.

[153] G. Vampa, C.R. McDonald, G. Orlando, D.D. Klug, P.B. Corkum und T. Brabec, *Physical Review Letters* **113** (2014), 073901.

[154] M. Velický und P.S. Toth, *Applied Materials Today* **8** (2017), 68. 2D Materials in Electrochemistry.

[155] S.A. Vitale, D. Nezich, J.O. Varghese, P. Kim, N. Gedik, P. Jarillo-Herrero, D. Xiao und M. Rothschild, *Small* **14** (2018), 1801483.

[156] X. Wang, C. Jin und C.D. Lin, *Physical Review A - Atomic, Molecular, and Optical Physics* **90** (2014).

[157] P. Wei, J. Miao, Z. Zeng, C. Li, X. Ge, R. Li und Z. Xu, *Physical Review Letters* **110** (2013), 233903.

[158] P. Wernet, M. Odelius, K. Godehusen, J. Gaudin, O. Schwarzkopf und W. Eberhardt, *Physical Review Letters* **103** (2009), 013001.

[159] J. Wu, D. Luo, P. Wen, X. Han, C. Wang, H. Yu, W. Gao, X. Liu, G. Konstantatos, J. Li und N. Huo, *Advanced Optical Materials* **10** (2022), 2201902.

[160] S. Wu, V. Fatemi, Q.D. Gibson, K. Watanabe, T. Taniguchi, R.J. Cava und P. Jarillo-Herrero, *Science* **359** (2018), 76.

[161] W. Wu, L. Wang, Y. Li, F. Zhang, L. Lin, S. Niu, D. Chenet, X. Zhang, Y. Hao, T.F. Heinz, J. Hone und Z.L. Wang, *Nature* **514** (2014), 470.

[162] D. Xiao, G.B. Liu, W. Feng, X. Xu und W. Yao, *Physical Review Letters* **108** (2012).

[163] D. Xiao, W. Yao und Q. Niu, *Physical Review Letters* **99** (2007), 236809.

[164] V.S. Yakovlev, M. Ivanov und F. Krausz, *Optics Express* **15** (2007), 15351.

[165] L. Yao, D. Wu und G. Ma, *Applied Optics* **61** (2022), 6967.

[166] W. Yao, D. Xiao und Q. Niu, *Physical Review B* **77** (2008), 235406.

[167] Z. Ye, D. Sun und T.F. Heinz, *Nature Physics* **13** (2016), 26.

[168] J.W. Yoon, Y.G. Kim, I.W. Choi, J.H. Sung, H.W. Lee, S.K. Lee und C.H. Nam, *Optica* **8** (2021), 630.

[169] A.H. Zewail, *The Journal of Physical Chemistry A* **104** (2000), 5660.

[170] Y. Zhang, Y.W. Tan, H.L. Stormer und P. Kim, *Nature* **438** (2005), 201.

[171] Z.X. Zhao und T. Brabec, *Journal of Physics B: Atomic, Molecular and Optical Physics* **39** (2006), L345.

[172] S. Zherebtsov, T. Fennel, J. Plenge, E. Antonsson, I. Znakovskaya, A. Wirth, O. Herrwerth, F. Süßmann, C. Peltz, I. Ahmad, S.A. Trushin, V. Pervak, S. Karsch, M.J.J. Vrakking, B. Langer, C. Graf, M.I. Stockman, F. Krausz, E. Rühl und M.F. Kling, *Nature Physics* **7** (2011), 656.

[173] H. Zhu, J. Yi, M.Y. Li, J. Xiao, L. Zhang, C.W. Yang, R.A. Kaindl, L.J. Li, Y. Wang und X. Zhang, *Science* **359** (2018), 579.

[174] J.E. Zimmermann, B. Li, J.C. Hone, U. Höfer und G. Mette, *Journal of Physics: Condensed Matter* **32** (2020), 485901.

Acknowledgements

I am extremely grateful for the opportunity to undertake this doctoral research and to the many people who have supported me throughout this unique journey. Without their support, arriving at this paragraph would not have been possible.

To begin with, I would like to express my sincere appreciation to my supervisor, Prof. Matthias Kling, for his continued support and faith in me. I am grateful for his decision to extend my stay in his group beyond my master's thesis to pursue a doctoral degree. Not only did he contribute immensely to my development as a scientist, but also as an alpine skier, preparing me well for the ups and downs of academic research. I am also thankful to Prof. Ferenc Krausz for accommodating me and the Kling group under the umbrella of the Laboratory of Attosecond Physics (LAP), whose resources significantly benefited me. Additionally, I thank the International Max Planck Research School for Advanced Photon Science of the Max Planck Society, along with the coordinators Prof. Matthias Kling, Nicholas Karpowicz, apl. Prof. Vladislav Yakovlev, and Hanieh Fattahi, for accepting me into this structured school. The school largely contributed to the development of key soft skills, along with the necessary scientific skills.

On a day-to-day basis, I am very thankful to all the present and many ex-members of the Kling group and LAP for their truly collaborative team spirit, which has taught me innumerable ways of tackling challenges in my research. Namely, Johannes Schötz and Pawel Wnuk were instrumental in teaching me the tricks of the trade, especially during the initial formative months of my Ph.D. I also thank Hirofumi Yanagisawa for fruitful discussions on numerical simulations of nanotips (carried forward from my master's thesis). Furthermore, I thank Benjamin Förg, Christian Burger, and William Okell for extending their support with the laser and experimental infrastructure of my first project in this dissertation on HHG in tailored fields. Moreover, I am indebted to Maximilian Högner for providing me with his code (HHGMax), which led to a better understanding of the experimental results and also allowed me to pursue an additional numerical study presented in this thesis. Additionally, I thank the Max Planck Computing and Data Facility (MPCDF) for allowing me to use their computing resources, without which the numerical results from the above-mentioned code could not have been produced. Vladimir Pervak has always catered to our needs with customized dielectric mirror coatings, which were crucial for my experimental projects, and I am very thankful for this. I also thank our external collaborator, Emilio Pisanty, for his input and discussions during the final stages of the HHG project.

Shubhadeep Biswas played an instrumental role in supporting me during the final measurements of the HHG project and engaging in fruitful discussions on the results. Eventually, I ended up working closely with him on numerous other projects which he envisioned, including my final and largest project on 2D materials. Throughout this period, he posed new questions and challenges that never allowed me to feel bored and helped maintain a steady learning curve. I am also thankful to Marcel Neuhaus for supporting and maintaining the laser source, Álvaro Jiménez-Galán and Rui Silva for their critical contributions to the success of the 2D materials project through discussions and theoretical support, and Prof. Misha Ivanov for his positive outlook on the project, motivating us to pursue this project in the lab despite technical challenges. Jun Ong supported the development of a laser pulse characterization apparatus, and Lucca Kühner and Prof. Stefan Maier helped with Raman characterization of our 2D hBN samples, for which I am very thankful.

Behind all active research in the labs are many contributors to the projects mentioned above in the background. This leads me to acknowledge Mrs. Monika Wild, our ex-secretary at LAP, who provided me with a roof over my head in Munich for the first few months. Along with her, I thank Kerstin Schmidt-Buchmann, Nicole Buchwiser, and Klaus Franke for their ever-present support with administrative issues at MPQ and LMU. I also thank the purchasing department at MPQ for catering to various requests from us researchers. Finally, I am grateful for the support extended to me by the technical teams at MPQ and LMU, which include Lukas Schuster, Harald Haas, Rolf Öhm, Tobias Kleinhenz, Alois Böswald, and Andreas Küchler.

In addition to directly supporting the projects, networking within the Kling group and LAP has indirectly played a big role in maintaining an optimal work atmosphere. Many of them have been exceptionally understanding and supportive in various ways both within and outside work. Most of the Kling and other LAP group members I have had an overlap with, who are Johannes Stierle, Philipp Rupp, Christian Burger, Benjamin Förg, Johannes Schötz, Marcel Neuhaus, Harald Fuest, Pawel Wnuk, Shubhadeep Biswas, Dziugas Kimbaras, Ritika Dagar, Philipp Rosenberger, Weiwei Li, Gaia Barberio, Martin Graßl, and Kiran Maiti, were often around during lunch and coffee breaks to make life a little more interesting at work. During the initial years, I also thank Harshit Lakhotia for being a very friendly neighbor at work and home and for including me in most of his social adventures. Later, Keyhan Golyari was always there to chat over tea or coffee, and later share our mutual misfortunes with the Deutsche Bahn (S1) on the way and back from work. Mikhail Mamaikin, Enrico Ridente, Muhammad Qasim, and Najd Altwaijry were often around for entertaining breaks with Table Tennis and Mario Kart. I had the pleasure of sharing my offices at varying lengths with Wilhelm Frisch, Johannes Schötz, Thomas Weatherby, Ancyline Maliakkal, Dziugas Kimbaras, Amelie Schulte, and Manoram Agarwal who maintained a very positive and social atmosphere.

I am also thankful to the many collaborators with whom I worked on secondary research projects during my dissertation period. They allowed me to contribute and further grow my experience in different fields. Namely, Boris Bergues, Philipp Rupp, Philipp Rosenberger, Thomas Weatherby, Ritika Dagar, Ali Alnaser, Rami Ali, Said Alghabra, and Sharjeel Khan on the nanoTRIMS project at MPQ/LMU in Garching, Germany, and AUS in Sharjah, UAE. I also thank Prof. Dong Eon Kim for hosting me at POSTECH, South Korea for a project on laser pulse compression, along with Jongkyoon Park, Meenkyo Seo, and Tsendsuren Khurelbaatar, who were supportive lab mates during my short stay in an unfamiliar country. Similarly, I acknowledge the unhindered support (both in and outside the lab) from Ahmad Saleh, Wolfgang Schweinberger, Meshaal Alharbi, and Abdallah M. Azzeer at KSU, Saudi Arabia during my experimental project on attosecond streaking. Finally, a big thanks to Matthew Weidman and our former master's student, Martin Graßl, for partially accommodating me in his group and supporting me with rebuilding an attosecond beamline for an additional experimental campaign at MPQ, Garching on attosecond streaking.

The pursuit of a doctoral thesis often puts personal relationships in the back seat, especially when many of them live thousands of kilometers away. Despite this, I am very grateful for the unconditional love and support extended to me by my grandmother, father, mother, sister, and later my in-laws, who helped me regain a great deal of motivation lost after short-term failures in the lab, especially by reminding me how passionate I was when I started this journey. Similarly, I would like to express my appreciation towards my old and new friends outside work, in Germany, and elsewhere. I especially thank a few close childhood friends (collectively referred to as Bingo), who managed to stay in touch despite our mutually busy schedules in the last couple of years, looking out for me in their own ways. Last but not least, a very special recognition to my partner in crime, Priyanka Hegde, who stood by me through the thick and thin of this thesis, with her unwavering support and an extremely positive outlook toward life that eventually rubbed off on me.